
The Solar Tachocline:
A Self-Consistent Model
of Magnetic Confinement

Toby Wood
Queens' College, Cambridge



A DISSERTATION SUBMITTED TO
THE UNIVERSITY OF CAMBRIDGE FOR
THE DEGREE OF DOCTOR OF PHILOSOPHY
APRIL 2010

“There is no easy way from the earth to the stars”

Lucius Annaeus Seneca

Acknowledgements

First and foremost, I would like to thank my supervisor, Prof. M. E. McIntyre, for his continuing guidance and infectious enthusiasm for science. I have also benefited enormously from discussions with members of my research group, including Prof. D. O. Gough, Dr. G. I. Ogilvie, Prof. J. C. B. Papaloizou, Prof. M. R. E. Proctor and Prof. N. O. Weiss. I am indebted to Prof. J. Christensen-Dalsgaard for providing the one-dimensional profiles of the solar structure used in chapter [5](#).

I never would have got this far without the support of my family, friends and colleagues, whose advice at every stage has been invaluable. I am particularly indebted to Mark Rosin, for suggesting the possibility of a life beyond mathematics, and to Céline Guervilly, for proving him right.

Declaration

This dissertation is based on research done at the Department of Applied Mathematics and Theoretical Physics from October 2006 to February 2010. The material presented is original except where reference is made to the work of others in the text. Much of Parts [III](#) and [IV](#) are based upon research work performed in collaboration with my supervisor Professor Michael E. McIntyre, and published as [Wood & McIntyre \(2007\)](#) and [Wood & McIntyre \(2010\)](#).

TOBY WOOD
Cambridge,
November 15, 2010

Abstract

In this dissertation we consider the dynamics of the solar interior, with particular focus on angular momentum balance and magnetic field confinement within the tachocline.

In Part [I](#) we review current knowledge of the Sun’s rotation. We summarise the main mechanisms by which angular momentum is transported within the Sun, and discuss the difficulties in reconciling the observed uniform rotation of the radiative interior with purely hydrodynamical theories. Following [Gough & McIntyre \(1998\)](#) we conclude that a global-scale interior magnetic field provides the most plausible explanation for the observed uniform rotation, provided that it is confined within the tachocline.

We discuss potential mechanisms for magnetic field confinement, assuming that the field has a roughly axial-dipolar structure. In particular, we argue that the field is confined, in high latitudes, by a laminar downwelling flow driven by turbulence in the tachocline and convection zone above.

In Part [II](#) we describe how the magnetic confinement picture is affected by the presence of compositional stratification in the “helium settling layer” below the convection zone. We use scaling arguments to estimate the rate at which the settling layer forms, and verify our predictions with a simple numerical model. We discuss the implications for lithium depletion in the convection zone.

In Part [III](#) we present numerical results showing how the Sun’s interior magnetic field can be confined, in the polar regions, while maintaining uniform rotation within the radiative envelope. These results come from solving the full, nonlinear equations numerically. We also show how these results can be understood in terms of a reduced, analytical model that is asymptotically valid in the parameter regime of relevance to the solar tachocline.

In Part [IV](#) we discuss how our high-latitude model can be extended to a global model of magnetic confinement within the tachocline.

Contents

I	Solar Dynamics	1
1	Basic Solar Physics	3
1.1	Solar structure and observations	3
1.2	Rotating, stratified fluids	5
1.3	Magnetised fluids	8
1.4	Solar spin-down	9
2	The Sun's Differential Rotation	15
2.1	Standard solar models	15
2.2	Helioseismology	16
2.3	Differential rotation	19
2.4	The tachocline	27
2.5	Dynamo theory	30
3	The Magnetic Interior	35
3.1	The Sun's fossil field	35
3.2	The Ferraro constraint	36
3.3	The magnetic confinement problem	38

4	Magnetic Field Confinement	43
4.1	Magnetic pumping	43
4.2	Mean meridional circulations (MMCs)	46
4.3	Summary	62
II	Solar Composition	63
5	Helium Settling	65
5.1	The μ -choke	65
5.2	The settling equation	68
5.3	The formation of the helium settling layer	71
5.4	The compositional gradient	75
5.5	Summary	76
6	Depletion of Lithium and Beryllium	79
III	The Magnetic Confinement Layer	83
7	The High-Latitude Tachocline	85
7.1	The structure of the magnetic field	85
7.2	The structure of the tachocline	86
7.3	Angular momentum balance	87
7.4	The equations and parameters	89
7.5	The limit of infinite stratification	92
7.6	Finite stratification	96

7.7 Summary	98
8 The Magnetic Confinement Layer	99
9 The Helium Sublayer	105
9.1 Sublayer scalings	105
9.2 The subtail	109
10 The Numerical Model	111
10.1 Numerical complexity	111
10.2 The numerical scheme	113
10.3 Boundary conditions	114
10.4 The numerical solutions	118
10.5 Upper-domain “slipperiness”	122
IV Conclusions	125
11 Discussion	127
12 Future Work	131
12.1 Gyroscopic pumping	131
12.2 Lithium burning	132
V Appendices	133
A Parameter Values	135

B	Meridional Circulation	137
C	MAC Waves	141
D	The Magnetic Margules Front	145
E	Magnetic Pumping	149
F	The Tayler Instability	153
G	The Tayler–Spruit Dynamo	157
H	The Numerical Scheme	161
H.1	Equations	161
H.2	Finite-differences	164
H.3	Magnetostrophic balance	166
I	Numerical Test Cases	169
I.1	Transient adjustment	169
I.2	Magnetostrophic balance	170
I.3	Numerical boundaries	171
I.4	Horizontal resolution	173
I.5	Horizontal diffusion	174

Part I

Solar Dynamics

Chapter 1

Basic Solar Physics

1.1 Solar structure and observations

1.1.1 Thermodynamics

The Sun formed from the gravitational collapse of a molecular cloud approximately 5 billion years ago. This collapse was halted once the radial (i.e. outward) pressure gradient became large enough to balance the gravitational attraction, leading to a state of hydrostatic balance that has persisted throughout the Sun’s main-sequence lifetime. Departures from hydrostatic balance are restored on the dynamical timescale (≈ 20 minutes).

Within the Sun’s core, which extends to around 30% of the Sun’s radius¹ R_{\odot} , high pressure and temperature cause hydrogen nuclei to fuse into helium, releasing the energy that powers the Sun (and all life on Earth). The thermal energy released in the core is carried outward by photon radiation. Throughout the solar interior, pressure, density and temperature all decrease outward with radius (see figure 1.1), but the radial entropy gradient changes sign at around $0.7R_{\odot}$. The Sun’s “super-adiabatic” outer layers are convectively unstable, and heat is transported outward through these layers by fluid motions as well as by photon radiation. The boundary between the convective and radiative zones is

¹Throughout this dissertation, we will use R for spherical radius and r for cylindrical radius. The value of R_{\odot} and other relevant parameters are listed in appendix A.

blurred slightly by the presence of dynamical instabilities and penetration by “overshooting” convective plumes, but these processes are limited by the strong stable stratification of the radiative envelope, as will be described in chapter 2.

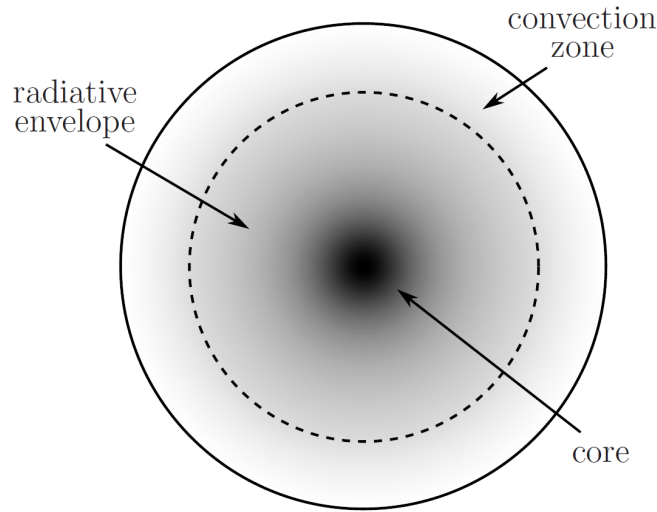


Figure 1.1: The interior structure of the Sun, shaded according to temperature. The dashed line indicates the boundary between the convection zone and the radiative envelope.

1.1.2 Rotation

The one-dimensional solar model just described ignores the effects of the Sun’s rotation. From an energetic perspective this is a valid approximation, because the total rotational energy of the Sun is only a tiny fraction of its thermal energy. But the Sun’s rotation significantly affects the dynamics of its interior, for reasons described in §1.2.

The Sun rotates at a rate of about once a month. The total angular momentum of the Sun is in fact only a small fraction of the angular momentum that was present in the molecular cloud from which the Sun formed. This cloud would have rotated relative to its centre at a rate given roughly by “Oort’s second constant”² — i.e. half the vorticity of the local galactic rotation. If angular momentum had been perfectly conserved during the gravitational collapse of this gas cloud, the “ballerina effect” would have caused the Sun to form with a rotation period of

²Approximately one rotation every 500 million years.

just a few seconds. In reality most of this angular momentum was lost during the early stages of the Sun’s formation, but nevertheless the Sun probably had a rotation period of less than one day when it arrived on the main sequence (e.g. [Mestel & Weiss, 1987](#), & refs). The Sun must therefore have continued to shed angular momentum even during its main-sequence lifetime. We return to the issue of “solar spin-down” in §1.4.

1.1.3 Magnetism

The Sun has a magnetic field, which can be observed where it extends out from the solar surface. The field at the surface has an average strength of around one gauss (slightly stronger than the Earth’s surface field), although field strengths of a few thousand gauss exist in localised patches called sunspots. The field is generated within the Sun’s convection zone, where the fluid motions act as a dynamo (§2.5), and decays in strength algebraically at large distances from the solar surface. The spin-down of the Sun is closely connected to the presence of this external magnetic field, as will be described in §1.4. First, however, we introduce some relevant fluid dynamics associated with rotating, stratified and magnetised fluids.

1.2 Rotating, stratified fluids

In a rotating system, small perturbations to the lines of absolute vorticity³ propagate as inertial waves (also known as epicyclic or Coriolis waves), with a wavespeed proportional to the rate of rotation. The dynamical importance of rotation is generally quantified by the Rossby number Ro , which is a measure of inertial forces, in the rotating frame, against Coriolis forces (e.g. [Greenspan, 1968](#)). If motions in the fluid have a characteristic timescale τ , say, and the overall rotation rate of the system is Ω , then the Rossby number is defined as $Ro = 1/(2\Omega\tau)$. For a rapidly rotating (i.e. low Rossby number) system, inertial wave propagation inhibits fluid motions that deform the lines of absolute vorticity — this is sometimes known as “rotational stiffness”. This physical principle

³Here, “absolute” vorticity refers to the total vorticity in an inertial frame.

is crystallised within the Taylor–Proudman theorem: for a barotropic fluid in a balance of Coriolis, pressure and gravitational forces, any motions perpendicular to the rotation axis must be invariant in the direction parallel to the rotation axis. Flow of this kind is called “geostrophic”. In a geostrophic fluid, any differential rotation must be “constant on cylinders”.

In a stratified, *non*-barotropic fluid, surfaces of constant density can be tilted with respect to surfaces of constant pressure. This “baroclinicity” is a source of vorticity in the direction perpendicular to the gradients of pressure and density. The presence of baroclinicity can overcome the Taylor–Proudman constraint. In particular, baroclinic production of azimuthal vorticity can balance the azimuthal vorticity produced by axial variations in the centripetal acceleration; this is known as “thermal-wind balance” (e.g. [Pedlosky, 1979](#)). Adopting cylindrical polar coordinates (r, ϕ, z) centred on the axis of rotation, this balance can be expressed as

$$\frac{\partial}{\partial z}(\Omega^2 r) = \frac{1}{\rho^2}(\nabla p \times \nabla \rho) \cdot \mathbf{e}_\phi, \quad (1.1)$$

where Ω is the local rotation rate, p and ρ are the pressure and density fields, and \mathbf{e}_ϕ is the unit-vector directed azimuthally. If the system is also in hydrostatic balance, and if we assume that fractional pressure perturbations are small compared with fractional density perturbations, then we may approximate $\nabla p \approx \rho \mathbf{g}$, where \mathbf{g} is the modified gravitational acceleration, i.e. the gradient of the total gravito-centrifugal potential. Equation (1.1) now becomes

$$\frac{\partial}{\partial z}(\Omega^2 r) \approx \frac{1}{\rho}(\mathbf{g} \times \nabla \rho) \cdot \mathbf{e}_\phi. \quad (1.2)$$

So any axial gradient in the angular velocity must be accompanied by a horizontal⁴ density gradient. In the absence of such gradients, the system reverts to a “Taylor–Proudman state”, with no axial variation in Ω . (A simple example of thermal-wind balance is the “Margules front” described in [appendix D](#).)

In an axisymmetric fluid, neither pressure nor gravity exert any torque about the axis of symmetry. So if we apply an axisymmetric torque to a fluid in a steady balance of Coriolis, pressure and gravitational forces, we expect the fluid to find

⁴Throughout this dissertation, we will use “horizontal” to refer to the directions perpendicular to \mathbf{g} .

a new steady state in which the applied torque is balanced by a Coriolis torque. Hence a retrograde applied torque, for example, will “gyroscopically pump” a flow toward the rotation axis. Viewed in an inertial (i.e. non-rotating) frame of reference, the fluid spirals in toward the rotation axis; the orbital decay of satellites is an analogous process. Since the fluid must conserve mass, the gyroscopically pumped flow must form part of a meridional circulation (see appendix B). The circulation transports angular momentum, and thus a retrograde torque applied at one location in the fluid can gyroscopically pump a circulation that spins down the entire fluid. Spin-down in a stirred cup of tea occurs in precisely this fashion; in that case the meridional circulation is driven primarily by the retrograde frictional torque at the bottom of the cup (e.g. Greenspan, 1968).

In the Earth’s stratosphere, breaking gravity and Rossby waves constitute, in a time-averaged sense, an effective retrograde forcing. This forcing drives the Brewer–Dobson and Murgatroyd–Singleton mean meridional circulations (MMCs) (e.g. Andrews *et al.*, 1987). However, in a stably stratified system such as the stratosphere, buoyancy forces act to restore any vertically displaced fluid elements to their original height. This produces oscillations known as internal gravity waves, whose frequency is proportional to the “buoyancy frequency” N (see appendix C). For large N , buoyancy inhibits motions that deform the stratification surfaces, producing a “horizontal stiffness”. The presence of stable stratification therefore tends to inhibit the formation of meridional circulations in rotating systems. In the absence of a “thermal relaxation” mechanism (i.e. a mechanism that diabatically returns the system to a reference-state temperature profile) there can be no compromise between stable thermal stratification and meridional circulations: either the circulation overturns the stratification surfaces or the stable stratification shuts off the circulation.

When a thermal relaxation mechanism is present, however, meridional circulations can co-exist with stable thermal stratification on lengthscales and timescales for which the rate of relaxation matches the rate of advection of the stratification. In that case, meridional flows driven persistently at a particular altitude tend to “burrow” downward over time, increasing the vertical extent of the circulation. This burrowing tendency gives rise to the principle of “downward control” (Haynes *et al.*, 1991), which states that the steady-state meridional mass flux at

any altitude is determined by the gyroscopic pumping at higher altitudes.

1.3 Magnetised fluids

Motions within an ionised fluid, or plasma, can induce a magnetic field. If the plasma is highly collisional and non-relativistic then the evolution of the magnetic field, \mathbf{B} say, is described by the MHD induction equation, which states that the magnetic field lines are advected by the fluid flow, and that the field diffuses at a rate inversely proportional to σ , the electrical conductivity of the plasma. Specifically,

$$\frac{\partial \mathbf{B}}{\partial t} = \nabla \times (\mathbf{u} \times \mathbf{B} - \eta \nabla \times \mathbf{B}) , \quad (1.3)$$

where $\eta = (4\pi\sigma)^{-1}$ is the magnetic diffusivity.⁵ The magnetic field influences the dynamics of the plasma through its Lorentz force, $\mathbf{F}_L = (4\pi)^{-1}(\nabla \times \mathbf{B}) \times \mathbf{B}$. Since the magnetic field is solenoidal, i.e. $\nabla \cdot \mathbf{B} = 0$, the Lorentz force can be written as the sum of gradient and curvature contributions,

$$\mathbf{F}_L = -\frac{1}{4\pi} \nabla \left(\frac{1}{2} |\mathbf{B}|^2 \right) + \frac{1}{4\pi} \mathbf{B} \cdot \nabla \mathbf{B} , \quad (1.4)$$

which are separately called the “magnetic pressure force” and “magnetic tension”. In the limit of perfect electrical conductivity (i.e. zero magnetic diffusivity) the field lines behave like elastic strings “frozen into” the fluid. Perturbations to the field lines generate Alfvén waves, which propagate along the field lines analogously to tension waves on an elastic string (Alfvén, 1942). The speed of propagation is the Alfvén speed, which is proportional to the strength of the magnetic field. If the Alfvén speed greatly exceeds the typical speeds of fluid motions within the plasma then the field lines behave rigidly. Therefore a strong magnetic field inhibits motions that perturb the field lines.

In the limit of strong magnetic field, only fluid motions that do not perturb the field lines are permitted. This “field-line stiffness” is somewhat analogous to the rotational stiffness described in §1.2. If the fluid is differentially rotating, then its angular velocity must be constant along each magnetic field line; this is known

⁵We use Gaussian-cgs units throughout this dissertation.

as Ferraro’s law of isorotation, after [Ferraro \(1937\)](#). In the presence of weak magnetic diffusion, the rigidity of the field lines becomes compromised, and fluid may “leak” across the field lines on long timescales and small lengthscales.

In a fluid that features rapid rotation, stable stratification and strong magnetic fields, motions of the fluid will be subject to all of the physical effects described in this and the previous section. Some simple systems that demonstrate the interplay between the various physical effects are described in appendices [C](#) and [D](#). A more complicated, but more immediately relevant, case study for many of these effects is solar spin-down — i.e. the gradual loss of angular momentum from the Sun over its main-sequence lifetime. This is described in detail in the next section.

1.4 Solar spin-down

1.4.1 Magnetic braking

Solar spin-down owes its origin to the “solar wind” — that is, the material ejected from the solar surface with sufficient energy to escape the Sun’s gravity — and the interaction of the wind with the Sun’s external magnetic field ([Schatzman, 1962](#)). Close to the solar surface the Alfvén speed exceeds the wind speed, and so the magnetic field lines behave rigidly. Therefore the wind is constrained to follow the field lines outward until it reaches the “Alfvén radius”, at which the wind speed overtakes the (outwardly decreasing) Alfvén speed. Moreover, within the Alfvén radius each magnetic field line rotates with the same angular velocity as its footpoint on the solar surface. So the matter ejected from the surface of the Sun in the solar wind conserves its angular velocity (rather than its angular *momentum*) until it reaches the Alfvén radius. This implies that the magnetic field exerts a prograde “Alfvénic” torque on the solar wind, and a corresponding retrograde Alfvénic torque on the solar surface.

“Magnetic braking” from the Sun’s external magnetic field acts only on the outermost layers of the Sun, since the tension in the field lines is overcome by the turbulent motions deeper within the convection zone. However, these turbulent

convective motions themselves transport angular momentum, and thus the spin-down of the solar surface is communicated throughout the convection zone on a timescale comparable to the turnover time of the largest convective eddies, which is about one month. We can crudely model this process by parametrising the convective turbulence as a large “turbulent viscosity” within the convection zone.

Within the stably stratified radiative envelope, the effective viscosity returns to its smaller, microscopic value. The timescale for purely viscous transport of angular momentum through this region is longer than the Sun’s lifetime. We might therefore expect solar spin-down to be confined to the convection zone, with the radiative envelope beneath rotating more rapidly. However, there are several mechanisms that can exchange angular momentum between the convection zone and radiative envelope, even when viscosity is negligible. These are discussed in the following sections.

1.4.2 Meridional circulations

If magnetic braking caused the solar convection zone to rotate more slowly than the radiative envelope, then the time-averaged turbulent stresses at the base of the convection zone would exert a drag on the top of the radiative envelope, gyroscopically pumping mean meridional circulations (MMCs) by the process described in §1.2. Spiegel (1972) described how, within a few rotation periods, these “spin-down currents” would establish a Taylor–Proudman regime within the outer part of the radiative envelope, wherein the rotation rate would match that of the convection zone, say Ω . The radiative envelope’s stable stratification would temporarily confine these MMCs to a layer of thickness $\sim (2\Omega/N)R$, where R is the radius of the convective–radiative interface, and N is the buoyancy frequency of the radiative envelope. Spiegel called this layer⁶ the “tachycline” (see figure 1.2). On a longer timescale, thermal relaxation would allow the MMCs to burrow deeper into the interior, as described in §1.2. Within the radiative envelope, thermal relaxation occurs through radiative diffusion, and so this burrowing process is often called “radiative spreading”. Using κ to denote the radiative

⁶A layer of this kind is often called a Holton layer, after Holton (1965), although the vertical lengthscale $(2\Omega/N)R$ is named the “Rossby height”, after Rossby (1938).

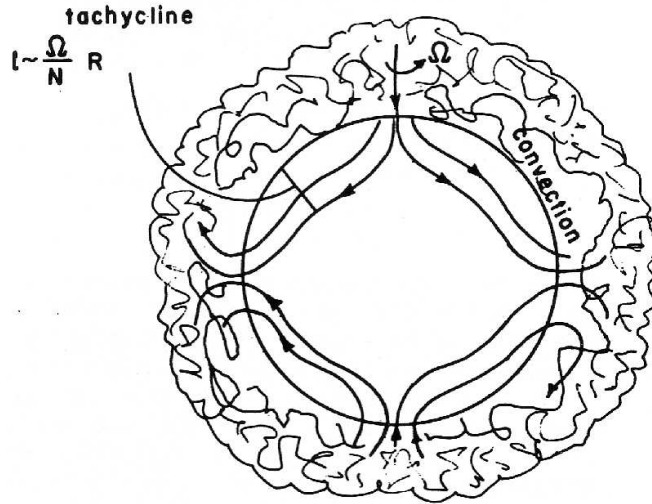


Figure 1.2: The convection zone’s slow rotation gyroscopically pumps spin-down currents within a “tachycline” in the outer part of the radiative envelope. Taken from [Spiegel \(1972\)](#).

diffusivity, the timescale⁷ τ for the burrowing, or spreading, is

$$\tau = \left(\frac{N}{2\Omega} \right)^2 \frac{R^2}{\kappa} . \quad (1.5)$$

If we take Ω to be the present rotation rate of the solar surface, then $\tau \approx 10^{11}$ years — much longer than the age of the Sun. But in the early, faster rotating Sun, the burrowing tendency would have been stronger, and this timescale would have been 10^9 years or less. If no other angular momentum transport mechanism were operating below the convection zone, then by now the surface spin-down would have been communicated perhaps half way to the centre of the Sun (see §2.4).

1.4.3 Internal gravity waves

As mentioned in §1.1.1, downward convective plumes close to the bottom of the convection zone may well overshoot and penetrate some way into the stably stratified radiative envelope. These overshooting plumes will excite internal gravity

⁷The physical mechanism that drives these circulations is closely analogous to that which drives the Eddington–Vogt–Sweet circulation (e.g. [Clark, 1975](#)). Indeed, the timescale in (1.5) is a (radially) local Eddington–Sweet timescale.

waves within the stably stratified interior. In fact, even in the absence of overshooting convection, fluctuating Reynolds stresses at the base of the convection zone can excite internal gravity waves in the radiative envelope.

Internal gravity waves carry an angular momentum flux. In the absence of global rotation, waves carrying westward and eastward angular momentum fluxes are excited and dissipated equally. But the presence of significant global rotation introduces asymmetry between these two types of waves, and therefore allows for wave-induced angular momentum transport (Schatzman, 1993; Zahn *et al.*, 1997). In order for this transport to be effective in the solar interior, the waves must be significantly dissipated within that region. Microscopic viscosity and radiative diffusion are too small to produce the required dissipation, so it must be supposed either that the interior is turbulent, with an effective turbulent diffusivity, or that the waves steepen and break at some depth within the interior. For certain parametrisations of the waves' generation and dissipation, the resulting angular momentum coupling between the convection zone and radiative envelope is found to be significant on the timescale of solar evolution (see Charbonnel & Talon, 2007, for a review of the successes of this theory). The effect of internal gravity waves on the rotation profile of the solar interior will be discussed further in chapter 2.

1.4.4 The Ferraro constraint

If the solar interior contains a global-scale magnetic field, \mathbf{B}_i say, then the picture of angular momentum transport changes dramatically (Mestel & Weiss, 1987; Charbonneau & MacGregor, 1993). In that case angular momentum is communicated along the field lines by Alfvén waves, and the pattern of angular momentum transport therefore depends on the topology of the field. Assuming that the field is confined within the radiative interior, and that $|\mathbf{B}_i| \gtrsim 10^{-2}$ gauss, Mestel & Weiss (1987) argued that the field would wipe out any radial differential rotation over the course of the Sun's main-sequence lifetime. The spin-down of the convection zone would thereby be efficiently communicated throughout the entire Sun.

Charbonneau & MacGregor (1993) constructed a simple axisymmetric, time-dependent computational model of spin-down in the solar interior in the presence of a global-scale magnetic field. They assumed that the stable stratification of the radiative interior would suppress any vertical motions within that region. Since their system was axisymmetric, only rotational motions were therefore permitted, and so Coriolis effects were absent. Furthermore, they neglected diffusion of the poloidal components of the magnetic field, so that the poloidal field configuration, which they took to be an axisymmetric dipole, could be statically imposed throughout the simulation. Therefore the only equations solved were the azimuthal components of the momentum and induction equations, and the only forces considered were Lorentz and viscous torques.

Charbonneau & MacGregor (1993) parametrised the turbulence in the convection zone as a large turbulent viscosity, and introduced a distributed “angular momentum sink” within the convection zone to represent magnetic braking by the solar wind. Over the course of their simulations, turbulent viscosity maintained near-uniform rotation within the convection zone, which was therefore spun down at the same rate as the solar surface. The manner in which spin-down was communicated to the interior was found to depend on the topology of the imposed poloidal magnetic field \mathbf{B}_i . The spin-down of the convection zone was rapidly communicated along any field lines that connected the radiative envelope to the convection zone, leading to a Ferraro state (recall §1.3). In cases for which the field was located entirely below the base of the convection zone, spin-down within the radiative interior was initially confined to a growing viscous boundary layer at the interface with the convection zone. Once this boundary layer grew sufficiently thick to encounter the deep magnetic field, a Ferraro state was again established within the interior. In all the cases they considered, a quasi-steady Ferraro rotation profile was established within approximately 10^7 years.

The effect of an interior magnetic field on angular momentum transport is discussed in further detail in chapter 3.

Chapter 2

The Sun’s Differential Rotation

2.1 Standard solar models

The internal structure of a star is, in most cases, uniquely determined by its mass and composition (e.g. [Kähler, 1978](#)). Hence the star’s future evolution is also uniquely determined; this is known as the “Vogt–Russell theorem”. In one-dimensional solar evolution models it is commonly assumed that the Sun was compositionally homogeneous at the start of its main-sequence phase (see §5). In principle, therefore, the internal structure of the Sun at any time on the main sequence can be determined from its initial mass, and the initial mass fractions of each of its chemical constituents. However, the effect of turbulence within the Sun’s convection zone cannot be precisely quantified by any analytical formula, and must instead be parametrised within one-dimensional solar evolution models. The most commonly used parametrisation is the “mixing-length” treatment of [Böhm-Vitense \(1958\)](#).

Furthermore, most solar evolution models assume that the Sun’s mass is constant. The necessary input parameters for these models are therefore the mixing-length parameter α , the helium mass fraction Y , and the “metallicity” Z , which is the mass fraction of all elements that are heavier than helium. The models are then calibrated by adjusting these input parameters to match the Sun’s present radius, luminosity and the ratio of Z/X at the solar surface, where X is the mass fraction of hydrogen. The surface ratio Z/X is not directly observable, but can

be inferred from spectroscopic data, via a suitable model of the solar atmosphere (e.g. [Christensen-Dalsgaard, 2002](#), & refs).

Until fairly recently, surface measurements of the abundance ratio Z/X were obtained using one-dimensional models of the solar atmosphere, and assumed local thermal equilibrium (LTE) (e.g. [Holweger & Müller, 1974](#)). In such models, the broadening and displacement of spectral lines by convective turbulence must be parametrised, usually in terms of “microturbulence” and “macroturbulence” (e.g. [de Jager, 1972](#)). More recent abundance measurements have been based on three-dimensional models of convection at the solar surface ([Stein & Nordlund, 1998](#)), and incorporate many non-LTE effects. The consequences of such effects for surface abundance measurements have been reviewed by [Asplund \(2005\)](#).

Arguably the main advantage of the new three-dimensional models over previous models is that they contain no adjustable “turbulence” parameters ([Asplund et al., 2006](#)), and therefore permit less ambiguity in the interpretation of the results. The development of these models has led to significant revision of the surface abundance measurements. The revised abundances of carbon, nitrogen and oxygen are lower than previous estimates (e.g. [Asplund et al., 2009](#)), and more closely reflect the abundances of the local interstellar medium ([Grevesse et al., 2007](#), & refs). The abundance ratio Z/X at the solar surface is now estimated to be 0.0181, which is significantly lower than previous estimates (e.g. [Grevesse & Sauval, 1998](#), estimated 0.023).

The revised abundances have serious implications for solar evolution models, to be discussed in the next section.

2.2 Helioseismology

In the 1970s, observations of the Sun’s surface oscillations demonstrated the existence of acoustic (p) modes, excited by turbulence in the convection zone ([Appourchaux et al., 2010](#), & refs). These observations, taken together with reasonable dynamical assumptions, allow certain properties of the solar interior to be inferred. In particular, if the oscillations are assumed to be linear, adiabatic perturbations to a spherically symmetric and hydrostatic background, then the

radial profiles of pressure, density and sound speed can be inferred from the oscillation spectrum (e.g. [Christensen-Dalsgaard & Thompson, 2007](#), & refs).¹ The sound speed is particularly well constrained (to within a few parts in 10^4) since it is the principal factor determining the acoustic oscillation frequencies. However, the vertical profiles of temperature and luminosity, for example, cannot be inferred without invoking additional, thermodynamical assumptions.

Helioseismology provides a means of testing models of the Sun’s interior structure. In particular, it can be used to locate the base of the convection zone, defined (in the context of helioseismology) to be the depth at which the mean stratification changes from almost adiabatic to subadiabatic. This transition is located at $(0.713 \pm 0.003)R_{\odot}$ ([Christensen-Dalsgaard *et al.*, 1991](#)). Ideally, solar evolution models should be able to reproduce this result with reasonable accuracy. Helioseismology can also be used to measure the helium mass fraction Y in the convection zone, provided that the equation of state is known ([Basu & Antia, 1995](#)), which provides an additional test of solar evolution models.

Until recently, standard solar models were in close agreement with the results of helioseismology (e.g. [Christensen-Dalsgaard *et al.*, 2009](#), & refs). However, solar models that are calibrated to match the revised abundances described in §2.1 agree less well with helioseismology, primarily because the opacity of solar material is sensitive to the abundance of heavy elements (e.g. [Basu & Antia, 2004](#)). Recalibrating standard solar models to match the revised abundances leads to an opacity decrease of around 25% near the base of the convection zone ([Montalbán *et al.*, 2006](#), & refs). As a result, the convection zone in these recalibrated models is significantly thinner, by about 10Mm ([Bahcall & Pinsonneault, 2004](#)). These recalibrated models also have a smaller helium mass fraction Y in the convection zone than is inferred from helioseismology, and a smaller sound speed in the radiative envelope.

Many authors have sought a possible resolution to the discrepancies between the recalibrated solar models and helioseismic results (see review in [Montalbán *et al.*, 2006](#)). Since the most significant effect of the revised abundances is a reduction

¹The inversion is achieved by iteratively refining a chosen reference model, and so the results may depend, to some extent, on the reference model chosen. See [Christensen-Dalsgaard & Thompson \(2007\)](#) for further details.

in opacity, the simplest resolution is simply to artificially increase the opacity by an appropriate amount, over the required temperature range (e.g. [Bahcall & Serenelli, 2005](#); [Christensen-Dalsgaard *et al.*, 2009](#)). However, there seems to be no physical justification for such a large opacity increase ([Badnell *et al.*, 2005](#)).

Since gravitational settling leads to a reduction in the surface abundance of heavy elements (see chapter 5), an alternative resolution is to increase the settling velocities used in solar models (e.g. [Montalbán *et al.*, 2004](#)). In this way, the present surface abundances can be explained without significantly changing the primordial abundances. However, this also reduces the abundance of helium in the convection zone, again in contradiction with the helioseismic results.

The opacity of solar material is highly sensitive to the abundance of neon, whose surface abundance cannot be measured directly by spectroscopy. Increasing the neon abundance of standard solar models by a factor of three would largely compensate for the reduction in other heavy-element abundances ([Bahcall *et al.*, 2005](#)). Whether such a high neon abundance is compatible with observations remains controversial ([Grevesse *et al.*, 2007](#), & refs).

As mentioned in §2.1, the “convection zone” defined by helioseismology includes any region in which entropy is well mixed, for example by convective overshoot. Including an overshoot layer in the recalibrated solar evolution models, with a thickness ≈ 10 Mm, therefore yields a convection zone whose thickness and helium abundance are in agreement with helioseismology. However, the sound speed profile within the radiative envelope in these models still departs significantly from the profile obtained seismologically ([Montalbán *et al.*, 2006](#)).

The present uncertainty regarding the Sun’s internal structure must be borne in mind when constructing any model of its internal dynamics. Fortunately, helioseismology is able to provide considerable information with relatively few assumptions. In the next section we review the properties of the Sun’s interior rotation that have been inferred from helioseismology.

2.3 Differential rotation

Carrington’s sunspot observations of the 1860s revealed that the surface of the Sun is differentially rotating, and that its angular velocity increases monotonically from pole to equator. Subsequent observations of sunspots and other magnetic tracers, as well as Doppler-shift measurements, allowed for more accurate measurement of the surface rotation, and it was found that the pole-to-equator variation is approximately 30% of the mean rotation rate.

With the advent of helioseismology, it became possible to infer the Sun’s interior rotation rate from the “rotational splitting” of the acoustic frequency spectrum (e.g. [Christensen-Dalsgaard & Thompson, 2007](#), & refs). It was found that the surface pattern of differential rotation persists qualitatively unchanged down to the base of the convection zone, but that the radiative envelope beneath is in approximately uniform rotation (see figure 2.1). The early helioseismic inferences

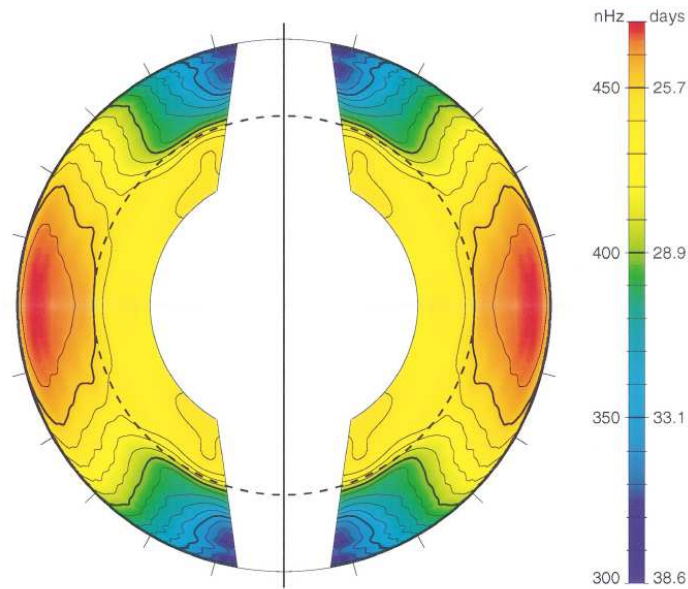


Figure 2.1: The angular velocity of the solar interior, adapted from [Schou *et al.* \(1998\)](#). The radiative envelope (below the dashed line) rotates approximately uniformly, with an angular velocity $\Omega_i \approx 2.7 \times 10^{-6} \text{s}^{-1}$. The convection zone (above the dashed line) exhibits significant differential rotation.

were subsequently refined, and the transition from differential to uniform rotation was found to occur across a thin shear-layer, which came to be known as the “tachocline” ([Spiegel & Zahn, 1992](#)). Even with modern helioseismology, the

tachocline is too thin to be accurately resolved, but its thickness is thought to be $\lesssim 30$ Mm — less than 5% of the Sun's radius R_\odot (e.g. Christensen-Dalsgaard & Thompson, 2007; Howe, 2009, & refs). The tachocline appears to be centred in the stably stratified radiative envelope, at $0.69R_\odot$, but possibly straddles the boundary with the convection zone, particularly in high latitudes (e.g. Basu & Antia, 2003). In fact, Basu & Antia found that, whereas the bottom of the tachocline is very nearly spherical, the top of the tachocline is prolate, although their results are also consistent with a discontinuous change in the tachocline thickness at the zero-shear latitudes $\approx \pm 30^\circ$.

Superimposed on the convection zone's differential rotation are the so-called “torsional oscillations” first observed at the surface by Howard & LaBonte (1980). These are bands of prograde and retrograde motion that propagate equatorward in low latitudes and poleward in high latitudes, with period of approximately 11 years. They are believed to be closely connected to the Sun's magnetic cycle (see §2.5). Helioseismology reveals that these bands occupy at least the outer 60 Mm of the convection zone (e.g. Antia & Basu, 2000), and may extend all the way to be the base of the convection zone in high latitudes (Vorontsov *et al.*, 2002). There is some evidence that the low latitude oscillation propagates upward, as well as equatorward (Basu & Antia, 2003).

Howe *et al.* (2000) found evidence of similar torsional oscillations at the base of the low-latitude convection zone, but with a period of 1.3 years. The angular velocity variations were most pronounced either side of the tachocline, with one band of oscillation at $0.63R_\odot$, and another at $0.72R_\odot$; the two bands oscillate out of phase, such that the shear variations are largest in the tachocline. The existence of tachocline oscillations has significant implications for theories of the solar dynamo (see §2.5). However, subsequent studies have failed to confirm the presence of these oscillations (e.g. Antia & Basu, 2000; Basu & Antia, 2003; Howe *et al.*, 2007). It is possible that the oscillations switched off in 2001, around the time of maximum solar activity (Howe *et al.*, 2007), and may reappear with the new solar cycle.

The early measurements made using helioseismology suggested that the Sun's core, below about $0.2R_\odot$, rotates significantly faster than the outer layers (e.g. Claverie *et al.*, 1981). However, subsequent studies have failed to yield consis-

tent measurements for the rotation rate in this region. In addition, the rotation rate close to the rotation axis is not well constrained by the observations (see figure 2.1). All data gathered in the last three decades is consistent with uniform rotation throughout the radiative interior, with an interior angular velocity $\Omega_i \approx 2.7 \times 10^{-6} \text{s}^{-1}$ (see [Howe, 2009](#), for a review).

Perhaps the most important observation concerning the Sun’s interior rotation is that the average angular velocity over each spherical surface is roughly the same, even within the differentially rotating convection zone. This demonstrates that the spin-down of the solar surface by magnetic braking has been efficiently communicated throughout the interior, and can help us to decide which (if any) of the angular momentum transport mechanisms mentioned in §1.4 are predominant in the solar interior.

However, helioseismology has also revealed some surprising features of the Sun’s interior rotation. Prior to the advent of helioseismology, the existence of the tachocline, i.e. the sharp transition from differential to uniform rotation, had not been anticipated.² In the following sections we review various attempts to answer the following questions:

1. What is the origin of the convection zone’s differential rotation?
2. How is uniform rotation maintained in the radiative envelope?
3. Why is the tachocline so thin?

2.3.1 The influence of rotation

The differential rotation within the Sun’s convection zone must, in some fashion, be driven by the turbulent convection within that region. Although a complete description of this process is lacking, it is well known that weakly nonlinear, rapidly rotating (quasi-geostrophic) convection in spherical geometry produces the kind of “equatorial acceleration” (i.e. latitudinal differential rotation)

²Although the tachocline bears a superficial resemblance to [Spiegel’s](#) tachycline (§1.4.2), the tachycline was expected to thicken over time, and by the Sun’s present age would extend most of the way to the Sun’s core — see §2.4.

observed at the solar surface. In that case, the phenomenon is attributed to the “banana shape” of the convective rolls in low latitudes, which implies an anisotropic Reynolds stress that transports angular momentum equatorward (e.g. [Busse & Hood, 1982](#)). This behaviour survives into the nonlinear regime provided that the convection is still “strongly influenced” by rotation (e.g. [Gilman, 1977](#)). However, the rotation profile produced in such cases is usually subject to the Taylor–Proudman constraint, i.e. the angular velocity contours are aligned with the rotation axis. By contrast, the Sun’s angular velocity contours are more “conical” (see figure 2.2).

Over the last 30 years many studies of rotating convection have sought to explain the dynamics behind the convection zone’s differential rotation (for a more extensive review, see [Miesch, 2005](#)). Most of these fall into one of two categories: direct numerical simulations and mean-field models. Here we will focus on direct numerical simulations. As mentioned above, numerical simulations of rotating

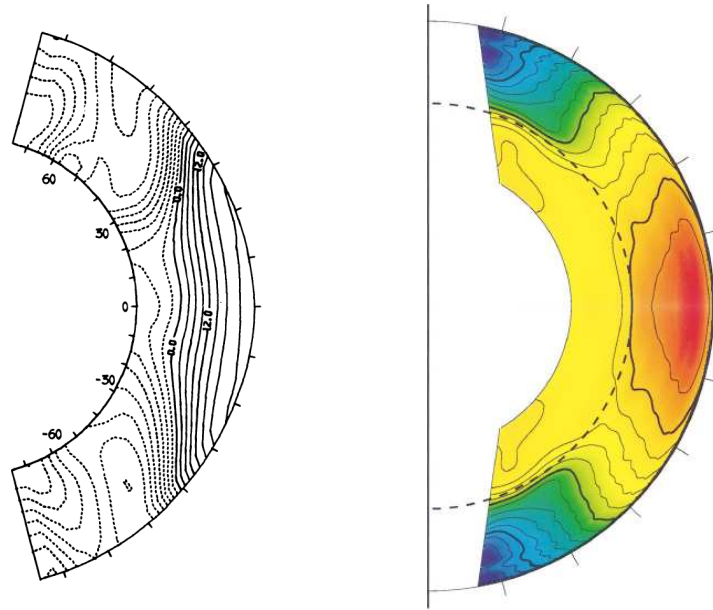


Figure 2.2: The convection zone’s angular velocity contours. The left panel shows the numerical model of [Gilman & Miller \(1981\)](#), in which the contours are aligned with the rotation axis, particularly in low latitudes. The right panel shows the real Sun, as inferred from helioseismology, with conical contours inclined at about 30° to the rotation axis.

convection in spherical shells are able, in certain parameter regimes, to produce equatorial acceleration similar to that observed for the Sun. However, the time-averaged angular velocity contours in these simulations tend to be aligned with

the rotation axis. The early computational models considered only Boussinesq fluids, for reasons of computational ease, and therefore did not include the effects of compressibility. But such effects are expected to be significant in the convection zone, particularly in its outer part, where the vertical density gradient is steepest. Compressible convection is characterised by narrow, concentrated downflows and broad, weak upflows (Hurlburt *et al.*, 1986; Cattaneo *et al.*, 1991). The downflows can take the form of isolated plumes or connected lanes, depending on the strength of the rotational influence (e.g. Brummell *et al.*, 2002). This suggests that compressible effects might significantly alter the angular momentum transport properties of rotating convection (e.g. Glatzmaier *et al.*, 2009, & refs).

In order to more closely approximate the dynamics of the convection zone, most modern computational models make use of the “anelastic” approximation, which retains the energetics of low Mach number compressibility but filters out acoustic waves (Gough, 1969). In these anelastic models, the quasi-geostrophic convection rolls that characterise rapidly rotating, weakly nonlinear convection in Boussinesq fluids are replaced by more complicated structures with distinct vertical asymmetry. Nonetheless, rotating anelastic convection retains certain properties of its Boussinesq counterpart. Provided that the rotational influence is sufficiently strong, concentrated downflowing lanes with a large north–south extension are found to form in low latitudes. Like the banana-shaped Boussinesq convection rolls, these downflowing lanes are tilted such as to transport angular momentum equatorward (Miesch *et al.*, 2000). Strongly rotating anelastic convection can therefore produce the same equatorial acceleration as strongly rotating Boussinesq convection. However, as with Boussinesq convection, the time-averaged angular velocity contours are found to be roughly aligned with the rotation axis, so the effects of compressibility alone do not overcome the Taylor–Proudman constraint.

It is generally accepted that the Sun’s differential rotation is due to rotationally induced anisotropies in the convective turbulence. However, it has not been conclusively shown in which particular parameter ranges an equatorial acceleration occurs, and whether the rotation profile in these parameter ranges is always Taylor–Proudman. The strength of convection is usually measured in terms of

the Rayleigh number Ra . At sufficiently high Rayleigh number the effects of baroclinicity overcome the Taylor–Proudman constraint (recall §1.2), and the structure of convection is no longer geostrophic. But numerical simulations at such high Rayleigh number typically exhibit an equatorial *deceleration*. Differential rotation of this kind is often called “anti-solar”, and may be the result of global homogenisation of angular momentum by the convective turbulence (e.g. [Aurnou *et al.*, 2007](#)).

It is usually assumed, following [Gilman \(1977\)](#), that convection is “strongly influenced” by rotation when the “convective Rossby number” Ro_c is smaller than unity. This is the Rossby number based on the timescale for the growth of convective elements in the absence of dissipative effects, and can be expressed as

$$Ro_c = \left(\frac{Ra Ek^2}{Pr} \right)^{1/2}, \quad (2.1)$$

where Pr is the Prandtl number and Ek is the Ekman number. For fixed Prandtl number, the condition $Ro_c \lesssim 1$ implies that the transitional Rayleigh number Ra_t , below which convection is “strongly influenced” by rotation, is proportional to Ek^{-2} .

More recently, [King *et al.* \(2009\)](#) have argued that convectively unstable systems will naturally adopt whichever form of convection allows the more efficient transport of heat, which can be quantified by the Nusselt number, Nu . Laboratory and numerical experiments suggest that, for fixed Prandtl number, the Nusselt number in non-rotating ($Ek = \infty$) convection is proportional to $Ra^{2/7}$, whereas for quasi-geostrophic ($Ek \rightarrow 0$) convection the Nusselt number is proportional to $Ra^{6/5} Ek^{8/5}$. [King *et al.* \(2009\)](#) therefore argue that the transitional Rayleigh number Ra_t must obey the relation

$$Ra_t^{2/7} \propto Ra_t^{6/5} Ek^{8/5} \quad (2.2)$$

$$\Rightarrow Ra_t \propto Ek^{-7/4}. \quad (2.3)$$

This implies that the transitional Nusselt number, Nu_t say, is proportional to $Ek^{-1/2}$. Furthermore they show that this dependence of Nu_t on Ek can be explained by a simple boundary layer argument. Whether the Prandtl number

dependence of the transition can be similarly explained is unclear.

Any argument based only on parameter values, with no regard to either geometry or boundary conditions, is likely to be overly simplistic. But taken at face-value, the scaling arguments above suggest that in the (narrow) parameter range $Ek^{-7/4} \ll Ra \ll Ek^{-2}$ the structure of convection will be non-geostrophic (i.e. non-Taylor–Proudman), and yet Coriolis effects will be significant on the timescale of the convective motions. The existence of such a regime has not been demonstrated, however.

2.3.2 Thermal-wind

If we assume that both hydrostatic balance and thermal-wind balance hold robustly within the solar interior, then we can use the rotation profile shown in figure 2.1, together with equation (1.1), to calculate the density distribution, and hence the temperature distribution, over every horizontal surface. From the qualitative pattern of rotation shown in figure 2.1 we anticipate that, on each horizontal surface, the temperature increases from equator to pole. In the Sun, the pressure surfaces are very nearly spherical (more so than the density and temperature surfaces), so we also expect to find “warm polar anomalies” on each spherical surface. These anomalies will be most pronounced in the tachocline, where axial variations in the angular velocity are greatest; [Miesch \(2005\)](#) estimated that the base of the convection zone is roughly 5K warmer at the poles than at the equator, although this estimate is sensitive to any errors in the rotation profile obtained by helioseismology. By directly imposing a latitudinal entropy gradient at the base of the convection zone in their simulations, corresponding to a temperature increase of about 10K from equator to pole, [Miesch *et al.* \(2006\)](#) were able to produce angular velocity contours in rough agreement with those observed in the Sun. This suggests that the interaction between the convection zone and the tachocline may play an essential role in determining the rotational profile in the solar interior.

[Miesch *et al.* \(2006\)](#) suggested two different physical explanations for the presence of warm polar anomalies in the convection zone. The first, which they called “thermal forcing”, supposes that the influence of rotation reduces the convective

heat flux at certain latitudes, and hence produces latitudinal variations in the time-averaged temperature profile. Thermal forcing of this kind has been incorporated successfully into mean-field models (e.g. [Kitchatinov & Rüdiger, 1995](#)) as a means to overcome the Taylor–Proudman constraint. The other explanation, which [Miesch *et al.*](#) called “mechanical forcing”, relies on the interaction between the convection zone and the stably stratified tachocline. Whatever process drives the convection zone’s differential rotation will also gyroscopically pump mean meridional circulations (MMCs) that burrow into the tachocline (see §4.2.6 and appendix B). These circulations are expected to be downwelling near the poles (see §1.4.2 and further discussion in §2.4). Within the tachocline, these downwelling flows will produce warm polar anomalies by adiabatic compression, i.e. advection of the background entropy profile. This process has been observed in the mean-field model of [Rempel \(2005\)](#).

Although [Miesch *et al.*](#) considered how thermal or mechanical forcing might drive the convection zone and tachocline towards a state of thermal–wind balance, they did not attempt to construct a complete picture of the balanced system. However, if we assume that the anomalous polar heating required to explain the Sun’s angular velocity profile does indeed originate in the tachocline, then it is possible to make a strong statement about the MMCs in that region. Since the stably stratified tachocline is a thermally relaxing system, departures from local radiative equilibrium will tend to relax back toward zero. To maintain a warm anomaly near the pole, there has to be persistent adiabatic compression by downwelling. This point was recognised much earlier by [Gough & McIntyre \(1998, see §4.2.1\)](#). In principle the required downwelling can be estimated from the magnitude and structure of the warm anomaly, which in turn can be estimated from the Sun’s rotation profile, as described above. In this fashion, [Gough & McIntyre](#) estimated a downwelling velocity of $10^{-5} \text{ cm s}^{-1}$ in the polar tachocline. To make a more precise estimate we would need a more accurate measurement of the shear in the tachocline.

2.4 The tachocline

The most puzzling feature of the Sun’s rotation is the thinness of the tachocline. As described in chapter 1, we expect any differences between the rotation rates of the convection zone and the radiative envelope to gyroscopically pump mean meridional circulations (MMCs) that burrow into the stably stratified interior. These MMCs transport angular momentum, and so the burrowing would cause the convection zone’s differential rotation to spread into the interior. For the deep interior to remain in uniform rotation, the MMCs driven at the base of the convection zone must somehow be prevented from burrowing into the radiative envelope, and thereby confined to the tachocline.

The problem of confining the convection zone’s MMCs was first elucidated by [Spiegel & Zahn \(1992\)](#), in the first paper on the tachocline. They described, using a laminar, hydrodynamic model, how MMCs driven at the base of the convection zone seek to establish a Taylor–Proudman state within the radiative envelope, leading to a thickening of the tachocline on the local Eddington–Sweet timescale (1.5). This is the same “radiative spreading” process described in chapter 1. [Spiegel & Zahn](#)’s results were confirmed by the numerical model of [Elliott \(1997](#), see figure 2.3); see also §4.2.6. If this spreading had been active throughout the Sun’s main-sequence lifetime, including during the early part of the main sequence when the Sun’s faster rotation made the burrowing tendency stronger, then the MMCs and differential rotation would by now have burrowed approximately half-way to the centre of the Sun. This result is not compatible with the helioseismic data. We must therefore conclude that some additional mechanism, absent from their laminar, hydrodynamic model, acts to stop the burrowing of the tachocline’s MMCs, and thereby maintains the uniform rotation of the radiative envelope.

The tachocline’s MMCs, which are gyroscopically pumped by turbulent stresses in the convection zone, can be prevented from burrowing only by compensating gyroscopic pumping within the tachocline. That is, angular momentum must be efficiently redistributed in the tachocline so as to precisely balance the anti-frictional redistribution of angular momentum in the layers above. The (mathematically) simplest mechanism that can redistribute angular momentum in this way is a large horizontal viscosity, which was the mechanism invoked by [Spiegel](#)

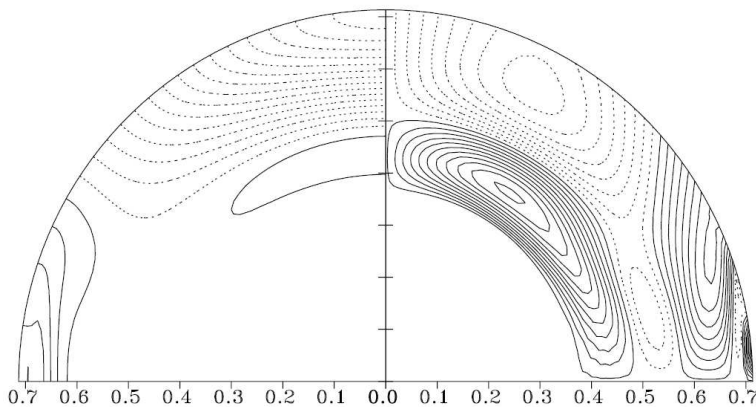


Figure 2.3: Radiative spreading in the solar interior, from the model of [Elliott \(1997\)](#). The left panel shows how deeply the convection zone’s prograde (solid contours) and retrograde (dashed contours) differential rotation burrow after one solar age. The right panel shows the MMCs that produce this burrowing, with dashed contours indicating anti-clockwise circulation.

& [Zahn](#) to halt radiative spreading in their model. They assumed that the combination of latitudinal shear and stable stratification in the tachocline would produce predominantly horizontal hydrodynamic turbulence, i.e. turbulent motions largely confined to horizontal surfaces. They further assumed that the turbulence would redistribute angular momentum in the manner of a large horizontal eddy viscosity (see also [Zahn, 1992](#)). However, several questions have subsequently been raised regarding this turbulence model. Firstly, it is not clear whether the shear in the tachocline is able to sustain turbulence. Many studies have examined the possibility of hydrodynamic and magnetohydrodynamic (MHD) instability in the tachocline (e.g. [Gilman & Cally, 2007](#); [Ogilvie, 2007](#); [Parfrey & Menou, 2007](#); [Spruit, 1999](#), see appendix F). As yet, there seems to be no consensus as to which instabilities are present, and whether they can lead to sustained turbulence in the tachocline.

Secondly, the kind of horizontal, shear-driven, hydrodynamic turbulence proposed by [Spiegel & Zahn](#) has no tendency to act like a viscosity. Instead, the horizontal turbulent eddies act to locally homogenise potential vorticity (PV), which can produce distinctly “anti-frictional” effects (e.g. [McIntyre, 1994, 2003](#), & refs). In the context of the tachocline, such turbulence would probably act to smooth any large extrema in the PV distribution, bringing the system to a marginally stable state without enforcing uniform rotation ([Garaud, 2001](#)).

On the other hand, horizontal MHD turbulence behaves rather differently from its hydrodynamical counterpart, and might well be free from the anti-frictional behaviour just described (McIntyre, 2003; Tobias *et al.*, 2007). But even if horizontal MHD turbulence can mix angular momentum locally, it would need to act efficiently over all latitudes in the tachocline in order to prevent radiative spreading. And even if horizontal turbulence is assumed to act at all latitudes and depths within the radiative interior, an additional mechanism must then be invoked to explain the lack of *radial* shear in that region.

Given the difficulties with using turbulence to explain the radiative envelope’s uniform rotation, it seems worth considering whether the other mechanisms for angular momentum transport mentioned in chapter 1 might provide a more plausible explanation. For example, internal gravity waves can transport angular momentum over large distances within the stably stratified interior (§1.4.3). If the amplitude and spectrum of this wave generation were finely tuned *over all latitudes*, then the resulting angular momentum transport could prevent the tachocline’s MMCs from burrowing into the radiative envelope. However, this situation seems unlikely to be realised within the solar interior, particularly in the early, faster rotating Sun when the burrowing tendency was stronger.

Nevertheless, several studies have advocated gravity waves as the explanation for the Sun’s uniform interior rotation (e.g. Talon *et al.*, 2002; Charbonnel & Talon, 2007, & refs). These studies assume, following Zahn (1992), that horizontal turbulence is able to enforce uniform rotation over each horizontal surface, and therefore seek only to describe how gravity waves can act to reduce the interior’s *radial* shear. By assuming a particular spectrum for the wave generation, which is based on the spectrum of turbulence in the lower convection zone, and by introducing a large turbulent viscosity into any regions of radial shear, the overall effect of angular momentum transport by gravity waves is found to be a smoothing of the radial rotation profile. However, it is frequently argued (e.g. Dintrans *et al.*, 2005, & refs) that the main source of internal gravity waves in the radiative envelope is convective overshoot, a source which is neglected in these models. Overshooting convection typically generates a broad-band spectrum of gravity waves (Hurlburt *et al.*, 1986; Rogers & Glatzmaier, 2006), and so would probably induce “anti-frictional” angular momentum transport (e.g. McIntyre,

1994; Gough & McIntyre, 1998; Rogers *et al.*, 2008). Furthermore, these models do not take into account Coriolis effects on either the generation or the propagation of the waves.

A model of gravity wave generation and dissipation in the radiative interior that allows for latitudinal shear, as well as Coriolis effects, is currently being developed (see Mathis, 2009), but results are not yet available. It is worth noting that the presence of a global-scale magnetic field in the radiative interior would also significantly alter both the generation and the propagation of the waves, as well as their angular momentum transport properties.

Having recognised all of the difficulties associated with purely hydrodynamical models of the tachocline, Gough & McIntyre (1998) concluded that the only mechanism that can plausibly explain the uniform rotation of the radiative envelope is a global-scale interior magnetic field. The impact of such a magnetic field on angular momentum transport was mentioned in §1.4.4, and is discussed in detail in the next chapter. In chapter 4 we give a summary of the Gough & McIntyre model.

2.5 Dynamo theory

The window into the Sun's interior rotation provided by helioseismology has significantly influenced theories of the solar dynamo and the solar cycle. In this section we briefly review the historical development of dynamo theory as applied to the Sun. More detailed discussions of dynamo theory can be found in the books by Moffatt (1978) and Krause & Rädler (1980).

As early as 1850 it was known that the number of sunspots on the Sun's surface follows an 11-year cycle, now known as the Schwabe cycle. Subsequently, Hale (1908) and Hale *et al.* (1919) discovered that sunspots are the sites of strong magnetic fields, and that the polarity of sunspot magnetic fields reverses at the start of each 11-year cycle. The Sun therefore has a 22-year magnetic cycle, which is now known as the Hale cycle. Also in 1919, Larmor proposed that the Sun's surface magnetic field is generated by a hydromagnetic dynamo mechanism.

The first significant development of dynamo theory was the proof by Cowling (1933) that a dynamo magnetic field must necessarily be non-axisymmetric, which rules out the possibility of simple axisymmetric dynamos. In an axisymmetric system, the action of differential rotation can twist poloidal magnetic field lines to generate a toroidal field, but there is no mechanism that can regenerate the poloidal field from the toroidal field. A possible solution to the dynamo problem was proposed by Parker (1955a). He noted that, in a rapidly rotating turbulent system such as the Sun’s convection zone, Coriolis effects lead to cyclonic (i.e. helical) motions within the fluid. He then showed that certain small-scale helical motions, in the presence of magnetic diffusion, can regenerate a large-scale poloidal field from a large-scale toroidal field.

Parker’s idea, that small-scale turbulence can regenerate a large-scale poloidal field, was developed into a formal mathematical theory by Steenbeck *et al.* (1966), which came to be known as “mean-field electrodynamics”. Today, the generation of poloidal field by small-scale turbulence, and the generation of toroidal field by differential rotation, are known as the “alpha” (α) and “omega” (ω) effects respectively, following the notation employed by Steenbeck & Krause (1969).

It is now generally accepted that the Sun’s 22-year magnetic cycle results from a large-scale $\alpha\omega$ -dynamo process operating within the convection zone, and that sunspots are the surface manifestation of the dynamo field. The Sun’s interior differential rotation generates a strong toroidal magnetic field, which becomes buoyantly unstable (Parker, 1955b) and rises to the surface in the form of “magnetic flux tubes”. Upon reaching the surface, the flux tubes extend into the Sun’s atmosphere as coronal loops. Sunspots are the footpoints of these loops on the solar surface. The strong magnetic field in sunspots inhibits convection, and so sunspots are cooler, and hence darker, than the rest of the solar surface. This model of sunspot formation also offers an explanation for many other observed properties of sunspots (Parker, 1955b), including their bipolarity and near east-west orientation.

However, it can be argued that any dynamo magnetic field within the bulk of the convection zone will be brought to the surface, by a combination of magnetic buoyancy and turbulent convection, on a timescale of months, rather than years (Parker, 1975; Schmitt, 1993, & refs). This suggests that the toroidal component

of the dynamo field must be located in a boundary layer the base of the convection zone (Spiegel & Weiss, 1980). Helioseismology provides additional support for this view, since it shows that the Sun's differential rotation is most pronounced at the base of the convection zone, i.e. within the tachocline. Spiegel & Weiss therefore proposed that the solar dynamo operates entirely within the stably stratified overshoot layer beneath the convection zone, within which the alpha effect arises from the helicity of overshooting convective plumes.

However, there are difficulties in reconciling sunspot observations with a model of the solar dynamo based entirely at the base of the convection zone. Since very few sunspots are observed at latitudes $\gtrsim 35^\circ$, toroidal flux tubes must rise almost vertically through the convection zone, rather than parallel to the Sun's axis of rotation (Parker, 1993, & refs). This requires the toroidal field strength to be $\sim 10^5$ gauss at the base of the convection zone, in order for Lorentz forces to dominate Coriolis forces during the buoyant rise of the flux tubes. However, the magnetic energy associated with a field of this strength significantly exceeds the kinetic energy associated with turbulent convective motions near the base of the convection zone. The Lorentz force from the field is therefore expected to suppress any turbulence in its vicinity, and thus “quench” the alpha effect (Parker, 1993, & refs). Indeed, in a system with a large magnetic Reynolds number, such as the convection zone, alpha-quenching is expected to occur well before the magnetic energy reaches equipartition with the turbulent kinetic energy (Cattaneo & Hughes, 1996, & refs).

A possible resolution of the alpha-quenching problem was proposed by Parker (1993), (see also Charbonneau & MacGregor, 1997). Parker proposed an “interface dynamo” in which the alpha and omega effects occur in spatially distinct regions, either side of the interface between the convection zone and radiative envelope. In this model, the toroidal magnetic field is significantly weaker in the region above the interface, as a result of turbulent magnetic diffusion within the convection zone. Alpha quenching is therefore averted within this region. Transport of poloidal and toroidal field across the interface is mediated by a combination of laminar and turbulent diffusion. The solar cycle and torsional oscillations can then be explained in terms of “dynamo waves” that propagate at the interface between the alpha and omega regions.

An alternative resolution of the alpha-quenching problem can be found in the model of Wang & Sheeley (1991), which is based on earlier work by Babcock (1961) and Leighton (1969). In this “Babcock–Leighton” or “flux-transport” dynamo model, generation of poloidal field³ is attributed both to the twisting of rising flux tubes by Coriolis forces and to the redistribution of magnetic flux by cyclonic motions and magnetic diffusion over the upper surface of the convection zone. This is not strictly an alpha effect, because the poloidal field is generated by large-scale motions rather than small-scale turbulence. Recent flux-transport dynamo models have placed increasing emphasis on the role of the convection zone’s mean meridional circulation in transporting the poloidal field from the surface to the base of the convection zone (e.g. Dikpati & Charbonneau, 1999). In these recent models, the turnover time of the convection zone’s meridional circulation is the main factor determining the period of the solar cycle, and the Sun’s torsional oscillations are attributed to meridional advection rather than a dynamo-wave mechanism.

The Sun’s dynamo field, which reverses every 11 years, must remain disconnected from the pseudo-steady interior magnetic field \mathbf{B}_i needed to explain the interior’s uniform rotation.⁴ This requires the existence of some mechanism that can confine the interior magnetic field against diffusion, as will be discussed in detail in chapter 4. If the interior field is sufficiently strong then it might still influence the solar cycle, perhaps inducing a 22-year cyclicity in solar activity (Levy & Boyer, 1982). There is some observational evidence for such cyclicity (Mursula *et al.*, 2001, & refs), although an interior magnetic field is not the only possible explanation (e.g. Charbonneau *et al.*, 2007). In chapter 3 we discuss the origin of the Sun’s interior magnetic field and its angular momentum transport properties.

³The generation of *toroidal* field is still attributed to the omega effect, i.e. to the action of differential rotation.

⁴Walén (1946) proposed that the solar cycle might arise from global Alfvénic oscillations of an interior magnetic field, but in that case the Sun’s differential rotation would also reverse every 11 years — see §3.2.

Chapter 3

The Magnetic Interior

3.1 The Sun’s fossil field

In the neighbourhood of our solar system, the interstellar magnetic field has a strength of roughly 10^{-6} gauss. The molecular cloud from which the Sun formed in all likelihood contained a magnetic field of similar strength, which would have been amplified during the Sun’s gravitational collapse. It is not known to what extent this primordial field was modified by deep convection during the Sun’s pre-main sequence Hayashi phase, but observations of T Tauri stars suggest that surface field strengths of 10^3 gauss are typical (e.g. [Bouvier *et al.*, 2007](#)).

Some component of the Sun’s primordial magnetic field was probably “fossilised” in the deep interior following the retreat of the convection zone (e.g. [Parker, 1981](#)). Since the global-scale magnetic diffusion time for the Sun is roughly 10^{10} years, comparable to the Sun’s present age, it is likely that some global-scale remnant of this field \mathbf{B}_i still exists within the stably stratified interior, with a field strength of perhaps a few hundred gauss (e.g. [Mestel & Weiss, 1987](#), & refs). However, only torque-free magnetic field configurations can persist on such long timescales (e.g. [Chandrasekhar & Prendergast, 1956](#)), so the field configuration in the Sun’s stably stratified interior cannot be deduced from magnetic diffusion alone.

Recently, [Braithwaite & Spruit \(2004\)](#) numerically modelled the evolution of fos-

sil fields in Ap stars (see also [Braithwaite & Nordlund, 2006](#)). By allowing the internal field to evolve from a random initial condition, they found that the star established a roughly torque-free equilibrium on the Alfvénic timescale — i.e. the global travel time of an Alfvén wave through the interior. The equilibrium configuration for the magnetic field was similar to that suggested by [Prendergast \(1956\)](#), a roughly axisymmetric dipole with a toroidal component in a neighbourhood of the neutral ring (see figure 3.1). The presence of the toroidal component is necessary, since any purely poloidal field configuration would be unstable ([Braithwaite & Nordlund, 2006](#), & refs).

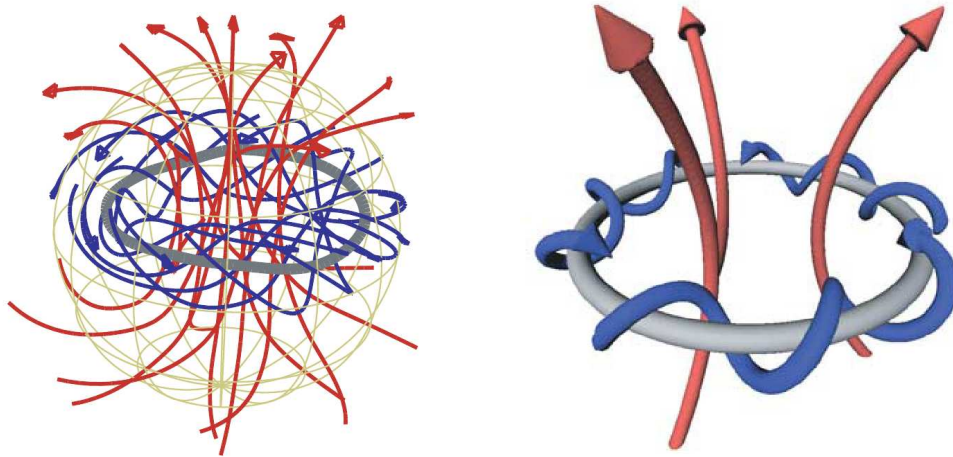


Figure 3.1: A possible configuration for the fossil magnetic field \mathbf{B}_i inside an Ap star ([Braithwaite & Spruit, 2004](#)). The field is a roughly axisymmetric dipole. The field in the insulating region surrounding the star is purely poloidal. Below the surface of the star, the neutral ring of the dipole is stabilised by a band of toroidal field, shown in blue. The right frame shows a simplified schematic of the field configuration.

In the following sections we suppose that the Sun’s interior fossil field has a similar configuration to that found by [Braithwaite & Spruit](#), and describe the effect of this field on angular momentum transport within the Sun.

3.2 The Ferraro constraint

As described in §1.3, in a system with a strong magnetic field the rotation must be constant on each “Ferraro surface”, i.e. on the surface of revolution of each field line. The presence of a magnetic field \mathbf{B}_i within the Sun’s radiative interior can

therefore provide a natural explanation for the uniform rotation of that region. Any initial deviation from a Ferraro state will deform the field lines, producing Alfvén waves. The simplest model of this process supposes that the field is axisymmetric, and that the fluid motions are purely rotational, as in the model of [Charbonneau & MacGregor](#) (recall §1.4.4). If we neglect viscosity and magnetic diffusion, then each “Ferraro surface” oscillates independently of the others, and with its own discrete set of harmonic frequencies, determined by the poloidal Alfvén speed within the surface ([Plumpton & Ferraro, 1955](#)). These global Alfvén modes, known as “torsional oscillations”,¹ were first studied by [Walén \(1946\)](#) as a possible explanation for the 22-year solar magnetic cycle (§2.5).

Since each Ferraro surface oscillates independently of its neighbours, the oscillations of neighbouring surfaces are generally not in phase, leading to large transverse gradients in the azimuthal velocity and magnetic fields; this is known as “phase mixing” ([Charbonneau & MacGregor, 1993](#)). Therefore the presence of weak magnetic diffusion rapidly damps the oscillations, leading to a steady Ferraro state. In the absence of viscosity, there can be no angular momentum transport between neighbouring Ferraro surfaces, so in general the steady state will be differentially rotating. However, the system may be subject to various hydrodynamic or MHD instabilities (see references in §2.4), leading to enhanced diffusion of both magnetic field and angular momentum. Allowing for finite meridional motions also introduces angular momentum coupling between the Ferraro surfaces, and may further enhance the damping of torsional oscillations (e.g. [Mestel & Weiss, 1987](#)).

The picture just described applies if the magnetic field \mathbf{B}_i is axisymmetric. For a non-axisymmetric field, only uniform rotation is permitted in the steady state. However, under some circumstances we would expect the field to be very nearly axisymmetric. For example, if the field were initially quite weak, a few gauss or less, and non-axisymmetric, then the action of differential rotation would wind up a predominantly toroidal field with large meridional gradients in the toroidal field strength. Magnetic diffusion would then rapidly eliminate the non-axisymmetric component of the field; this process is known as “rotational smoothing” ([Spruit, 1999](#), & refs).

¹The torsional oscillations of the interior magnetic field should not be confused with the torsional oscillations of the convection zone described in §2.3.

3.3 The magnetic confinement problem

As mentioned in §2.2, the early measurements made using helioseismology suggested that the Sun’s core rotates at least twice as fast as the radiative envelope. [Mestel & Weiss \(1987\)](#) argued, based on the picture put forward in §3.2, that the presence of a magnetic field in the radiative interior is incompatible with such rapid core-rotation, unless the magnetic field is very weak (10^{-2} gauss or less). They suggested that the helioseismological measurements were in error, and that in fact the entire region below the convection zone is locked into uniform rotation by a global-scale fossil magnetic field \mathbf{B}_i . They assumed that the magnetic field would be confined to the radiative interior by “magnetic flux expulsion” from the convection zone ([Weiss, 1966](#)). This mechanism is described in §4.1.

[Rüdiger & Kitchatinov \(1997\)](#) constructed the first quantitative model of the interaction between a magnetic field in the radiative envelope and the differential rotation of the convection zone. Their model was similar to the spin-down model of [Charbonneau & MacGregor \(1993\)](#), except that the convection zone’s differential rotation was directly imposed at the top of the radiative envelope. The poloidal component of \mathbf{B}_i , which they took to be an axisymmetric dipole, was imposed throughout the calculation, and meridional flows were forbidden. [Rüdiger & Kitchatinov](#) assumed that the turbulence in the convection zone would act as a large eddy diffusivity, and thereby expel any magnetic field from that region (see §4.1). They therefore only considered magnetic field configurations with no direct magnetic coupling between the convection zone and radiative envelope. In their simulations, the convection zone’s differential rotation spread into the radiative envelope by viscous diffusion, and then proceeded to wind up the interior field. A balance was achieved once the Lorentz torque from the magnetic field became large enough to balance the viscous torque. In cases where the imposed poloidal field was sufficiently strong ($|\mathbf{B}_i| \gtrsim 10^{-4}$ gauss), the differential rotation within the radiative envelope was confined to a thin shear-layer resembling the tachocline. This shear-layer can be described by a simple boundary-layer theory ([Rüdiger & Kitchatinov, 1997](#)) in which we approximate the density ρ , viscosity ν and magnetic diffusivity η as constant. Since the density is assumed constant ($\rho \approx 0.21 \text{ g cm}^{-3}$, see appendix A), we may measure the magnetic field \mathbf{B} in units of Alfvén speed, with 1 gauss corresponding to approximately 0.6 cm s^{-1} .

The governing equations are the azimuthal components of the momentum and induction equations, which can be expressed in cylindrical polar coordinates as

$$0 = \frac{1}{r} \mathbf{B}_i \cdot \nabla (r B_\phi) + \nu \left(\nabla^2 - \frac{1}{r^2} \right) u_\phi , \quad (3.1)$$

$$0 = r \mathbf{B}_i \cdot \nabla (u_\phi / r) + \eta \left(\nabla^2 - \frac{1}{r^2} \right) B_\phi . \quad (3.2)$$

Away from the poles, the dipolar field \mathbf{B}_i is roughly horizontal below the base of the convection zone. We therefore expect that

$$\mathbf{B}_i \cdot \nabla \sim |\mathbf{B}_i| / L , \quad (3.3)$$

where L is the horizontal scale of the imposed differential rotation, which we take to be the radius of the tachocline, $0.7R_\odot$. Assuming that the thickness of the steady-state shear-layer is $\Delta \ll L$, we also expect that

$$\nabla^2 \sim 1 / \Delta^2 . \quad (3.4)$$

Hence it is readily verified from (3.1) and (3.2) that

$$\Delta \sim \left(\frac{\nu \eta L^2}{|\mathbf{B}_i|^2} \right)^{1/4} , \quad (3.5)$$

$$B_\phi \sim (\nu / \eta)^{1/2} u_\phi . \quad (3.6)$$

So the thickness of the shear-layer decreases as the strength of the poloidal field increases, and becomes $\lesssim 0.05R_\odot$ when

$$|\mathbf{B}_i| \gtrsim \frac{\nu \eta (0.7R_\odot)^2}{(0.05R_\odot)^4} \quad (3.7)$$

$$\approx 4 \times 10^{-7} \text{ cm s}^{-1} . \quad (3.8)$$

So a poloidal field with $|\mathbf{B}_i| \gtrsim 10^{-6}$ gauss should be sufficient to confine the convection zone's differential rotation within a layer as thin as the tachocline. From (3.6) we see that the magnitude of the toroidal field wound up in the shear-layer is essentially independent of $|\mathbf{B}_i|$. The typical magnitude of u_ϕ is determined by the imposed differential rotation at the top of the radiative envelope, which is

about 30% of the interior rotation rate Ω_i , and so

$$u_\phi \sim 0.3\Omega_i L . \quad (3.9)$$

This leads to an estimate for B_ϕ of around 10^4 gauss — considerably larger than the lower bound on $|\mathbf{B}_i|$ found above. However, a strongly toroidal field would probably be unstable (see appendix F).

The model of Rüdiger & Kitchatinov demonstrates that an interior magnetic field can prevent the *viscous* spread of the convection zone’s differential rotation into the interior. However, the radiative spreading process described in §2.4 is the result of meridional flows seeking to establish a Taylor–Proudman state, and has no connection with viscous diffusion. In the model of Rüdiger & Kitchatinov meridional flows are artificially suppressed, and so Coriolis effects are absent. We might say that their model describes a *non-rotating* Sun. Nonetheless, their model provides a simple illustration of how an interior magnetic field is able to enforce uniform rotation, provided that the field is confined (i.e. predominantly horizontal) beneath the convection zone.

Subsequently, MacGregor & Charbonneau (1999) considered a very similar model, but where now the interior magnetic field \mathbf{B}_i was unconfined, i.e. directly coupled to the convection zone. They found that the convection zone’s differential rotation propagated along the poloidal field lines, rapidly establishing a Ferraro state of differential rotation within the interior (see figure 3.2). This demonstrates that the geometry of the internal field is crucial to determining the pattern of rotation in the interior. In order to explain the sharp transition between uniform and differential rotation at the base of the convection zone, the magnetic field lines must remain nearly horizontal within the outer part of the radiative envelope.

But even if the magnetic field is initially confined in this fashion, over the Sun’s lifetime it can diffuse into the convection zone, whereupon the convection zone’s differential rotation will be rapidly transferred to the interior. This can be called the “magnetic confinement problem”, and has been illustrated by the recent numerical simulations of Brun & Zahn (2006). They modelled the evolution of a dipolar fossil magnetic field within the radiative envelope, using a three-dimensional, anelastic numerical scheme. They modelled the radiative–convective

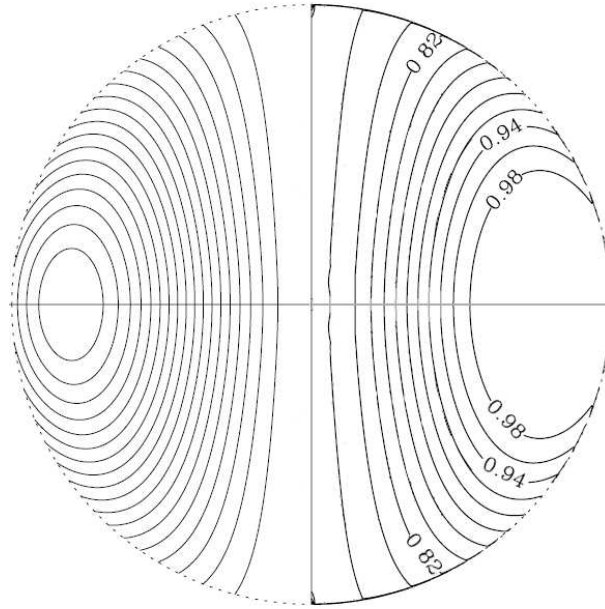


Figure 3.2: The imposed poloidal magnetic field (left panel) and steady-state angular velocity (right panel) in the model of [MacGregor & Charbonneau \(1999\)](#).

interface as a differentially rotating, impenetrable boundary; the differential rotation imposed on this boundary was chosen to represent the differential rotation of the lower convection zone. They found that, as the interior field diffused, it connected to the differentially rotating outer boundary, and communicated this differential rotation into the radiative envelope. This problem was particularly conspicuous in high latitudes, where the convection zone’s slow rotation was transmitted to an “apple-core” region surrounding the axis (see figure 3.3).

In order for the interior magnetic field to enforce uniform rotation within the radiative envelope, a mechanism must be in place to confine the magnetic field, holding the field lines horizontal below the base of the convection zone. Possible mechanisms for achieving magnetic confinement are discussed in the next chapter.

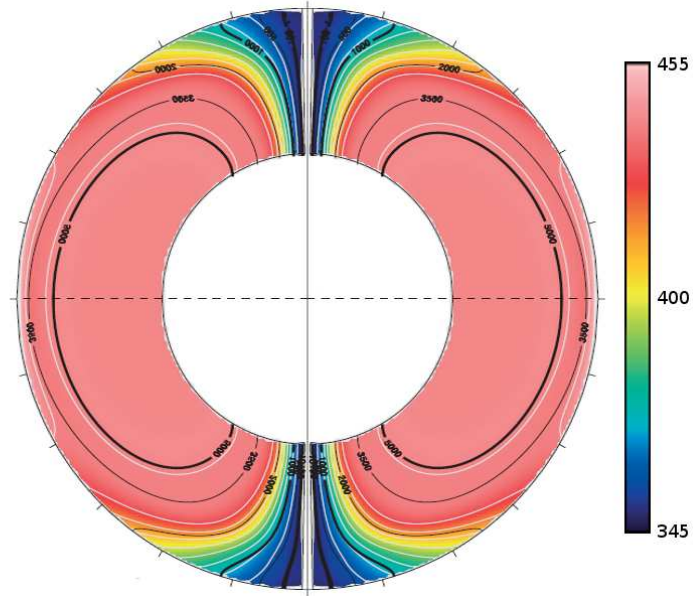


Figure 3.3: If the interior magnetic field \mathbf{B}_i (black lines) is allowed to diffuse into the convection zone, then the convection zone's differential rotation is imprinted on the interior ([Brun & Zahn, 2006](#)). The colours represent angular velocity (units are nHz).

Chapter 4

Magnetic Field Confinement

4.1 Magnetic pumping

The studies of [Mestel & Weiss \(1987\)](#) and [Rüdiger & Kitchatinov \(1997\)](#) both assumed that the Sun’s interior magnetic field would be confined to the radiative interior by the turbulence in the convection zone. They argued that any magnetic field in the convection zone would be characterised by the same small lengthscales and timescales as the convective turbulence, and that therefore the time-averaged mean field would reside entirely within the stably stratified interior.

A simple example of the interaction between convective turbulence and magnetic fields was considered by [Weiss \(1966\)](#). He showed that turbulent eddies enhance the rate of dissipation of magnetic fields, so that magnetic flux becomes concentrated at the boundaries between the eddies. This is often called “magnetic flux expulsion”, i.e. expulsion of magnetic flux from the most turbulent regions of the flow.

A related but separate concept is that of “topological pumping”, first proposed by [Drobyshevski & Yuferev \(1974\)](#). Based on the structure of solar convection — concentrated downwelling lanes separating weak upflowing regions — they argued that horizontal flux tubes in the convection zone would be carried downward by the convection (see also [Tao *et al.*, 1998](#), & refs). Recently, [Tobias *et al.* \(1998\)](#) studied the interaction between turbulent compressible convection and a hori-

zontal *layer* of magnetic field (see also [Dorch & Nordlund, 2001](#), & refs). They performed cartesian-box simulations of a convectively unstable region overlying a stably stratified region. Once the convection was fully developed, a horizontal layer of magnetic field was inserted into the unstable region. They found that much of this field was pumped into the stably stratified region by overshooting convective plumes. They also found that this “magnetic flux pumping” operates only when the convective turbulence is significantly compressible, and therefore vertically asymmetric (recall §2.3.1). However, it is unclear from their simulations whether the pumping results simply from the vertical anisotropy of the turbulence, or whether the presence of the stably stratified layer is also required.

The concepts of flux expulsion and flux pumping are also present in mean-field theory. In that context, mean-field transport is attributed to the antisymmetric component of the “ α -tensor” (e.g. [Roberts & Soward, 1975](#)), which can be expressed in terms of an effective pumping velocity γ ([Rädler, 1968](#)). Pumping can arise from either inhomogeneous turbulence (so-called “diamagnetic pumping”) or density gradients (e.g. [Kitchatinov & Rüdiger, 1992](#)). In fact, inhomogeneous turbulence of itself cannot produce pumping; the turbulence must also be anisotropic. Within the context of mean-field theory it is therefore straightforward to make a distinction between the flux *expulsion* described by [Weiss \(1966\)](#), which occurs even for isotropic turbulence, and the flux *pumping* hypothesised by [Drobyshevski & Yuferev \(1974\)](#). In numerical simulations this distinction may be less clear.

Recently, [Garaud & Rogers \(2007\)](#) performed a numerical simulation of the interaction between a magnetic field \mathbf{B}_i in the solar interior and the turbulence of the convection zone. Their model was of a two-dimensional (non-rotating) “cylindrical Sun” (see figure 4.1). They found that, as the initially confined magnetic field diffused into the convection zone, it was quickly stretched and advected by the turbulent convective eddies, so that no large-scale component survived within the convection zone. However, the structure of the field within the radiative envelope was similar to that found by [Brun & Zahn \(2006, see figure 3.3\)](#). A snapshot of the magnetic field is shown in figure 4.1. After less than one global-scale magnetic diffusion time, significant field-line connection is established with the convection zone in the polar regions, although the field lines remain almost horizontal in

middle and low latitudes. There is no indication of magnetic field being pumped

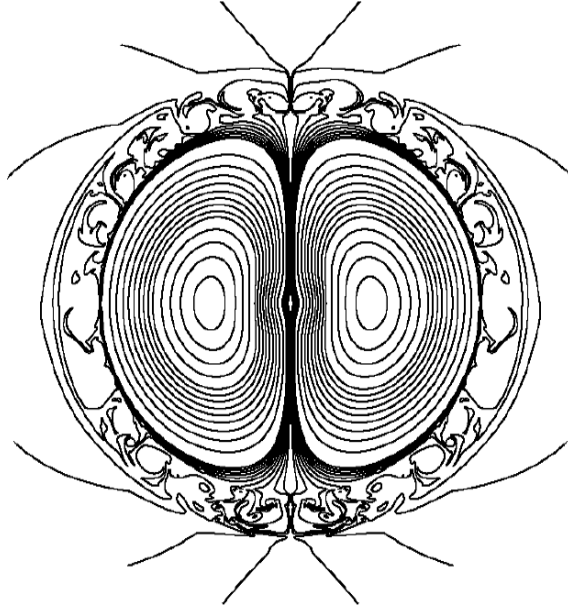


Figure 4.1: A cross-section through the “cylindrical Sun” of [Garaud & Rogers \(2007\)](#). Turbulent eddies destroy any large-scale poloidal magnetic field within the convection zone.

out of the convection zone back into the radiative envelope. This may be because the turbulence is not sufficiently compressible; the parameter regime described by [Tobias *et al.* \(1998\)](#) cannot be matched in a global model.

[Garaud & Rogers](#) hypothesised that, although the interior magnetic field \mathbf{B}_i is able to connect to the convection zone, since the field lines follow an essentially random path through that region they do not transmit any net torque to the interior. However, since the effects of rotation could not be included in their two-dimensional model, it was not possible to directly test this hypothesis. By analogy with the results of [Brun & Zahn \(2006\)](#), it seems likely that the slow rotation of the high-latitude convection zone would be communicated to an apple-core region surrounding the axis in the radiative interior.

The question of whether magnetic flux pumping might act to confine the Sun’s interior magnetic field has also been considered by [Kitchatinov & Rüdiger \(2008\)](#), in the context of an axisymmetric mean-field model. They parametrised the turbulence in the convection zone using a combination of large turbulent magnetic diffusivity and diamagnetic pumping. They found that the interior magnetic field \mathbf{B}_i could be confined, provided that the diamagnetic pumping was suffi-

ciently strong. The model of Kitchatinov & Rüdiger is re-derived (and slightly generalised) in appendix E. The main result is that strong downward pumping at the base of the convection zone leads to an accumulation of horizontal magnetic field at the top of the radiative envelope. This result is at least superficially similar to that of Tobias *et al.* (1998), although as mentioned above the same behaviour was not observed in the model of Garaud & Rogers (2007).

Whether such strong diamagnetic pumping operates at all latitudes within the convection zone, and whether it is directly related to the magnetic flux pumping found by Tobias *et al.*, remains unclear. Intuitively, we would expect pumping to be most effective in middle and low latitudes, where the interior field is horizontal, as in the model of Tobias *et al.* (1998). The pumping efficiency might be further reduced in high latitudes by Coriolis effects (Tobias *et al.*, 2001). We might therefore tentatively conclude that diamagnetic pumping can confine the horizontal field in middle and low latitudes, but that another mechanism may be required in high latitudes. The importance of confining the magnetic field in the high latitude regions is highlighted by the results of Brun & Zahn (figure 3.3).

4.2 Mean meridional circulations (MMCs)

4.2.1 The Gough & McIntyre (GM98) model

The problem of magnetic field confinement was first discussed by Gough & McIntyre (1998, hereafter GM98). They proposed that the Sun’s fossil magnetic field \mathbf{B}_i is confined to the radiative interior by the tachocline’s MMCs, which hold the field in the tachocline in advection–diffusion balance; that is, the upward diffusion of the field is balanced by downward advection by the tachocline’s MMCs. As discussed in §2.3.2, they argued that the pattern of differential rotation observed in the convection zone and tachocline imply the existence of persistent downwelling in high latitudes. They estimated the magnitude of the downwelling velocity U to be $\sim 10^{-5} \text{cm s}^{-1}$ in the stably stratified polar tachocline. Since the magnetic diffusivity η in the tachocline is $\approx 410 \text{cm}^2 \text{s}^{-1}$ (see appendix A), the magnetic advection–diffusion lengthscale δ_η with this velocity is $\eta/U \approx 0.4 \text{Mm}$, which is much thinner than the tachocline. They reasoned that the high-latitude down-

welling therefore confines the interior magnetic field within a magnetic boundary layer of thickness δ_η at the base of the high-latitude tachocline. Henceforth we will refer to this boundary layer as the “magnetic confinement layer”.

The [GM98](#) model comprises three distinct regions:

- Above the magnetic confinement layer, the tachocline is laminar,¹ field-free and in thermal-wind balance.
- Within the magnetic confinement layer, the poloidal field is held in advective–diffusive balance. A toroidal field component, wound up by differential rotation, exerts a prograde Lorentz torque on the fluid, turning the downwelling flow equatorward, and thereby confining the meridional circulation.
- Below the confinement layer, the radiative envelope is stagnant and uniformly rotating, held in isorotation by the interior magnetic field \mathbf{B}_i , which [GM98](#) assumed to be an axial dipole.

[GM98](#) did not provide a complete model of magnetic confinement. In fact, they modelled only a localised, high-latitude region, sufficiently far from the pole that curvature terms could be neglected and the interior magnetic field assumed horizontal. Moreover, they modelled only the deepest extent of the confinement layer, which can be approximated as a linear perturbation to the stagnant, uniformly rotating interior. Their model can therefore be described in terms of the MAC-wave theory set out in appendix C. Following [GM98](#) we neglect viscosity and take the interior magnetic field \mathbf{B}_i to be uniform. The steady-state temperature perturbation T' is then described by the equation

$$\left[(\mathbf{B}_i \cdot \nabla)^4 + \eta^2 (2\boldsymbol{\Omega}_i \cdot \nabla)^2 \nabla^2 \right] \nabla^2 T' - \frac{\eta N^2}{\kappa} (\mathbf{B}_i \cdot \nabla)^2 \nabla_H^2 T' = 0 \quad (4.1)$$

(cf. (C.20)–(C.21) in appendix C). Here, $\boldsymbol{\Omega}_i$ is the constant angular velocity of the interior, κ is the thermal diffusivity, N is the buoyancy frequency and ∇_H^2 is the horizontal Laplacian. Again following [GM98](#), we assume that the system is axisymmetric, and that there is a single latitudinal lengthscale, say L ,

¹Recently, [McIntyre \(2007\)](#) presented a significantly revised version of the [GM98](#) model in which the bulk of the tachocline is subject to Tayler instability — see appendix G.

which is determined by the global geometry of the tachocline (GM98 estimated $L \approx 0.15R_\odot \approx 100\text{Mm}$). We therefore replace $\nabla_H^2 \rightarrow -1/L^2$ in (4.1). Since the interior field \mathbf{B}_i is assumed horizontal, we may also replace $(\mathbf{B}_i \cdot \nabla)^2 \rightarrow -|\mathbf{B}_i|^2/L^2$. For convenience we choose to measure the strength of the field in terms of the “horizontal” Elsasser number

$$\Lambda_H = \frac{|\mathbf{B}_i|^2}{2\Omega_i\eta}, \quad (4.2)$$

which is a dimensionless number. If $\Lambda_H = 1$ then $|\mathbf{B}_i| \approx 8 \times 10^{-2}$ gauss. Since $\delta_\eta \ll L$, we may make the boundary-layer approximation $\nabla^2 \approx \partial^2/\partial z^2$, where z is the vertical coordinate, so that (4.1) becomes

$$\left(\Lambda_H + \frac{L^4}{\Lambda_H} \frac{\partial^4}{\partial z^4} \right) \frac{\partial^2}{\partial z^2} T' = \frac{N^2}{2\Omega_i\kappa} T'. \quad (4.3)$$

In GM98 it was assumed that thermal-wind balance is not modified by the Lorentz force in the confinement layer. As a result of this assumption, rather than (4.3) they obtained the equation

$$\frac{L^4}{\Lambda_H} \frac{\partial^6}{\partial z^6} T' = \frac{N^2}{2\Omega_i\kappa} T'. \quad (4.4)$$

This equation has three independent solutions that decay with depth, and three that grow with depth; the second three violate the assumptions made in the linearisation, and are therefore rejected. The remaining three solutions all decay exponentially with depth on the vertical lengthscale

$$\left(\frac{2\Omega_i\kappa}{\Lambda_H N^2 L^2} \right)^{1/6} L \approx \Lambda_H^{-1/6} \text{Mm}. \quad (4.5)$$

By matching this vertical lengthscale to the magnetic advection–diffusion lengthscale $\delta_\eta = \eta/U$, GM98 were able to directly relate the downwelling velocity U to the strength of the interior magnetic field, which here is quantified by Λ_H . Using their estimates $U \approx 10^{-5} \text{cm s}^{-1}$ and $L \approx 100\text{Mm}$ they deduced that $|\mathbf{B}_i| \approx 1$ gauss.

By comparing (4.3) and (4.4), we find that the results of GM98 are valid only if

$$\Lambda_H^2 \ll \frac{N^2 L^2}{2\Omega_i \kappa} \approx 10^{12}. \quad (4.6)$$

This leads to an upper bound on $|\mathbf{B}_i|$ of approximately 50 cm s^{-1} , or 80 gauss. The results of GM98 are therefore valid, although the margin of error is rather small. In fact, the full equation (4.3) has the same essential property as (4.4): it has three independent solutions that decay with depth, and three that grow with depth. The GM98 picture is therefore qualitatively unaffected by the extra term in (4.3).

4.2.2 The polar regions

In GM98 it was assumed that, in order to confine the tachocline’s MMCs, the interior magnetic field \mathbf{B}_i needed to be accurately horizontal. Near the poles, where the assumed dipolar field is not horizontal, they speculated that the MMCs would burrow into the radiative envelope, forming “polar pits” (see figure 4.2). Such polar pits would have significant implications for lithium burning, as will be described in chapter 6.

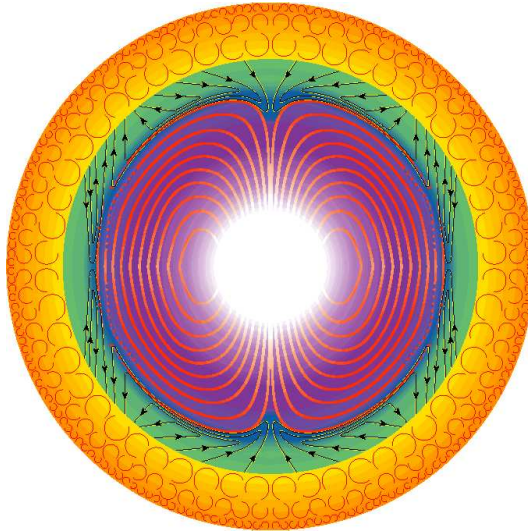


Figure 4.2: An interior dipole \mathbf{B}_i (red lines) confined by the tachocline’s MMCs (black lines with arrows). Near the poles, the MMCs burrow into the radiative envelope, forming polar pits. Adapted from Gough & McIntyre (1998). The thickness of the tachocline (shown in green) has been exaggerated.

To go beyond these speculations, we must formulate a complete and self-consistent model of the magnetic confinement layer that includes the polar regions. This is the ultimate goal of this dissertation. As a first step towards achieving this goal, it is instructive to consider how the regime described by (4.3) changes as we move closer to the pole. The first of GM98’s approximations to break down will be that of horizontal magnetic field. Once the slope of the interior field lines becomes comparable to the aspect ratio of the confinement layer, it is no longer valid to neglect the vertical component of \mathbf{B}_i . Indeed, within some neighbourhood of the pole \mathbf{B}_i must be approximately vertical. Within this neighbourhood we may approximate $(\mathbf{B}_i \cdot \nabla)^2 \approx B_{iz}^2 \partial^2 / \partial z^2$, where B_{iz} is the vertical component of \mathbf{B}_i . Equation (4.1) then becomes

$$\frac{\partial^2}{\partial z^2} \left[\left(\Lambda_V \frac{\partial^2}{\partial z^2} + \frac{1}{\Lambda_V} \nabla^2 \right) L^2 \nabla^2 T' + \frac{N^2}{2\Omega_i \kappa} T' \right] = 0 \quad (4.7)$$

where we have replaced $\nabla_H^2 \rightarrow -1/L^2$ and defined a “vertical” Elsasser number

$$\Lambda_V = \frac{B_{iz}^2}{2\Omega_i \eta} . \quad (4.8)$$

Equation (4.7) supports two independent axisymmetric solutions with non-exponential dependence on z . One corresponds to Ferraro differential rotation; the other corresponds to vertical flows along the field lines, the signature of GM98’s polar pits. The flow perturbs the thermal stratification surfaces, thereby establishing a thermal wind in the radiative envelope. In the laminar, inviscid system described by equation (4.7) there is nothing that can limit the degree of Ferraro differential rotation, nor the depth to which the flow along the field lines can burrow. However, as discussed in §3.2, in the real Sun any differential rotation in the polar regions would be limited by hydrodynamic and MHD instabilities, which introduce angular momentum coupling between the Ferraro surfaces, and allow the flow to leak across the field lines. We would therefore expect the polar pits, and their associated thermal winds, to extend only a finite distance into the radiative envelope,² as indicated in figure 4.2.

²Since helioseismology cannot provide an accurate measurement of the Sun’s angular velocity profile close to the rotation axis (see figure 2.1), differential rotation within this region cannot be ruled out by present solar observations.

In addition to the two solutions just described, equation (4.7) supports four boundary-layer ($\nabla^2 \approx \partial^2/\partial z^2 \gg 1/L^2$) solutions, which are described by the equation

$$(\Lambda_V + \Lambda_V^{-1}) L^2 \frac{\partial^4}{\partial z^4} T' + \frac{N^2}{2\Omega_i \kappa} T' = 0 . \quad (4.9)$$

As in GM98, solutions that grow exponentially with depth are not physically relevant. This leaves two independent solutions, both of which decay exponentially with depth on the vertical lengthscale

$$\left(\frac{2\Omega_i \kappa}{N^2 L^2} (\Lambda_V + \Lambda_V^{-1}) \right)^{1/4} L . \quad (4.10)$$

Equating this to the lengthscale δ_η , and again assuming that $U \approx 10^{-5} \text{ cm s}^{-1}$, we deduce that $(\Lambda_V + \Lambda_V^{-1}) \approx 240$. This implies that there are two possible values for the vertical field strength $|B_{iz}|$: either $|B_{iz}| \sim 1$ gauss or $|B_{iz}| \sim 10^{-3}$ gauss.

4.2.3 Gyroscopic pumping

GM98 gave a qualitative description of the “gyroscopic pumping” process that drives the downwelling in the high-latitude tachocline. Their argument can be summarised as follows:

1. The turbulent stresses within the convection zone³ impart a systematic retrograde forcing at high latitudes, causing that region to rotate slower than the rest of the convection zone.
2. The confined interior magnetic field \mathbf{B}_i holds the radiative envelope in uniform rotation, and thus constrains the high-latitude tachocline to rotate faster than the layers above.
3. The retrograde forcing at the base of the high-latitude convection zone, unable to spin down this region, instead gyroscopically drives a poleward flow.

³And also any turbulent stresses within the tachocline — see McIntyre (2007) and appendix G.

4. The converging poleward flow establishes a meridional circulation within the tachocline, which tries to burrow into the radiative envelope in the manner described by Haynes *et al.* (1991) and Spiegel & Zahn (1992). The resulting MMC is downwelling in the polar regions (see figure 2.3).

A similar process pumps the “spin-down currents” in Spiegel’s tachycline model (§1.4.2). An analogy can also be made with the “mechanical forcing” described by Miesch *et al.* (2006), but the gyroscopic pumping described by GM98 persists long after the system has established thermal-wind balance. Some more recent studies of gyroscopically pumped meridional circulations are discussed in §4.2.6.

The gyroscopic pumping described by GM98 relies on the interior magnetic field being confined below the base of the convection zone. If, instead, the field lines protrude into the convection zone in high latitudes, then the retrograde forcing in that region will be transmitted directly into the radiative envelope along the unconfined field lines, as in the model of Brun & Zahn (2006).

4.2.4 Global field confinement

GM98 modelled only linear perturbations to the interior magnetic field \mathbf{B}_i , and therefore did not explicitly demonstrate field confinement. Subsequent studies by Garaud (2002) and Garaud & Garaud (2008) have sought to achieve field confinement by MMCs in a global, nonlinear, axisymmetric model of the radiative interior. Garaud & Garaud (2008) also offered a two-fold explanation for the lack of field-confinement in the model of Brun & Zahn (2006). Firstly, by imposing a no-penetration boundary condition at the top of the radiative envelope, Brun & Zahn inhibited the generation of MMCs in their model. Secondly, the viscosity used by Brun & Zahn was too large in relation to the thermal diffusivity, significantly weakening the burrowing tendency of the MMCs. In a field-free analogue of the Brun & Zahn model, radiative spreading would be halted by viscosity before the MMCs could burrow more than $\sim 0.2R_\odot$ into the radiative envelope. As a result, the MMCs in Brun & Zahn’s model were too weak to significantly offset the outward diffusion of the magnetic field.

In Garaud & Garaud’s model, differential rotation *and* meridional flows are im-

posed at the top of the radiative envelope. They found, as expected, that the MMCs in the radiative envelope distorted the magnetic field lines on lengthscales comparable to the magnetic advection–diffusion lengthscale η/U , where U is a typical value of the imposed downwelling at the top of the radiative envelope. In particular, imposing downwelling in high latitudes was found to reduce the magnetic coupling between the interior field \mathbf{B}_i and the differentially rotating outer boundary. However, since they only considered cases where the downwelling vanished at the poles, the magnetic field in all cases was found to be unconfined in the polar regions (see figure 4.3).

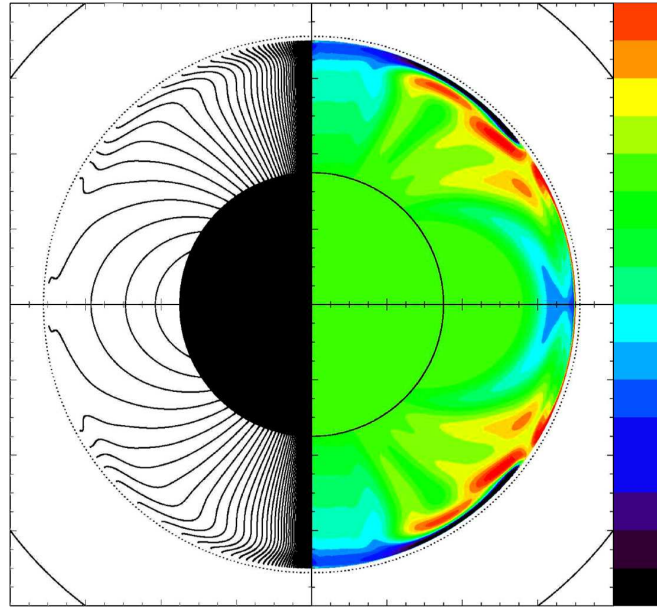


Figure 4.3: Left panel: An interior dipole field \mathbf{B}_i partially confined by MMCs. Right panel: The steady-state angular velocity; the colour axis runs from 278 nHz (black) to 463 nHz (red). Taken from [Garaud & Garaud \(2008\)](#).

The model of [Garaud & Garaud \(2008\)](#) employs a Newton-Raphson-Kantorovich (NRK) numerical algorithm to find solutions of the steady-state equations, rather than evolving the time-dependent equations. With this method, convergence to the steady state is usually more rapid than with a time-dependent algorithm. However, this method provides no information regarding the dynamical convergence to the steady state, and failure to find a steady state does not imply that no steady state exists. Furthermore, any steady state found will be highly sensitive to the choice of boundary conditions, and may also depend on the ansatz used

as a starting point for the algorithm. The discussion of gyroscopic pumping in §4.2.3 suggests that two distinct steady states may exist in high latitudes: one with a magnetic field confined by MMCs, and one with an unconfined field that short-circuits the gyroscopic pumping of MMCs.

4.2.5 Burrowing

Recently, a number of authors have claimed that the tachocline’s MMCs are unable to burrow significantly into the radiative envelope, even in the absence of a magnetic field (e.g. Gilman & Miesch, 2004; Rüdiger *et al.*, 2005), and that the tachocline can therefore be explained simply as an Ekman layer.⁴ Were these claims true, it would undermine the majority of the work that has been reviewed in the preceding chapters. In particular, it would invalidate the model of Spiegel & Zahn (1992), which is the starting point for most models of the tachocline. Detailed criticisms of these claims have been made elsewhere (e.g. McIntyre, 2007; Garaud & Brummell, 2008) and will not be repeated here. Instead, two recent studies of the gyroscopic pumping of MMCs by Garaud & Brummell (2008) and Garaud & Acevedo Arreguin (2009) are summarised in §4.2.6.

However, based on the assumption that MMCs driven in the convection zone and tachocline cannot penetrate deeper into the radiative envelope than the Ekman length $\delta_{\text{Ek}} = (\nu/2\Omega_i)^{1/2}$, Kitchatinov & Rüdiger (2006) have constructed a model for the interaction between the tachocline’s MMCs and the fossil field \mathbf{B}_i in the radiative envelope. Using the tachocline’s microscopic viscosity value $\nu \approx 30\text{cm}^2\text{s}^{-1}$ (see appendix A), the Ekman scale is $\delta_{\text{Ek}} \approx 3 \times 10^3 \text{ cm} \sim 10^{-8} R_\odot$. It might be thought that such a small-scale flow would have negligible impact on the diffusion of the interior field. In particular, since the microscopic magnetic diffusivity η in the tachocline is larger than the viscosity ν by a factor $\eta/\nu \approx 15$, the magnetic field diffuses across a layer of thickness δ_{Ek} in much less than one solar rotation period. However, if the horizontal shear flow within the Ekman layer is sufficiently large, then it can “kink” the field lines that cross it. Indeed, if the Ekman layer is assumed to be infinitely thin, so that its latitudinal flow has the form of a delta function in radius, then the flow will produce a vertical

⁴Or Ekman–Hartmann layer if a magnetic field is present.

discontinuity in the latitudinal magnetic field. This is the situation considered by [Kitchatinov & Rüdiger](#). In their model, the turbulence in the convection zone is assumed to act in the manner of a large magnetic diffusivity, so that the field outside the radiative envelope can be approximated as a vacuum field, for which the latitudinal and vertical components are necessarily of similar magnitude. By imposing an equatorward flow $\sim 10^3 \text{ cm s}^{-1}$ in a layer of thickness $\sim \delta_{\text{Ek}}$ at the top of the radiative envelope, they found that the magnetic field lines crossing the layer were sufficiently kinked that the field lines near the top of the radiative envelope were nearly horizontal. In this way, the interior field could be confined to the radiative envelope.

The shear associated with [Kitchatinov & Rüdiger](#)'s equatorward flow is $\sim 1 \text{ s}^{-1}$, which implies a gradient Richardson number less than 10^{-5} . It is unlikely that such an extreme shear flow would remain stable within the radiative envelope. However, the model relies on the shear layer remaining laminar, or at most weakly turbulent, so that only microscopic magnetic diffusion is present within this layer. A larger magnetic diffusivity would not permit the required kinking of the magnetic field lines. Yet the magnetic diffusivity is assumed to be infinite in the convection zone immediately above the shear layer, in order to prevent large horizontal magnetic fields from accumulating in that region.

It should also be noted that the latitudinal flow assumed by [Kitchatinov & Rüdiger](#) is artificially imposed (via mass sources at the pole and corresponding sinks at the equator) and is not derived within the model. Furthermore, the Coriolis force arising from this flow is neglected, although it would be expected to make a leading-order contribution to the total force balance. The Lorentz forces arising from the kinking of the field lines in the Ekman layer are also not included in the model.

4.2.6 Recent studies of gyroscopic pumping

The radiative spreading, or burrowing, described by [Spiegel & Zahn \(1992, see §2.4\)](#) arises because of the departures from geostrophic balance implied by the tachocline's rotational shear. Such departures imply, via thermal-wind balance, a horizontal temperature gradient, which must be maintained against thermal

relaxation by the advection of entropy by meridional circulations. In the absence of viscous or magnetic torques, the Coriolis torque on the meridional circulation cannot be balanced, and as a result the meridional circulations burrow into the interior, spreading the differential rotation of the convection zone. Radiative spreading is essentially a hyperdiffusive process, and so the tachocline in [Spiegel & Zahn](#)'s model thickens as $t^{1/4}$. More precisely, if the rotation rate in the tachocline varies on a horizontal scale of order L , say, then the tachocline thickness Δ grows like

$$\Delta \sim L(t/\tau)^{1/4} \quad (4.11)$$

where

$$\tau = \left(\frac{N}{2\Omega_i} \right)^2 \frac{L^2}{\kappa}, \quad (4.12)$$

cf. equation (1.5). Here, Ω_i is the uniform rotation rate below the tachocline.

As radiative spreading brings the radiative interior progressively closer to a geostrophically balanced Taylor–Proudman state, so the meridional flow speed decreases. Eventually the flow would shut off completely, but only after a time $\gg \tau$, which is much longer than the age of the Sun.

In the presence of some additional physics, such as viscosity or magnetic fields, that is capable of supporting a finite torque, the burrowing process can be halted sooner, and finite meridional circulations can persist even in the steady state. In the absence of radiative spreading, the presence of viscosity, ν , would itself cause the tachocline thickness to grow like

$$\Delta \sim (\nu t)^{1/2}. \quad (4.13)$$

Equating (4.11) and (4.13) we deduce that viscous diffusion overtakes radiative spreading, thereby shutting off the burrowing of the meridional circulations, when

$$\Delta \sim \frac{L^2}{(\nu\tau)^{1/2}} \quad (4.14)$$

$$\sim \left(\frac{\kappa}{\nu} \right)^{1/2} \left(\frac{2\Omega}{N} \right) L \quad (4.15)$$

(see [Clark, 1973](#)). In oceanography, the lengthscale (4.15) is usually called the

Lineykin length,⁵ after [Lineykin \(1955\)](#).

In a recent study, [Garaud & Brummell \(2008, hereafter GB08\)](#) have analysed the steady-state structure of meridional flows in the radiative interior in the presence of viscosity. Their model is similar to that of [Spiegel & Zahn](#) in that the flows, which are assumed to be linear perturbations to a hydrostatic, stably stratified background, are driven by boundary conditions imposed at the interface between the radiative and convective zones. The particular sets of boundary conditions they consider differ from those of [Spiegel & Zahn](#), however. Specifically, they impose the three components of velocity at the top of the radiative envelope, together with one of two choices for the thermal boundary conditions. The first choice imposes that the temperature perturbation has no derivative normal to the radiative–convective interface,⁶ and the second choice imposes that the perturbations do not contribute to the total (advective plus diffusive) flux of heat across the radiative–convective interface.

[GB08](#) first consider a cartesian model, with the rotation axis aligned with gravity, and with constant buoyancy frequency N and constant angular velocity Ω_i . In this situation, the importance of stratification in shaping the steady state is quantified by the dimensionless parameter σ , say, where

$$\sigma = \left(\frac{\nu}{\kappa}\right)^{1/2} \frac{N}{2\Omega_i} \quad (4.16)$$

(e.g. [Barcilon & Pedlosky, 1967](#)). Assuming that all fields have the same sinusoidal horizontal dependence, [GB08](#) show that any steady-state solution can be expressed as a superposition of eight linearly independent modes. In the parameter regime appropriate to the solar interior, four of these modes have the small vertical lengthscale characteristic of Ekman layers, $\delta_{\text{Ek}} = (\nu/2\Omega_i)^{1/2}$. Of the remaining four modes, two have vertical scales equal to the imposed horizontal scale, L say, and two (the Lineykin modes) have the vertical scale given by (4.15), i.e. $\sigma^{-1}L$. With parameter values appropriate to the tachocline (see appendix A), we have $\sigma^{-1} \approx 5$. The Lineykin modes therefore penetrate considerably deeper

⁵[Garaud & Acevedo Arreguin \(2009\)](#) refer to this as the “thermo-viscous” lengthscale. We will not use this term here, in order to avoid confusion with the thermo-viscous lengthscale found by [Tassoul & Tassoul \(1986\)](#) in a very similar problem.

⁶Although [GB08](#) refer to this as a “perfectly conducting” boundary condition, in fact it serves to fix the diffusive heat flux across the boundary.

than the Ekman modes for any L that is larger than δ_{Ek} .

If the domain is assumed to be infinitely deep then, for all the sets of boundary conditions GB08 considered, virtually all of the meridional flow in the steady state resides within an Ekman layer below the radiative–convective interface. They found that the deep meridional flows were strongest in cases where vertical flows were imposed at the interface, and when the second choice of temperature boundary conditions was employed. Even in these cases, the vertical flows beneath the Ekman layer were found to be weaker than the vertical flows imposed at the interface by a factor

$$\frac{\sigma H}{L} \approx \frac{H}{5L} \quad (4.17)$$

where L is again the imposed horizontal scale and $H = g/N^2$ is the scale height of the background potential temperature. Furthermore, mass conservation implies that the latitudinal flow within the thin Ekman layer is much faster than the vertical flow, by a factor L/δ_{Ek} , whereas the latitudinal flow within the deep interior is slightly slower than the vertical flow, by a factor $\sigma \approx 0.2$.

If we take the limit $\nu \rightarrow 0$, holding all other quantities fixed, then $\sigma \rightarrow 0$. In this limit *all* of the downwelling meridional flow imposed at the radiative–convective interface is diverted into an Ekman layer of vanishing thickness, and the flow within the bulk of interior vanishes. This is at first surprising, as it seems to suggest that the presence of viscosity is essential for driving deep meridional flows, contrary to the results of Spiegel & Zahn (1992). This apparent paradox is resolved when we remember that the analysis of GB08 applies only to the steady state, in which the burrowing of meridional circulations has either extended to infinite depth and then shut off, or else has been halted by viscosity.

If the domain is now assumed to be of finite depth, and if the lower boundary is taken to be impenetrable, then there is a limit on the depth to which meridional circulations can burrow, and so we would expect stronger circulations in the steady state. GB08 verify that this is indeed the case. In particular, if the depth of the domain is taken to be the same as the imposed horizontal scale, L , then the vertical component of the deep meridional circulation increases by a factor of $\sigma^{-1} \approx 5$, and the latitudinal component increases by a factor of $\sigma^{-2} \approx 25$.

GB08 then consider a more realistic model of the radiative interior, in axisymmet-

ric spherical geometry, with background thermodynamic profiles from a standard one-dimensional solar model. The linearised equations are solved using the same NRK algorithm used by [Garaud & Garaud \(2008, see §4.2.4\)](#). They find that the scaling laws derived from the cartesian model agree very well with the results of the more realistic model. The agreement is particularly good in cases where the deep meridional circulations are weak. Physically, this is because only the deep circulations are affected by the geometrical curvature and the non-uniform background profiles used in the spherical model.

The results of [GB08](#) demonstrate that imposing strong flows at the radiative–convective interface does not guarantee the existence of strong steady-state meridional circulations within the radiative interior. Indeed, in the absence of viscosity ν , any meridional circulation would have an unbalanced Coriolis torque, and so the steady-state meridional circulation must vanish in the limit $\nu \rightarrow 0$. The choice of temperature boundary conditions is also found to significantly affect the steady state.

However, [GB08](#) note that by considering only the linearised steady-state equations they have overlooked many possible types of behaviour that might otherwise arise. For example, sufficiently strong meridional circulations within the stably stratified interior can overturn the stratification surfaces. This kind of nonlinear behaviour is beyond the scope of the linearised equations, and might be missed completely by a steady-state analysis. (For further discussion, see [McIntyre \(2007\)](#).) Similarly, angular momentum transport by meridional circulations can lead to nonlinear departures from an initial state of uniform rotation. Indeed, in several of the cases presented by [GB08](#) the steady state has regions of counterrotation! Clearly such solutions should not be taken literally.

In a subsequent study, [Garaud & Acevedo Arreguin \(2009, hereafter GAA09\)](#) have considered meridional flows driven by Reynolds stresses within the convection zone, rather than by conditions imposed at the radiative–convective interface. They model the convection zone as an unstratified layer, with a large (turbulent) thermal diffusivity, overlying the stably stratified radiative interior. Within the convection zone they parametrise the turbulent Reynolds stresses in terms of a “generalised Rayleigh friction” that drives the system towards a state with prescribed differential rotation and vanishing meridional flow within the con-

vection zone (cf. appendix B, in which we assume a purely azimuthal friction). This friction can be regarded as a generalisation of the Darcy friction used by [Bretherton & Spiegel \(1968\)](#) to model Reynolds stresses in the convection zone. In the model of [GAA09](#), the azimuthal component of the friction gyroscopically pumps meridional circulations in the convection zone, which penetrate into the interior; in this respect their model has more in common with those of [Haynes *et al.* \(1991\)](#) and [McIntyre \(2007\)](#) than with that of [Spiegel & Zahn \(1992\)](#).

As in [GB08](#), they first consider a cartesian model, and then a more realistic spherical model. However, due to the complexity of modelling the interface between the convection zone and the radiative interior, even the cartesian model can only be solved analytically in certain limiting cases. The cartesian model is further simplified by assuming that the differential rotation towards which the convection zone is driven is linear in altitude and sinusoidal in latitude.

With realistically small values for the diffusivities, [GAA09](#) find that meridional circulations within the convection zone are typically stronger than any meridional circulations within the deep radiative interior by many orders of magnitude. In “weakly stratified” cases, defined by $\sigma \ll 1$, the strength of the deep meridional circulations is found to depend on the choice of boundary conditions at the bottom of the cartesian domain. In particular, cases with a no-slip lower boundary condition typically have significantly stronger circulations than cases with a stress-free lower boundary condition. This behaviour is most evident in cases with no stratification, i.e. $\sigma = 0$ (see figure 4.4). But even in these cases, the circulations within the radiative interior are still much weaker than those within the convection zone (again, see figure 4.4).

At first sight, it is perhaps surprising that the interior meridional circulations are so weak even in the absence of stratification. However, it should be remembered that such circulations arise because of departures from geostrophic balance (i.e. departures from a Taylor–Proudman state). In figure 4.4 it is evident that the steady state below the convection zone is very nearly a Taylor–Proudman state, and therefore it should be no surprise that the steady-state meridional circulations are weak in that region. It is also evident that the presence of a no-slip lower boundary breaks the Taylor–Proudman constraint, and therefore allows for stronger steady-state meridional circulations. [GAA09](#) note that “the dynamics

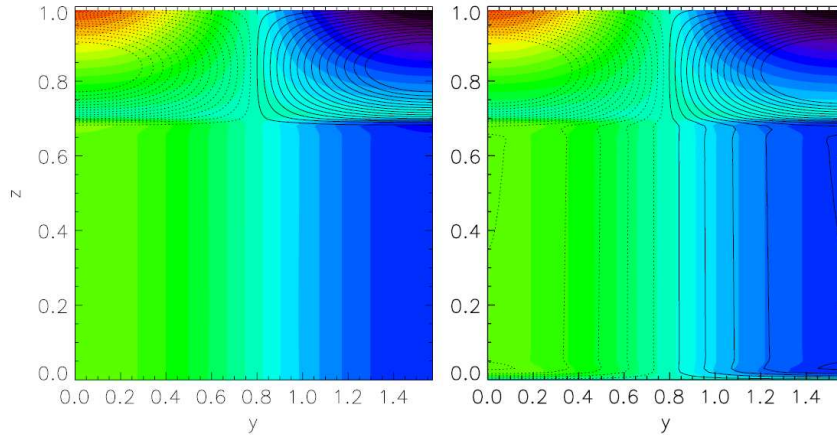


Figure 4.4: Steady-state meridional circulations and differential rotation in an unstratified, cartesian model of the solar interior (Garaud & Acevedo Arreguin, 2009). Colours represent angular velocity, and solid/dotted lines represent anti-clockwise/clockwise meridional streamlines. The left and right panels show the cases with stress-free and no-slip lower boundaries respectively. The convection zone is located in the region $0.7 \leq z \leq 1.0$.

of the lower boundary layer entirely control the mass flux through the system”.⁷

In “strongly stratified” cases, i.e. cases with $\sigma \gg 1$, the deep meridional circulations are confined to a thin Lineykin boundary layer below the convection zone, with an aspect ratio $\sim \sigma$. Nonetheless, the steady-state rotation profile is still found to be roughly constant on cylinders, as a result of viscous diffusion over the entire domain. Since the meridional flows do not extend to the bottom of the domain, the choice of lower boundary conditions has little influence on the structure of the steady state in these cases.

GAA09 note that the parameter σ depends not only on the stratification strength N but also on the rotation rate Ω_i . So at the time of the Sun’s arrival on the main sequence, when the Sun rotated more rapidly, the burrowing tendency would have been stronger. We expect this statement to apply to the transient meridional flows as well as to the steady-state meridional flows (§2.4).

Finally, GAA09 note that viscosity is not the only mechanism capable of overcoming the Taylor–Proudman constraint and sustaining a finite torque. An in-

⁷This statement on first reading seems to directly contradict the principle of “downward control” described by Haynes *et al.* (1991, see §1.2). However, downward control operates only in non-Boussinesq systems, i.e. systems with meridional circulations encompassing several density scale heights.

terior magnetic field can also serve these two purposes, and thereby prevent the burrowing of meridional circulations while also permitting finite meridional circulations to persist in the steady state, as described by [Gough & McIntyre \(1998\)](#). However, a complete model of these processes would also need to describe the confinement of the magnetic field, and so there is no direct analogy between the models of [Gough & McIntyre](#) and [GAA09](#).

4.3 Summary

The observations made in the preceding sections highlight the need for a fully self-consistent model of magnetic confinement and angular momentum balance within the tachocline. From the various studies of the solar interior reviewed in chapters 2–4 we may draw the following conclusions:

- In order to confine the convection zone’s differential rotation, and maintain uniform rotation within the radiative envelope, angular momentum must be transported from the low-latitude tachocline to the high-latitude tachocline.
- An interior magnetic field \mathbf{B}_i can naturally produce this angular momentum transport, provided that the field is confined, i.e. provided that the field lines remain nearly horizontal within the tachocline.
- If the interior magnetic field is assumed to be an axisymmetric dipole, then magnetic flux pumping by overshooting convection may be able to confine the field in middle and low latitudes.
- Field confinement in high latitudes can probably only be achieved by the tachocline’s MMCs, which, fortunately, are expected to be downwelling at those latitudes.

In Part [III](#) we construct a model of the magnetic confinement layer responsible for confining the interior magnetic field in high latitudes. First, in Part [II](#), we discuss certain observations regarding the Sun’s composition, and the physical implications of these observations. These discussions prove to have a significant bearing on our confinement-layer model.

Part II

Solar Composition

Chapter 5

Helium Settling

5.1 The μ -choke

The molecular cloud from which the Sun formed comprised mostly hydrogen and helium, plus traces of heavier elements¹ (collectively known as “metals”). When the Sun first formed, its composition by mass was roughly 72% hydrogen, 27% helium and 1% metal (e.g. [Asplund *et al.*, 2009](#)).

During its pre-main-sequence Hayashi phase, the entire Sun was in a state of turbulent convection. The turbulence maintained an approximately uniform composition throughout the interior. At the end of the Hayashi phase the centre of the Sun became convectively stable, and the base of the convection zone began to retreat towards its current location (e.g. [Iben, 1965](#)). The retreat of the convection zone took approximately 3×10^7 years, and concluded at about the same time as the Sun arrived on the main sequence. This timescale is sufficiently short that the Sun was still “well mixed”, i.e. compositionally homogeneous, at the start of the main sequence, with a uniform helium mass fraction $Y \approx 0.27$.

In the absence of interactions between the various chemical species inside the Sun (including free electrons) each species would attain separate hydrostatic equilibrium on a dynamical timescale, with the hydrogen nuclei located further from the gravitational centre of the Sun, on average, than the helium nuclei, for example.

¹Including lithium and beryllium, which are discussed in the next chapter.

But collisions between the various species reduce the rate at which this compositional segregation occurs, and under certain conditions can even reverse the direction of the compositional flux. The slow segregation that occurs in the presence of collisions is usually called either “gravitational settling” or “diffusion”, and has a timescale much longer than the lifetime of the Sun (see §5.3 below). The compositional changes produced by gravitational settling may therefore be regarded as linear perturbations from the perspective of stellar evolution.

The terms “settling” and “diffusion” are used interchangeably in the literature. In this dissertation, we will use “settling” to refer to a compositional flux that is proportional to the concentration, and “diffusion” to refer to a compositional flux that is proportional to the concentration gradient, although this distinction is somewhat artificial.

Within the Sun’s core, the helium mass fraction Y increases steadily during the main sequence as a result of hydrogen fusion (see figure 5.1). Within the convection zone the composition remains roughly uniform throughout the main-sequence phase, because of turbulent mixing, but as heavy elements settle out of the convection zone a vertical compositional gradient develops in the outer part of the radiative envelope. The resulting gradient in the mean molecular weight μ contributes significantly, in today’s Sun, to the total stable stratification within that region. Since the formation of this layer is principally due to gravitational settling of helium, it is usually known as the “helium settling layer”. The reality of the helium settling layer is strongly indicated by both standard solar-evolution models and helioseismology, notwithstanding the compositional uncertainties described in §2.2 (e.g. Christensen-Dalsgaard *et al.*, 1993; Ciacio *et al.*, 1997; Elliott & Gough, 1999; Christensen-Dalsgaard & Thompson, 2007, again see figure 5.1).

Because the rate of diffusion of heavy elements through hydrogen is typically very small compared to thermal diffusion, compositional stratification is much more effective at inhibiting vertical motions than thermal stratification (recall §1.2). This near-impermeability of compositionally stratified regions strongly inhibits MMCs, and has been called the “ μ -choke” (Mestel & Moss, 1986).

The effects of compositional stratification were neglected in the tachocline model

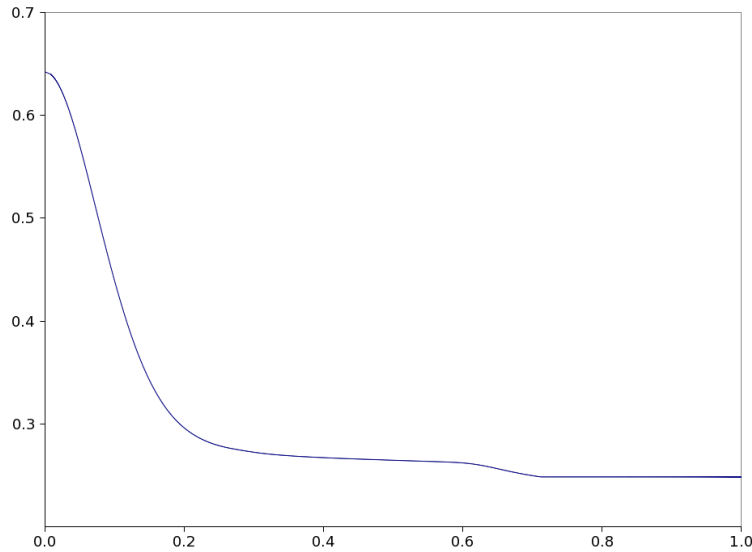


Figure 5.1: The helium mass fraction Y in a one-dimensional model of the solar interior, plotted as a function of radius R in units of R_\odot (J. Christensen-Dalsgaard, personal communication). Nuclear fusion produces helium in the region $R \lesssim 0.2R_\odot$. The helium settling layer is visible below the convection zone in the region $0.6R_\odot \lesssim R \lesssim 0.7R_\odot$.

of GM98. Subsequently, McIntyre (2007) presented a significantly revised version of the GM98 model that included the effects of compositional stratification. In the revised model, the helium settling layer acts as a barrier against the MMCs responsible for confining the interior field.² Furthermore, the stable compositional stratification within the helium settling layer holds the μ isopleths horizontal to within “a very tiny fraction of a megametre”. Therefore the tachocline’s MMCs are unable to dig the polar pits conjectured in §4.2.2. Moreover, the MMCs do not decay exponentially with depth beneath the magnetic confinement layer in the manner described in §4.2.1, but terminate abruptly at a “tachopause” marking the top of the helium settling layer.

These conclusions, which have significant implications for lithium burning (chapter 6), rely on the existence of the helium settling layer and the compositional stratification therein. Our aim in this chapter is to delineate the physical processes involved in the formation of the helium settling layer, and to estimate its contribution to the total buoyancy frequency. In this way, we can test the robust-

²Spiegel & Zahn (1992) also considered the effect of compositional stratification, as a possible means to halt radiative spreading in their model of the tachocline. They concluded that radiative spreading is not hindered by the presence of compositional stratification. This conclusion is in error, as explained in §8.5 of McIntyre (2007).

ness of the arguments made in [McIntyre \(2007\)](#) against the assumptions made by solar evolution models.

5.2 The settling equation

We consider a simple one-dimensional model of solar evolution. For simplicity, we suppose that the Sun contains only hydrogen and helium, i.e. we neglect heavier elements. The settling and diffusion of helium within the radiative envelope, viewed in an inertial frame, can be described by the equation

$$\frac{\partial}{\partial t}(\rho R^2 Y) = -\frac{\partial}{\partial R} \left(\rho R^2 (u_R - v) Y - \rho R^2 \chi \frac{\partial Y}{\partial R} \right) \quad (5.1)$$

(e.g. [Proffitt & Michaud, 1991](#)). Here, $\rho(R, t)$ is the density, $u_R(R, t)$ is the radial velocity, $\chi(R, t)$ is the diffusivity of helium through hydrogen and $v(R, t)$ is the “settling velocity”. Both χ and v are calculated from inter-species collision integrals, and are related by the formula

$$v = \chi \left(\frac{k_p}{H_p} + \frac{k_T}{H_T} \right) \quad (5.2)$$

where H_p and H_T are the pressure and temperature scale heights, and k_p and k_T are the corresponding Soret factors, which depend only on the local composition. The scale heights and Soret factors can be calculated to a high degree of accuracy, but the formulae for χ and v depend on the Coulomb logarithm, and consequently are less tightly constrained (e.g. [Michaud & Proffitt, 1993](#)). Therefore we will make only order-of-magnitude statements in what follows. Approximate values for all these quantities at $0.7R_\odot$ are given in appendix A. We note that v is always positive, and so the settling flux is always directed downward, as we would expect, whereas the diffusive flux may be directed either up or down.

Within the nuclear core, a source term must be introduced into equation (5.1) to represent the production of helium by nuclear fusion. The changes in the core’s composition drive the main-sequence evolution of the Sun. However, the compositional changes within the outer radiation zone are small, as can be seen in figure 5.1, and play no role in the Sun’s main-sequence evolution to a first ap-

proximation. In describing the formation of the helium settling layer, the density ρ , the pressure p and the temperature T may therefore be assumed independent of Y in (5.1), and regarded as known functions of R and t . This assumption also allows us to approximate the Soret factors in (5.2) as constant, rather than as functions of Y . Similarly we may neglect the Y -dependence of χ and v , so that the settling and diffusion coefficients are also known functions of R and t . In particular, since the Coulomb logarithm is approximately constant throughout the solar interior, we have

$$\chi \propto \frac{T^{5/2}}{\rho} \quad (5.3)$$

(Michaud & Proffitt, 1993). Under these assumptions (5.1) becomes a linear PDE for the helium mass fraction Y within the radiative envelope.

Equation (5.1) assumes purely radial motions, and therefore neglects any compositional mixing arising from turbulence or MMCs. In stellar evolution modelling, these mixing processes are usually parametrised in terms of a turbulent diffusivity (see discussion in §5.5). In this study, for simplicity, we will assume that turbulent mixing is confined to the convection zone, where it maintains a perfectly homogeneous composition throughout the Sun's main-sequence life. This treatment of convective mixing is equivalent to assuming an infinitely large turbulent diffusivity within the convection zone.

The location of the convection zone does not remain fixed in space during the main sequence, because the Sun's outer layers expand over time. However, the convection zone's lower boundary is approximately fixed in the Lagrangian description. It is therefore convenient to rewrite equation (5.1) in terms of new coordinates M and t , where $M(R, t)$ represents the mass contained within a sphere of radius R at time t . Then

$$\left(\frac{\partial M}{\partial R} \right)_t = 4\pi\rho R^2 \quad (5.4)$$

$$\text{and} \quad \left(\frac{\partial M}{\partial t} \right)_R = -4\pi\rho R^2 u_R. \quad (5.5)$$

It follows that the “mass coordinate” M is a Lagrangian coordinate, since

$$\left(\frac{\partial R}{\partial t}\right)_M = - \left(\frac{\partial M}{\partial t}\right)_R / \left(\frac{\partial M}{\partial R}\right)_t \quad (5.6)$$

$$= u_R . \quad (5.7)$$

Written in terms of the new coordinates M and t , equation (5.1) becomes

$$\frac{\partial Y}{\partial t} = \frac{\partial}{\partial M} \left(4\pi\rho R^2 v Y + (4\pi\rho R^2)^2 \chi \frac{\partial Y}{\partial M} \right) . \quad (5.8)$$

So, in the Lagrangian description, the mass fraction Y is a conserved quantity. Integrating equation (5.8) between fixed mass coordinates, say $M = M_1$ and $M = M_2$, we obtain

$$\frac{d}{dt} \int_{M_1}^{M_2} Y dM = \left[4\pi\rho R^2 v Y + (4\pi\rho R^2)^2 \chi \frac{\partial Y}{\partial M} \right]_{M_1}^{M_2} \quad (5.9)$$

which quantifies how the total mass of helium between concentric material surfaces changes due to settling and diffusive fluxes over those surfaces.

Though the evolution equation (5.8) does not hold within the convection zone, the principle of helium conservation can still be applied there. Neglecting any loss of helium due to outflows from the solar surface we may therefore express the conservation of helium in the convection zone as

$$\frac{d}{dt} \int_{M_{\text{RZ}}}^{M_\odot} Y dM = - \left(4\pi\rho R^2 v Y + (4\pi\rho R^2)^2 \chi \frac{\partial Y}{\partial M} \right) \Big|_{M=M_{\text{RZ}}} \quad (5.10)$$

where $M_{\text{RZ}} \approx 0.975M_\odot$ is the mass coordinate at the top of the radiation zone, and M_\odot is the total solar mass, both of which we approximate as constant. The right-hand side of equation (5.10) is to be evaluated immediately *below* the base of the convection zone, where χ takes a microscopic (non-turbulent) value. Our assumption that turbulent mixing homogenises the chemical composition within the convection zone implies that Y can be taken outside the integral on the left-hand side of (5.10). We thus obtain an equation for the evolution of Y within

the convection zone:

$$M_{\text{CZ}} \frac{dY}{dt} = - \left(4\pi\rho R^2 v Y + (4\pi\rho R^2)^2 \chi \frac{\partial Y}{\partial M} \right) \Big|_{M=M_{\text{RZ}}} \quad (5.11)$$

where $M_{\text{CZ}} = M_{\odot} - M_{\text{RZ}}$ is the mass of the convection zone. This equation serves as an outer boundary condition when solving (5.8) within the radiative envelope.

5.3 The formation of the helium settling layer

Since the Sun's chemical composition is assumed to be uniform at the start of the main sequence, there is no diffusive flux anywhere in the interior at that time. Therefore the initial evolution within the bulk of the radiative envelope (i.e. away from the core and convection zone) arises entirely from spatial variations in the settling rate:

$$\frac{\partial Y}{\partial t} = Y \frac{\partial}{\partial M} (4\pi\rho R^2 v) \quad (5.12)$$

$$\sim -Y \frac{v}{H_{\rho}}, \quad (5.13)$$

where H_{ρ} is the density scale height. This process has a timescale of order $H_{\rho}/v \sim 60\text{Gyr}$ — considerably longer than the Sun's main sequence lifetime — and produces a slight compositional gradient within the bulk of the radiation zone (see figure 5.1, between $0.4R_{\odot}$ and $0.6R_{\odot}$). The formation of the settling layer is a separate process that is driven by the boundary condition (5.11). For the rest of this section we will neglect the effects of spatial or temporal variations in ρR^2 , v and χ on the formation of the settling layer. The importance of such effects will be considered in §5.3.3.

Formation of the settling layer, at least in the early stages of the main sequence, is driven by helium settling out of the convection zone. From (5.11) we see that the helium mass fraction Y at the top of the radiative envelope initially decreases exponentially on the timescale t_{CZ} given by

$$t_{\text{CZ}} = \frac{M_{\text{CZ}}}{v} \frac{\partial R}{\partial M} \Big|_{M_{\text{RZ}}} \quad (5.14)$$

which is of the order of 30Gyr. This depletion of helium from the convection zone produces a steep gradient in Y at the top of the radiative envelope. Diffusion of helium back into the convection zone reduces this gradient, producing a diffusive tail in Y in the outer part of the radiative envelope whose thickness increases as $(\chi t)^{1/2}$. This diffusive tail is the nascent helium settling layer. During these early stages, the compositional gradient in the settling layer is roughly $\partial \ln Y / \partial r \sim -(t/t_{\text{CZ}})/(\chi t)^{1/2} \propto -t^{1/2}$. The subsequent evolution of the settling layer depends crucially on the relative magnitudes of t_{CZ} and the settling–diffusion time, $t_{\text{SD}} = \chi/v^2$.

5.3.1 The solar case

In the outer part of the Sun’s radiative envelope, the settling–diffusion time t_{SD} is approximately 7Gyr, which is significantly shorter than the timescale for helium depletion in the convection zone, $t_{\text{CZ}} \approx 30\text{Gyr}$. As the helium settling layer steepens, the upward diffusive flux of helium into the convection zone increases, while the downward settling flux remains roughly constant. After a time of order t_{SD} , the upward diffusive flux is still smaller than the downward settling flux, by a factor $(\chi/v)\partial \ln Y / \partial R \sim (\chi/v)(t_{\text{SD}}/t_{\text{CZ}})/(\chi t_{\text{SD}})^{1/2} \sim (t_{\text{SD}}/t_{\text{CZ}})$. To a first approximation we may therefore neglect the diffusive flux of helium into the convection zone throughout this period. The upper boundary condition (5.11) can therefore be approximated as

$$\frac{dY}{dt} = -\frac{Y}{t_{\text{CZ}}} \quad \text{at } M = M_{\text{RZ}}. \quad (5.15)$$

For times $t \lesssim t_{\text{SD}}$, the helium settling layer thickens like $(\chi t)^{1/2}$. When $t \sim t_{\text{SD}}$ the thickness of the settling layer becomes comparable to the settling–diffusion length, $\chi/v \approx 0.02R_{\odot}$. At this time the divergence of the settling flux in (5.8) becomes of the same order as the divergence of the diffusive flux. For times $t \gtrsim t_{\text{SD}}$ the depth of the settling layer therefore increases roughly linearly in time, like vt , and the compositional gradient therefore converges to a constant

value,

$$\left. \frac{\partial \ln Y}{\partial R} \right|_{M_{\text{RZ}}} \approx -(t/t_{\text{CZ}})/(vt) = -1/(vt_{\text{CZ}}) \quad (5.16)$$

$$\Leftrightarrow \left. \frac{\partial Y}{\partial M} \right|_{M_{\text{RZ}}} \approx -\frac{Y}{M_{\text{CZ}}} . \quad (5.17)$$

In fact, this implies that the settling flux out of the convection zone exceeds the diffusive flux into the convection zone even for times $> t_{\text{SD}}$. Throughout the evolution the abundance of helium in the convection zone therefore decreases approximately exponentially, but on a long timescale $t_{\text{CZ}} \approx 30\text{Gyr}$, and so helium depletion in the convection zone occurs at a roughly constant rate during the main sequence.

5.3.2 The super-solar case

Stars that are slightly more massive (and therefore hotter and less opaque) than the Sun have smaller convection zones (e.g. [Pinsonneault *et al.*, 2001](#)). For such stars the available “reservoir” of helium in the convection zone is smaller, and the timescale t_{CZ} is therefore shorter. A star of mass $1.1M_{\odot}$, for example, would have $t_{\text{CZ}} \ll t_{\text{SD}}$. In that case the upward diffusive flux of helium into the convection zone quickly comes into balance with the downward settling flux, after a time of roughly $t_{\text{CZ}}^2/t_{\text{SD}} \ll t_{\text{CZ}}$. From this time onwards the upper boundary condition (5.11) can be approximated as

$$0 \approx \left(vY + 4\pi\rho R^2\chi \frac{\partial Y}{\partial M} \right) \Big|_{M=M_{\text{RZ}}} \quad (5.18)$$

and the formation of the helium settling layer proceeds as though the convection zone were infinitely thin. From (5.18) we deduce that

$$\left. \frac{\partial \ln Y}{\partial R} \right|_{M_{\text{RZ}}} \approx -v/\chi . \quad (5.19)$$

5.3.3 The effect of spatio-temporal variations

The formation of the settling layer is affected quantitatively by the variations of ρR^2 , v and χ in both space and time, which have been neglected in the analysis above. The effect of these variations can be estimated by a simple experiment in which we evolve equation (5.8) with *static* profiles of ρR^2 , v and χ . To this end we have written a numerical code to timestep (5.8) using profiles for ρR^2 , v and χ calculated from a one-dimensional model of the solar interior (J. Christensen-Dalsgaard, personal communication). The numerical scheme employed is identical to that described in Proffitt & Michaud (1991), except that the settling flux is calculated using a first-order upwind difference (as opposed to their centred difference). This gives greater numerical stability, with no loss in overall accuracy. In figure 5.2 we plot the resulting evolution of Y , from an initially uniform profile of $Y = 0.27$, over 5Gyr on the main sequence. The formation of the

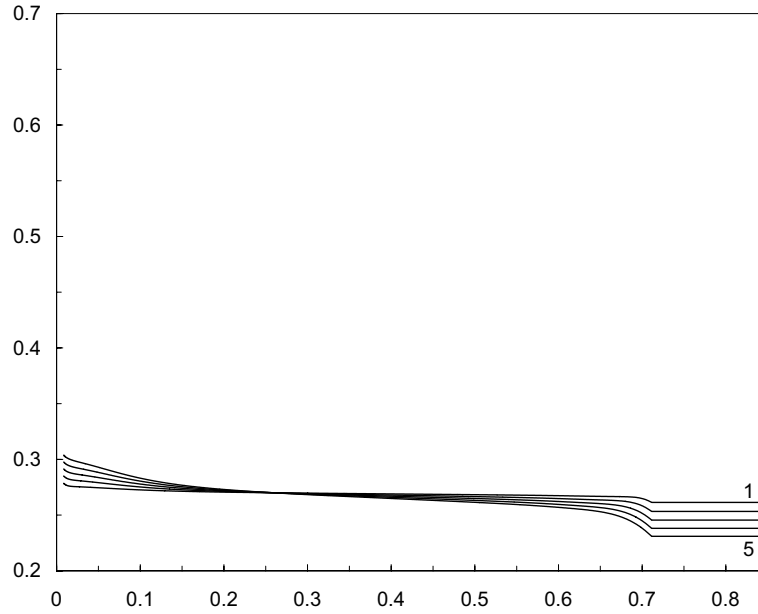


Figure 5.2: Plots of Y against R/R_\odot after 1, 2, 3, 4 and 5Gyr on the main sequence.

helium settling layer closely follows the analytical predictions, suggesting that spatial variations in the profiles of ρR^2 , v and χ do not significantly influence the process. We note in particular that the abundance of helium in the convection zone decreases approximately linearly with time, indicating that the downward settling flux out of the convection zone dominates the upward diffusive flux into

the convection zone throughout the period simulated. The plots in figure 5.2 are also in rough agreement with those of [Ciaccio *et al.* \(1997\)](#), where the full nonlinear, time-dependent equations were employed (see figure 5.3). The most conspicuous difference — aside from the lack of nuclear fusion in our model — is due to the gradual shift in the location of the convection zone mentioned in §5.2. Nonetheless, both models produce comparable estimates for the compositional gradient within the helium settling layer, so the effect of temporal variations in the profiles of ρR^2 , v and χ also has little impact on the formation of this layer.

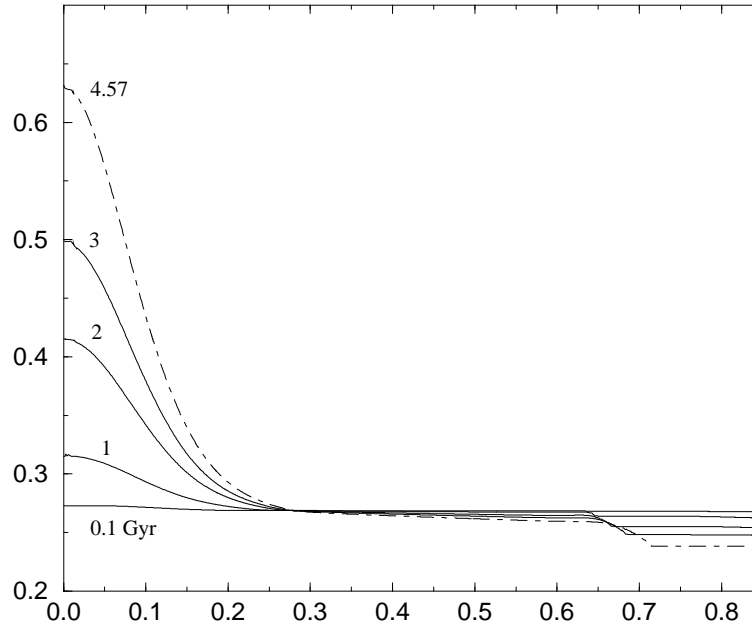


Figure 5.3: Plots of Y against R/R_{\odot} at various stages during main sequence. Taken from [Ciaccio *et al.* \(1997\)](#).

5.4 The compositional gradient

We can use the scaling arguments in §5.3.1 to estimate the contribution from compositional stratification, N_{μ} say, to the buoyancy frequency N at the top of the radiative envelope. In this region both hydrogen and helium are fully ionised, and so the mean molecular weight μ , neglecting contributions from heavier elements, depends only on Y :

$$\mu = \frac{1}{2 - \frac{5}{4}Y} \quad (5.20)$$

(e.g. [Strömberg, 1938](#)). Hence

$$d \ln \mu = \frac{5}{4} \mu dY \quad (5.21)$$

and so, assuming an ideal gas equation of state,

$$N_\mu^2 = -g \frac{\partial \ln \mu}{\partial R} = -\frac{5}{4} g \mu \frac{\partial Y}{\partial R} . \quad (5.22)$$

Using the upper bound for $\partial \ln Y / \partial R$ given by (5.16) we obtain an estimate for N_μ of roughly 10^{-3}s^{-1} . This is in good agreement with the value $N_\mu \approx 0.5 \times 10^{-3} \text{s}^{-1}$ computed by [McIntyre \(2007, §8.5\)](#) from information in [Christensen-Dalsgaard & Thompson \(2007\)](#).

5.5 Summary

The discussions above indicate that the helium settling layer is a robust feature of the solar interior, i.e. that its existence is not conditional on the assumptions or parametrisations made in solar-evolution models. In particular, the presence of additional turbulent mixing below the base of the convection zone cannot prevent the formation of the settling layer. If the turbulent mixing is very efficient, then it can be regarded as an extension of the mixing in the convection zone, and will therefore only cause the settling layer to form deeper inside the radiative envelope. Less efficient turbulent mixing, on the other hand, can make the settling layer thicker, and thereby reduce the compositional gradient below the convection zone. For example, if we suppose that turbulence below the convection zone produces an fifty-fold increase in the effective helium diffusivity χ , then the effective settling–diffusion time t_{SD} also increases by a factor of fifty. This puts the Sun into the regime discussed in §5.3.2 (i.e. $t_{\text{SD}} \gg t_{\text{CZ}}$). The compositional gradient at the top of the radiative envelope is then reduced by a factor $t_{\text{CZ}}/t_{\text{SD}} \approx 0.1$ from the value estimated in §5.4, meaning that N_μ^2 is about ten times smaller. A larger turbulent diffusivity would produce a greater reduction in N_μ , but could not be reconciled with helioseismology ([Christensen-Dalsgaard *et al.*, 1993](#)).

As described by [McIntyre \(2007\)](#), the presence of the helium settling layer has

significant implications for the convection zone's lithium abundance. These are discussed in detail in the next chapter.

We note that the helium settling layer, though an effective barrier against MMCs, does not nullify the arguments in favour of an interior magnetic field put forward in chapter 2. In the absence of such a magnetic field, the burrowing MMCs described by [Spiegel & Zahn \(1992\)](#) would ventilate the outer part of the radiative envelope, thickening the tachocline and causing the helium settling layer to form much deeper than is observed. Furthermore, the region below the helium settling layer, inaccessible to MMCs driven from the convection zone, would probably not be spun down as efficiently, leading to a rapidly rotating core. This point is discussed further in the next chapter.

Chapter 6

Depletion of Lithium and Beryllium

Observations of solar-type stars indicate that the surface lithium abundance decreases with age on the main sequence (e.g. [Soderblom *et al.*, 1990](#)), although not all stars fit the general trend (e.g. [Gaidos, 1998](#)). The Sun seems to be a particularly extreme example of lithium depletion; the lithium to hydrogen ratio in the solar convection zone is now less than 1% of its primordial value ([Vauclair *et al.*, 1978](#); [Asplund *et al.*, 2009](#)). The surface beryllium abundance is less well determined by observations (e.g. [Pinsonneault & Delahaye, 2009](#)) but is believed to be at least half of the primordial value.

Many mechanisms for lithium depletion in stars have been proposed, including gravitational settling ([Michaud, 1986](#)), convection-zone dilution caused by mass loss ([Weymann & Sears, 1965](#)), and various sources of internal mixing (e.g. [García López & Spruit, 1991](#); [Charbonnel *et al.*, 1992](#); [Fritts *et al.*, 1998](#); [Israelian *et al.*, 2009](#), & refs). Nearly all¹ of the proposed mechanisms rely on the fact that ${}^7\text{Li}$ is destroyed (or “burned”) by proton capture at around 2.5×10^6 K ([Michaud & Charbonneau, 1991](#)). This is the temperature of the solar interior at a depth of about $0.05R_{\odot}$ below the bottom of the convection zone (e.g. [Christensen-](#)

¹The gravitational settling mechanism proposed by [Michaud \(1986\)](#) is an exception. This mechanism is not thought to be particularly relevant to the Sun, since it would tend to deplete lithium and beryllium equally, but it may contribute to the “lithium dip” observed in F stars ([Boesgaard & Tripicco, 1986](#)).

Dalsgaard *et al.*, 1992). If material from this depth is efficiently mixed into the convection zone then the surface depletion of lithium can be explained. If the mixed region extends significantly beyond $0.1R_{\odot}$ below the bottom of the convection zone, where the temperature exceeds 3×10^6 K, then the convection zone’s beryllium will also be burned.² The surface abundance observations therefore impose tight constraints on the degree of mixing within the solar interior.

Arguably the simplest process that can produce the required mixing is main-sequence mass loss (Weymann & Sears, 1965). As matter is lost from the solar surface, the Sun’s internal structure adjusts, and layers below the convection zone that were previously hot enough to burn lithium become cooler. If the rate of mass loss is sufficiently fast, then the cool, lithium-poor layers may become convectively unstable, leading to “lithium dilution” in the convection zone. However, the mass-loss rate would need to be quite finely tuned in order to dilute the convection zone’s lithium by a factor of 100 without greatly diluting the beryllium as well (Swenson & Faulkner, 1992).

The mean meridional circulations (MMCs) described in chapter 2 can transport lithium, as well as angular momentum, within the radiative envelope. This is another potential source of mixing, which may be further enhanced by shear instabilities and turbulence triggered by the angular momentum transport. This combination of processes is often called “rotational mixing” (e.g. Charbonnel *et al.*, 1992). The early models of rotational mixing sought to explain both the spin-down of the solar interior and the depletion of lithium in the convection zone simultaneously. However, the limits on interior mixing implied by the surface beryllium abundance make it difficult to explain solar spin-down by this mechanism. Furthermore, the production of helium in the Sun’s core establishes strong, stable compositional stratification deep within the radiative interior (figure 5.1) which practically forbids the propagation of MMCs into that region (Mestel, 1953). Therefore models based entirely on rotational mixing tend to have a rapidly rotating core, which contradicts the current measurements from helioseismology.

Another potential source of turbulence and mixing in the solar interior arises

²Although rapid beryllium burning occurs only at temperatures exceeding 3.4×10^6 K (e.g. Christensen-Dalsgaard *et al.*, 1991).

from internal gravity waves. As described in §2.4, gravity waves generated at the bottom of the convection zone can transport angular momentum within the interior. This transport can induce MMCs and turbulence, and hence lead to mixing (e.g. [Fritts *et al.*, 1998](#)).

Using a combination of rotational mixing and gravity wave mixing, [Charbonnel & Talon \(2005\)](#) constructed a model that can simultaneously explain spin-down and lithium depletion within the solar interior. In their model, differential rotation within the interior is assumed to drive turbulence that maintains constant angular velocity on each spherical surface (see §2.4). This turbulence also dissipates internal gravity waves generated by the convection zone’s turbulent stresses, leading to spin-down. At the same time, rotational mixing below the convection zone leads to lithium depletion. Spin-down by gravity waves is an essential part of this picture — without a mechanism for reducing the vertical shear in the interior, their model would produce too much mixing, and therefore too much lithium depletion.

However, the angular momentum transport produced by internal gravity waves is sensitive to the manner in which the waves are generated and dissipated (§2.4). Furthermore, the presence of a fossil magnetic field in the radiative envelope would strongly inhibit the MMCs required for rotational mixing, as described in chapter 3. In the [GM98](#) model, it was argued that MMCs would be able to burrow into the radiative envelope only at the polar “weak spots” of the dipolar magnetic field (figure 4.2). To produce lithium depletion in the convection zone, these “polar pits” would need to be well ventilated and deep enough to burn lithium. However, in this model the effects of compositional stratification were neglected. In the revised model presented by [McIntyre \(2007\)](#) the existence of polar pits was ruled out by the μ -choke from the the helium settling layer. Instead, it was conjectured that the outer $0.1R_{\odot}$ of the radiative envelope is ventilated by a combination of MMCs and MHD turbulence (see appendix G), and that the helium settling layer forms below this ventilated region. At the time, the uncertainties in the helioseismic evidence described in §2.2 permitted such speculation ([Christensen-Dalsgaard & di Mauro, 2007](#)). But more recent work seems to confirm that the top of the helium settling layer is in fact located significantly higher than $0.6R_{\odot}$ ([Christensen-Dalsgaard & Gough, in preparation](#)).

This suggests that the Sun’s lithium must have been depleted in the early stages of the main sequence, before the formation of the helium settling layer. (This hypothesis has some support from observations, e.g. [Chen *et al.* \(2001\)](#).)

In Part [III](#) we will develop a self-consistent model of magnetic field confinement in the high-latitude tachocline that allows us to test some of the speculation in [GM98](#) and [McIntyre \(2007\)](#). In Part [IV](#) we will discuss the implications of our model for solar lithium depletion.

As a postscript to this review of lithium depletion, we note that the theories outlined above all need to be rather finely tuned in order to produce the observed 99% depletion of lithium in the Sun’s convection zone. Such fine tuning would not be necessary if it could be shown that lithium is actively *produced* in the outer layers of the Sun, for example by spallation in solar flares (e.g. [Christian & Mathioudakis, 2000](#)). In that case the observations could be explained even if all the convection zone’s lithium were destroyed early in the main sequence ([Guzik *et al.*, 1987](#)). However, most “autogenesis” theories predict a higher ratio of ${}^6\text{Li}/{}^7\text{Li}$ than is observed ([Feast, 1966](#); [Soderblom *et al.*, 1990](#)).

Part III

The Magnetic Confinement Layer

Chapter 7

The High-Latitude Tachocline

7.1 The structure of the magnetic field

Based on the arguments put forward in Parts I and II, we now attempt to construct a global model of angular momentum balance and magnetic field confinement in the solar tachocline. Our focus will be on today’s Sun, as inferred from helioseismology. However, in Part IV we will consider the implications of our model for the early main-sequence Sun, with particular regard to lithium depletion.

Figure 7.1 is a sketch suggesting the simplest possible structure for the time-averaged magnetic field in the tachocline. The inner, grey sphere represents the top of the helium settling layer. In high latitudes, the field lines emerging from the helium settling layer are swept aside by the tachocline’s downwelling MMC. The latitudinal shear in the tachocline winds up these field lines, transmitting a prograde “Alfvénic torque” to high latitudes, as required to confine the downwelling MMC. We presume that the time-averaged effect of convective overshoot and other turbulent processes in the tachocline is to hold the field lines horizontal in middle and low latitudes, as described in §4.1. We presume also that the turbulent processes act in the manner of a magnetic diffusivity, preventing the field lines from being wound up arbitrarily tightly by the latitudinal shear.

Assuming that the high-latitude confinement layers at either pole behave in a

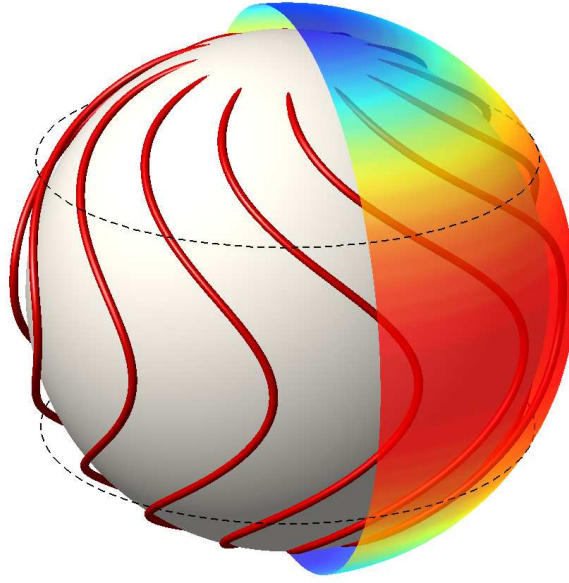


Figure 7.1: Sketch of the time-averaged magnetic field in the tachocline. Poloidal magnetic field lines (red) emerge from the helium settling layer (inner sphere) in high latitudes, and are wound up by differential rotation in the tachocline, acting against eddy diffusion. A prograde Alfvénic torque is transmitted from low to high latitudes along these field lines. The cutaway outer sphere, which represents the bottom of the convection zone, is shaded according to angular velocity. The dashed lines indicate the latitudes at which the rotation of the convection zone matches that of the interior, $\Omega_i = 2.7 \times 10^{-6} \text{s}^{-1}$.

similar fashion, the field lines must emerge from the helium settling layer with no toroidal component B_ϕ . Otherwise an Alfvénic torque would be exerted on the top of the helium settling layer at either pole, producing torsional oscillations within the apple-core region between the two confinement layers. A similar topological constraint arises in the simulations of Braithwaite & Spruit (2004), although in their case it results from the assumption of perfectly insulating boundaries (see figure 3.1 in §3.1). There must still be a nonvanishing B_ϕ component deeper within the interior, in order to stabilise the neutral ring of the dipolar field (again see figure 3.1).

7.2 The structure of the tachocline

It is apparent from the discussions in chapter 4 that the high-latitude regions are the most critical to the magnetic confinement problem. Our aim in the following

chapters is to construct a fully self-consistent model of the high-latitude magnetic confinement layer, based on the global picture presented in figure 7.1. We seek to describe the complete vertical structure of the confinement layer, including how it matches on to the mean-field-free tachocline above, and on to the Ferraro-constrained radiative envelope below. However, we do not attempt to describe in detail the turbulent processes within the convection zone and tachocline that pump the downwelling MMC responsible for confining the field. To do so would require an accurate description of the (magneto)hydrodynamic turbulence within the convection zone and tachocline, which is beyond the scope of this study. The existence of downwelling in the high-latitude tachocline is strongly supported by the arguments in §2.3.2 and §4.2.1 (see also appendix G and discussions in Part IV).

Since our focus is on today’s Sun, our model must describe how the structure of the confinement layer is affected by the presence of the compositionally stratified helium settling layer in the outer part of the radiative envelope. As described in chapter 5, the μ -choke from the settling layer will severely limit the magnitude and scale of any MMCs within that region. The downwelling MMC that confines the magnetic field in high-latitudes must therefore feed into an equatorward flow immediately above the helium settling layer. In the absence of helium diffusivity, we would expect a discontinuity in the vertical compositional gradient at the interface between the magnetic confinement layer and helium settling layer, as in the model of McIntyre (2007). Here, we shall allow for finite helium diffusivity, and so the change in the compositional gradient will be resolved over a thin “helium sublayer”.

Figure 7.2 shows a vertical cross-section through the confinement layer in a region surrounding the north pole.

7.3 Angular momentum balance

The most crucial role of the interior magnetic field is to supply angular momentum to the high-latitude confinement layer, and thereby to prevent the tachocline’s MMCs from burrowing into the radiative envelope. Consider the overall angular

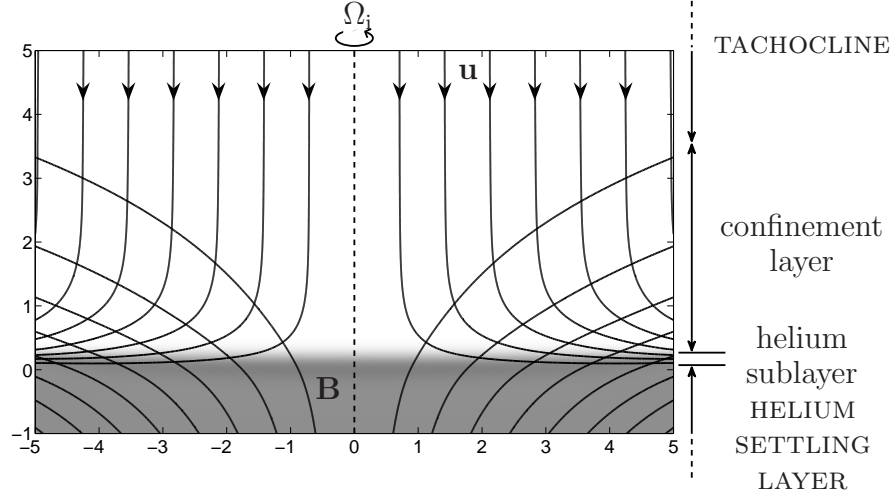


Figure 7.2: The magnetic confinement layer near the north pole. The field strength falls off exponentially with altitude. The streamlines with arrows show the downwelling responsible for the confinement. Compositional stratification is indicated by shading. With typical parameters the confinement layer is a fraction of a megametre thick. The plot is from a numerical solution of the confinement-layer equations (§7.4). The horizontal and vertical axes are colatitude and altitude in units of the magnetic advection–diffusion length $\delta_\eta = \eta/U$.

momentum balance in the cylindrical volume illustrated in figure 7.2, which we denote as V . Adopting cylindrical polar coordinates (r, ϕ, z) , angular momentum balance in the non-rotating frame can be expressed as

$$\int_{\partial V} r \rho u_\phi \mathbf{u} \cdot d\mathbf{S} = \frac{1}{4\pi} \int_{\partial V} r B_\phi \mathbf{B} \cdot d\mathbf{S} + \int_{\partial V} r^2 \rho \nu \nabla \left(\frac{u_\phi}{r} \right) \cdot d\mathbf{S} , \quad (7.1)$$

i.e. the net flux of angular momentum into or out of the volume V must be balanced by Maxwell and viscous stresses exerted over the boundary, ∂V . Provided that departures from uniform rotation remain small, the system will be magnetostrophic, i.e. Coriolis and Lorentz forces will dominate viscous and relative inertial forces. We may then approximate $u_\phi \approx \Omega_i r$, so that (7.1) becomes

$$\int_{\partial V} r^2 \rho \Omega_i \mathbf{u} \cdot d\mathbf{S} \approx \frac{1}{4\pi} \int_{\partial V} r B_\phi \mathbf{B} \cdot d\mathbf{S} . \quad (7.2)$$

For any flow qualitatively like that in figure 7.2 the left-hand side of (7.2) is positive — i.e. the flow produces a net export of angular momentum. To maintain balance, angular momentum must be supplied by the magnetic field, via an Alfvénic torque over the boundary ∂V . In principle this Alfvénic torque can be supplied either over the bottom of the domain, or over its periphery, or a com-

bination of the two. However, as discussed in §7.1, any Alfvénic torque exerted on the top of the helium settling layer in high-latitudes will lead to torsional oscillations in the apple-core region between the two polar confinement layers. Therefore, in the steady state, the Alfvénic torque over the bottom of the domain V must vanish. This is equivalent to the condition that $B_\phi = 0$ over the bottom of the domain. This boundary condition ensures that the Alfvénic torque on the confinement layer comes exclusively from the confinement layer’s sideways connection to low latitudes,¹ via field lines like those sketched in figure 7.1.

7.4 The equations and parameters

Within the high-latitude cylindrical domain shown in figure 7.2 we may take gravity to be uniform and anti-parallel to the rotation axis. We impose uniform downwelling of magnitude U through the top of the domain, and an axial dipolar magnetic field underneath to represent the interior magnetic field \mathbf{B}_i . We anticipate that the characteristic vertical scale of the magnetic confinement layer will be the magnetic advection–diffusion length $\delta_\eta = \eta/U$, where the magnetic diffusivity² $\eta \approx 4.1 \times 10^2 \text{cm}^2 \text{s}^{-1}$. If the imposed downwelling U has magnitude $\sim 10^{-5} \text{cm s}^{-1}$ then this lengthscale is $\sim 0.4 \text{Mm}$, which is far smaller than the local pressure scale height, $H_p \approx 60 \text{Mm}$. We may therefore employ the Boussinesq approximation in modelling the confinement layer.

We work in a frame rotating with the same angular velocity as the interior, $\Omega_i = 2.7 \times 10^{-6} \text{s}^{-1}$. We nondimensionalise the Boussinesq equations using δ_η as the lengthscale, U as the scale for the velocity field \mathbf{u} , and δ_η/U as the timescale, $\sim 10^5 \text{yr}$ if $U \sim 10^{-5} \text{cm s}^{-1}$. We measure the magnetic field \mathbf{B} in units of Alfvén speed, 0.6cm s^{-1} per gauss at a tachocline density of 0.2g cm^{-3} , and nondimensionalise \mathbf{B} with respect to $(2\Omega_i\eta)^{1/2} \approx 0.05 \text{cm s}^{-1}$. The significance of this scaling will be explained in chapter 8. We suppose that the thermal and compositional stratifications are approximately uniform within the helium settling layer, shaded

¹If the interior field were assumed to be a quadrupole, rather than a dipole, then part of the Alfvénic torque could be transmitted from low to high latitudes via the deep radiative interior. However, it is not known whether a quadrupolar interior field can be dynamically stable, so here we consider only the simpler, dipolar case illustrated in figure 7.1.

²Values for all the relevant dimensional parameters in the tachocline are listed in appendix A.

in figure 7.2. Writing \hat{T} and $\hat{\mu}$ for the fractional perturbations of temperature and mean molecular weight, we define the buoyancy frequencies N_T and N_μ to be exactly constant at the bottom of the domain,

$$\left. \frac{\partial \hat{T}}{\partial z} \right|_{\text{bottom}} = \frac{N_T^2 \delta_\eta}{g} = \text{const.}, \quad (7.3)$$

$$\left. \frac{\partial \hat{\mu}}{\partial z} \right|_{\text{bottom}} = -\frac{N_\mu^2 \delta_\eta}{g} = \text{const.}, \quad (7.4)$$

where z is now the dimensionless axial or altitude coordinate. At the top of the helium settling layer we have $N_T \approx 0.8 \times 10^{-3} \text{s}^{-1}$, and $N_\mu \approx 0.5 \times 10^{-3} \text{s}^{-1}$ (appendix A). In place of \hat{T} and $\hat{\mu}$ we define dimensionless rescaled quantities T and μ by

$$\frac{N_T^2 \delta_\eta}{g} T = \hat{T}, \quad (7.5)$$

$$\frac{N_\mu^2 \delta_\eta}{g} \mu = \hat{\mu}. \quad (7.6)$$

The thermal and compositional diffusivities are denoted respectively by $\kappa \approx 1.4 \times 10^7 \text{ cm}^2 \text{s}^{-1}$ and $\chi \approx 0.9 \times 10^1 \text{ cm}^2 \text{s}^{-1}$. We then arrive at the following dimensionless Boussinesq equations,

$$\begin{aligned} \text{Ro} \frac{D\mathbf{u}}{Dt} + \mathbf{e}_z \times \mathbf{u} &= -\nabla p + \alpha_T T \mathbf{e}_z - \alpha_\mu \mu \mathbf{e}_z \\ &+ (\nabla \times \mathbf{B}) \times \mathbf{B} + \text{Ek} \nabla^2 \mathbf{u} \end{aligned} \quad (7.7)$$

$$0 = \nabla \cdot \mathbf{u} \quad (7.8)$$

$$\frac{\partial \mathbf{B}}{\partial t} = \nabla \times (\mathbf{u} \times \mathbf{B}) + \nabla^2 \mathbf{B} \quad (7.9)$$

$$0 = \nabla \cdot \mathbf{B} \quad (7.10)$$

$$\frac{DT}{Dt} = \frac{\kappa}{\eta} \nabla^2 T \quad (7.11)$$

$$\frac{D\mu}{Dt} = \frac{\chi}{\eta} \nabla^2 \mu \quad (7.12)$$

where $D/Dt = \partial/\partial t + \mathbf{u} \cdot \nabla$, the Lagrangian or material derivative, and where \mathbf{e}_z is the unit vector parallel to the rotation axis. We have defined four dimensionless

coefficients Ro , Ek , and

$$\alpha_T = \frac{N_T^2 \delta_\eta^2}{2\Omega_i \eta}, \quad \alpha_\mu = \frac{N_\mu^2 \delta_\eta^2}{2\Omega_i \eta}; \quad (7.13)$$

Ro and Ek are Rossby and Ekman numbers defined by

$$\text{Ro} = \frac{U/\delta_\eta}{2\Omega_i}, \quad \text{Ek} = \frac{\nu}{2\Omega_i \delta_\eta^2} = \frac{\nu}{\eta} \text{Ro} \quad (7.14)$$

where ν is the kinematic viscosity, the sum of molecular and radiative contributions, $\approx 2.7 \times 10^1 \text{ cm}^2 \text{ s}^{-1}$ (appendix A). In (7.12) we have neglected gravitational settling, an excellent approximation in virtue of the short timescale of the confinement-layer dynamics relative to the Sun's lifetime.

For $U \sim 10^{-5} \text{ cm s}^{-1}$ the Rossby number is tiny, $\text{Ro} \sim 0.5 \times 10^{-7}$, and the Ekman number is smaller still, because $\nu/\eta \approx 0.7 \times 10^{-1}$. To excellent approximation, therefore, the flows under consideration will be magnetostrophic. In (7.7) the Coriolis force will be balanced against the combined pressure-gradient, buoyancy and Lorentz forces:

$$\mathbf{e}_z \times \mathbf{u} = -\nabla p + \alpha_T T \mathbf{e}_z - \alpha_\mu \mu \mathbf{e}_z + (\nabla \times \mathbf{B}) \times \mathbf{B}. \quad (7.15)$$

For simplicity we restrict attention to axisymmetric steady states. Then the azimuthal components of (7.15) and its curl are respectively

$$u_r = \frac{1}{r} \mathbf{B} \cdot \nabla (r B_\phi), \quad (7.16)$$

$$\frac{\partial u_\phi}{\partial z} = \alpha_T \frac{\partial T}{\partial r} - \alpha_\mu \frac{\partial \mu}{\partial r} + \frac{1}{r} \frac{\partial}{\partial z} (B_\phi^2) - r \mathbf{B} \cdot \nabla \left(\frac{[\nabla \times \mathbf{B}]_\phi}{r} \right) \quad (7.17)$$

where r is the dimensionless perpendicular distance from the rotation axis, and where suffixes (r, ϕ, z) denote vector components in cylindrical polar coordinates.

Equation (7.16) represents the local torque balance about the rotation axis, after multiplication by r (cf. equation (7.2)). It describes how the retrograde Coriolis torque from the equatorward flow is balanced by the prograde Lorentz torque from the confined magnetic field. Equation (7.17) represents low Rossby number thermal-wind balance generalised to include compositional gradients and the

Lorentz force-curl. In the upper part of figure 7.2, where the magnetic field and compositional stratification are both negligible, this balance becomes the standard thermal-wind balance

$$\frac{\partial u_\phi}{\partial z} = \alpha_T \frac{\partial T}{\partial r} \quad (7.18)$$

(cf. equation (1.2)).

7.5 The limit of infinite stratification

Equation (7.17) describes how the Coriolis and Lorentz force-curves act to tilt the stratification surfaces. Now if the stable stratification is sufficiently strong, i.e. if α_T and α_μ are both sufficiently large, then the tilting will be only slight. With $U \sim 10^{-5} \text{cm s}^{-1}$ we have

$$\alpha_T \sim 5 \times 10^{11} \quad (7.19)$$

$$\text{and} \quad \alpha_\mu \sim 2 \times 10^{11}. \quad (7.20)$$

So we anticipate that both the thermal and compositional stratification surfaces will be nearly “flat”, meaning gravitationally horizontal, within the confinement layer. This flatness will be more precisely quantified in chapters 8 and 9 using scale analysis. In fact, the analysis in chapter 9 shows that, to a first approximation, the helium sublayer can be modelled as an impermeable, frictionless, horizontal lower boundary.

If we take the asymptotic limit in which $\alpha_T, \alpha_\mu \rightarrow \infty$, with \mathbf{u} and \mathbf{B} both finite, then we may seek solutions in which the stratification surfaces are perfectly flat, i.e. $T = T(z)$ and $\mu = \mu(z)$. It then proves possible to solve the steady-state confinement-layer equations analytically, as a system of coupled ordinary differential equations, as we now show. We will refer to these analytical solutions as “perfectly flat”.

In the limit of perfect flatness, (7.11) and (7.12) imply for steady flow that

$$u_z = \frac{\kappa}{\eta} \frac{d}{dz} \ln \frac{dT}{dz} = \frac{\chi}{\eta} \frac{d}{dz} \ln \frac{d\mu}{dz}. \quad (7.21)$$

Therefore u_z is a function of z alone, $u_z = u_z(z)$. From (7.8) it then follows that u_r is r times a function of z alone, on the assumption of regularity at the pole $r = 0$. We say that the poloidal velocity field is “horizontally self-similar”, since it is invariant under a uniform stretching of the horizontal coordinates.³ The induction equation (7.9) then permits a steady poloidal magnetic field that is horizontally self-similar in the same sense. Equations (7.7)–(7.10) then reduce to

$$ru_r = \mathbf{B} \cdot \nabla(rB_\phi) \quad (7.22)$$

$$0 = \frac{1}{r} \frac{\partial(ru_r)}{\partial r} + \frac{du_z}{dz} \quad (7.23)$$

$$r\mathbf{u} \cdot \nabla \frac{B_\phi}{r} = r\mathbf{B} \cdot \nabla \frac{u_\phi}{r} + \left(\nabla^2 - \frac{1}{r^2} \right) B_\phi \quad (7.24)$$

$$u_z \frac{dB_z}{dz} = B_z \frac{du_z}{dz} + \frac{d^2 B_z}{dz^2} \quad (7.25)$$

$$0 = \frac{1}{r} \frac{\partial(rB_r)}{\partial r} + \frac{dB_z}{dz} . \quad (7.26)$$

This is a complete set because perfect flatness implies that the meridional components of (7.7) are not needed; more precisely, equation (7.17) becomes degenerate in the limit where $\alpha_T, \alpha_\mu \rightarrow \infty$ and $\partial T/\partial z, \partial \mu/\partial z \rightarrow 0$. The azimuthal component of (7.7) is replaced by (7.16) and multiplied by r to give (7.22), expressing the balance between Coriolis and Lorentz torques. Equations (7.23)–(7.26) correspond to (7.8)–(7.10); equations (7.11) and (7.12) have no further role, beyond their connection to the downwelling expressed by (7.21).

Equations (7.22)–(7.26) represent a slight generalisation of the confinement-layer equations presented by Wood & McIntyre (2007, hereafter WM07). In particular, equation (7.24) permits more general toroidal magnetic and differential-rotation fields than were considered by WM07. Perhaps surprisingly, these equations admit a family of solutions in which the function $u_z(z)$ is arbitrary except for certain restrictions on its asymptotic behaviour as $z \rightarrow \pm\infty$. In particular, we require $u_z(z) \rightarrow -1$ as $z \rightarrow +\infty$ and $u_z(z) \rightarrow 0$ as $z \rightarrow -\infty$. The necessary restrictions will shortly be made more precise. Solutions can be most conveniently

³This horizontal self-similarity is an indication that the confinement layer’s intrinsic horizontal lengthscale becomes infinite in the asymptotic limit $\alpha_T, \alpha_\mu \rightarrow \infty$. This is confirmed by the scale analysis in chapters 8 and 9.

constructed by specifying a suitable $u_z(z)$ at the start even though, in virtue of (7.21), we could instead choose to specify either $T(z)$ or $\mu(z)$.

With $u_z(z)$ specified, we can find $B_z(z)$ immediately by solving the vertical component (7.25) of the induction equation as a linear ordinary differential equation, assuming that B_z vanishes far above the confinement layer ($z \rightarrow +\infty$) and that it matches on to the interior dipolar magnetic field structure beneath ($z \rightarrow -\infty$). The interior dipole has the same horizontally self-similar structure as the confinement layer, with components satisfying $B_{i\phi} = 0$, $B_{ir}/r = \text{constant}$, and B_{iz} a linear function of z consistent with (7.26). Even though the balance in (7.25) is not simple advective–diffusive, we find that B_z decays upward like $\exp(-z)$.

The radial components of \mathbf{u} and \mathbf{B} can be found directly from their vertical components, by using (7.23) and (7.26) and assuming regularity at the pole $r = 0$:

$$u_r = -\frac{r}{2} \frac{du_z}{dz}, \quad (7.27)$$

$$B_r = -\frac{r}{2} \frac{dB_z}{dz}. \quad (7.28)$$

So once we have $B_z(z)$ we can calculate B_r from (7.28), and then the toroidal field B_ϕ from (7.22) by using (7.27) and taking advantage of the hyperbolic character of the operator $\mathbf{B} \cdot \nabla$. By calculating B_ϕ in this way, we ensure that the Lorentz torque balances the Coriolis torque along each magnetic field line. Requiring that $B_\phi(r, z) \rightarrow 0$ for all r as $z \rightarrow -\infty$ leads to the following, unique solution of (7.22):

$$B_\phi = B_z \int_{-\infty}^z \frac{u_r}{B_z^2} dz. \quad (7.29)$$

For any u_r profile that decays exponentially as $z \rightarrow -\infty$, this solution for B_ϕ , and with it the Maxwell stress and Alfvénic torque, will also decay exponentially as $z \rightarrow -\infty$. The expression (7.29) then shows that B_ϕ has the same self-similar functional form as u_r and B_r , namely r times a function of z alone.

To ensure that \mathbf{B}_ϕ decays aloft, as $z \rightarrow +\infty$, it is sufficient to assume that

$$u_r = O(\exp(-\gamma z)) \quad \text{as } z \rightarrow +\infty \quad (7.30)$$

where $\gamma > 1$, implying that $u_z(z) \sim -1 + O(\exp(-\gamma z))$. The three cases $\gamma > 2$, $\gamma = 2$, and $2 > \gamma > 1$ need separate consideration. When $\gamma > 2$, the only case considered in WM07, the integral in (7.29) converges to a constant plus $O(\exp(-(\gamma-2)z))$ as $z \rightarrow +\infty$. That in turn means that B_ϕ decays upward like $\exp(-z)$. When $\gamma = 2$, the integral in (7.29) asymptotes to a linear function of z , and B_ϕ decays upward like $z \exp(-z)$. When $2 > \gamma > 1$, the integral in (7.29) increases upward like $\exp((2-\gamma)z)$, but B_ϕ still decays upward, like $\exp(-(\gamma-1)z)$.

In all these cases it is clear from (7.29) that B_ϕ does not have exactly the same z -dependence aloft as does B_z , as might have been expected from advective–diffusive balance with advection by constant downwelling $u_z = -1$. Having the same z -dependences would make the right-hand side of (7.22) vanish. Hence it is the more or less subtle *departures* from advective–diffusive balance, including the contribution to B_ϕ from the twisting of field lines by the differential rotation u_ϕ , that enable the Lorentz torque on the right of (7.22) to support the flow u_r at all altitudes.

The u_ϕ field that does the twisting can be calculated next, from (7.24) and the condition that the interior rotates uniformly, $u_\phi \rightarrow 0$ as $z \rightarrow -\infty$. Again this calculation depends on the hyperbolic character of the operator $\mathbf{B} \cdot \nabla$. When B_ϕ is given by (7.29) we have, uniquely,

$$u_\phi = \int_{-\infty}^z \left(u_z \frac{\partial B_\phi}{\partial z} - \frac{\partial^2 B_\phi}{\partial z^2} \right) \frac{dz}{B_z} \quad (7.31)$$

showing that u_ϕ is also r times a function of z alone. That is, the differential rotation is shellular solid rotation. In the three cases $\gamma > 2$, $\gamma = 2$, and $2 > \gamma > 1$, the behaviours of u_ϕ as $z \rightarrow +\infty$ are respectively $u_\phi \sim \text{constant}$, $u_\phi \sim \pm z$, and $u_\phi \sim \pm \exp((2-\gamma)z)$.

Cases with negative shear aloft, $\partial u_\phi / \partial z < 0$ — especially the last case, with exponentially-increasing negative shear aloft — are suggestive of a possible way to match upwards to the observed, much stronger negative shear in the bulk of the tachocline. By using (7.29) to eliminate B_ϕ from $\partial / \partial z$ of (7.31), then using (7.25) to eliminate $d^2 B_z / dz^2$ and (7.27) to eliminate du_z / dz , we find

$$\frac{\partial u_\phi}{\partial z} = \frac{u_z u_r}{B_z^2} - \frac{1}{B_z^2} \frac{\partial u_r}{\partial z} - \frac{2u_r}{r} \int_{-\infty}^z \frac{u_r}{B_z^2} dz \approx (\gamma-1) \frac{u_r}{B_z^2} \quad \text{as } z \rightarrow \infty. \quad (7.32)$$

The asymptotic behaviour on the right comes from the first two terms in the exact expression. The third term involving the integral is smaller by a factor $O(\exp(-\gamma z))$. Asymptotically, therefore, the sign of the shear $\partial u_\phi / \partial z$ aloft is the same as the sign of u_r aloft. We can therefore find solutions that match on to the strong negative tachocline shear provided that there is an exponentially weak poleward mass flux above the confinement layer. However, a more precise description of such matching may well need to take account of other sensitivities aloft (see discussions in §§10.3, 10.5), including a sensitivity to slight departures from magnetostrophic balance due to small-scale MHD turbulence (e.g. Parfrey & Menou, 2007, & refs.), as well as slight departures from perfect flatness.

Although the structure aloft is sensitive to the precise conditions as $z \rightarrow +\infty$, the solutions (7.29) and (7.31) show that, by contrast, the structure of the rest of the confinement layer is relatively insensitive. An illustrative solution is plotted in figure 7.3. In this case the interior field \mathbf{B}_i has $B_r/r = 1$. The downwelling profile $u_z(z)$ was adapted from the numerical solution shown in figure 7.2, as described in §10.5, and has $\gamma = 2.24$. For other γ values the bottom half of each plot looks qualitatively the same, whereas the top half may in some cases be wildly different; again see §10.5.

Some three-dimensional streamlines and magnetic field lines corresponding to the solution in figure 7.3 are plotted in figure 7.4, visualising how the prograde Lorentz torque on the right of (7.22), associated with field-line curvature, balances the retrograde Coriolis torque on the left of (7.22) and satisfies the overall torque balance (7.2).

7.6 Finite stratification

The perfectly flat confinement-layer equations (7.22)–(7.26) are formally valid only in the limit $\text{Ro}, \text{Ek} \rightarrow 0$ and $\alpha_T, \alpha_\mu \rightarrow \infty$. Allowing for finite α_T or α_μ introduces non-flat corrections to the solutions. In chapters 8 and 9 we consider the scalings and dynamics within the confinement layer and helium sublayer respectively, in order to estimate the magnitude of these corrections.

The full equations (7.7)–(7.12), with finite $\text{Ro}, \text{Ek}, \alpha_T$ and α_μ , are solved numeri-

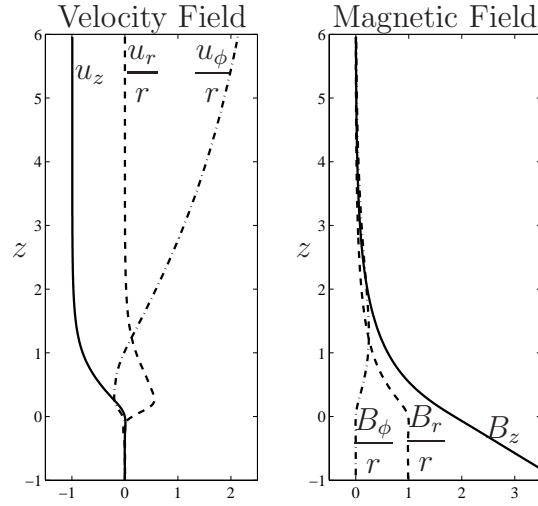


Figure 7.3: Vertical profiles from a perfectly flat solution of the confinement-layer equations in the limit $\alpha_T, \alpha_\mu \rightarrow \infty$. The downwelling profile $u_z(z)$, solid curve on left, was chosen to match the downwelling profile from the numerical solution shown in figure 7.2. For numerical reasons, small adjustments were made to this profile in the “slippery” region $z > 1.5\delta_\eta$ — see §10.5. In (7.30) the decay constant $\gamma = 2.24$, and the u_ϕ profile therefore approaches a constant like $\exp(-0.24z)$.

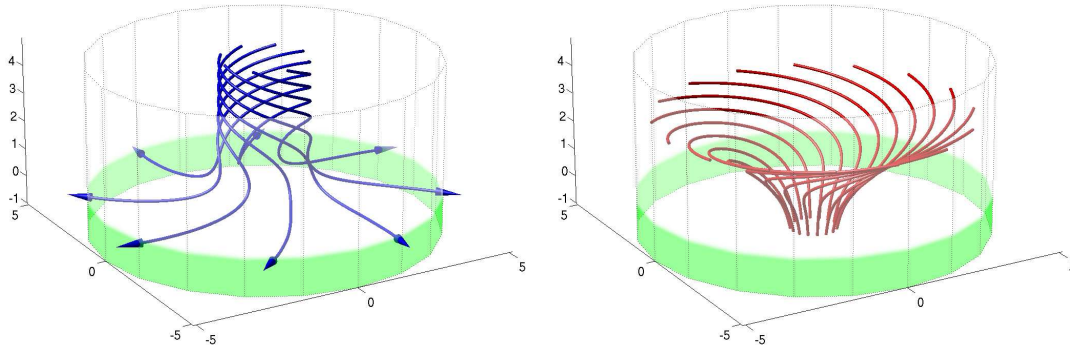


Figure 7.4: Streamlines (left) and magnetic field lines (right) in a perfectly flat solution of the confinement-layer equations, whose vertical profiles are displayed in figure 7.3. The peripheral shading indicates the helium settling layer and helium sublayer.

cally in chapter 10. The numerical solutions verify the results of chapters 8 and 9, and provide additional insights. In particular, they confirm that the thermal and compositional stratification surfaces are very nearly flat within the confinement layer and sublayer, provided that the stable stratification is realistically strong. The vertical cross-section shown in figure 7.2 is taken from a numerical solution; the slight concavity of the helium surfaces, for example, is barely visible.

The numerical solutions of chapter 10 also verify that the flows within the confinement layer and sublayer are magnetostrophic to excellent approximation. However, magnetostrophic balance becomes more delicate in the upper part of the flow, wherein the Lorentz and Coriolis forces become vanishingly small. This lends a certain “slipperiness” to the solutions, one symptom of which is the abovementioned sensitivity of the perfectly flat solutions to the exact value of γ .

7.7 Summary

The results of section 7.5 may be summarised as follows:

- In the strongly stratified, magnetostrophic limit, the confinement-layer equations reduce to (7.22)–(7.26), which can be solved for any chosen profile of $u_z(z)$.
- In order for the magnetic field $|\mathbf{B}|$ to be confined, i.e. to decay exponentially as $z \rightarrow +\infty$, we require only that $u_z(z) \sim -1 + O(\exp(-\gamma z))$ as $z \rightarrow +\infty$, with $\gamma > 1$.
- If $u_z(z) \rightarrow 0$ as $z \rightarrow -\infty$ then there is a unique solution with uniform rotation and vanishing Alfvénic torque below the confinement layer.

It is therefore apparent that plausible confinement-layer solutions can be obtained with only minor restrictions on the downwelling profile $u_z(z)$. The physical interpretation of the considerable freedom this affords becomes clearer when considering the boundary conditions for the numerical solutions (§10.3).

Chapter 8

The Magnetic Confinement Layer

Consider the scaling regime within the bulk of the confinement layer, well above the helium sublayer. Because the photon mean free path makes the thermal diffusivity relatively large, $\kappa/\eta \sim 3 \times 10^4$, the confinement-layer flow only weakly perturbs the background thermal stratification. Consistently with (7.3) and (7.5) we define the temperature perturbation T' so that $T = z + \text{const.} + T'$. Then, sufficiently close to the pole, the leading-order balance in the steady-state thermal equation (7.11) involves only the vertical component u_z of \mathbf{u} ,

$$u_z = \frac{\kappa}{\eta} \nabla^2 T' . \quad (8.1)$$

From this we estimate the magnitude of the thermal anomaly to be $T' \sim \eta/\kappa \ll 1$. By contrast, the diffusivity of helium is relatively small, $\chi/\eta \approx 2 \times 10^{-2}$, so the diffusive flux of helium up into the bulk of the confinement layer is negligible. The confinement layer is therefore well ventilated, i.e. the mean molecular weight μ within the bulk of the confinement layer is close to being constant. Compositional stratification is important only in the helium sublayer and the helium settling layer, as indicated by the shading in figure 7.2 and further discussed in chapter 9.

The aim in this chapter is to estimate, using scale analysis, the characteristic horizontal lengthscale of the confinement-layer flow, and hence to quantify the “flatness” of the confinement layer. For the moment we do not assume axisymmetry. We therefore begin with the full set of equations (7.7)–(7.12). We neglect

the α_μ term in (7.7), since we expect the effects of compositional stratification to be negligible within the confinement layer, and therefore equation (7.12) plays no further role in the dynamics. We also use (8.1) in place of (7.11). Next, we assume that the confinement-layer flow is perfectly magnetostrophic, i.e. we neglect the $O(\text{Ro})$ and $O(\text{Ek})$ terms in (7.7). After taking the curl of (7.7) to eliminate the pressure force, the steady-state confinement-layer equations are

$$-\frac{\partial \mathbf{u}}{\partial z} = -\alpha_T \mathbf{e}_z \times \nabla T' + \mathbf{B} \cdot \nabla (\nabla \times \mathbf{B}) - (\nabla \times \mathbf{B}) \cdot \nabla \mathbf{B} \quad (8.2)$$

$$0 = \nabla \cdot \mathbf{u} \quad (8.3)$$

$$0 = \nabla \times (\mathbf{u} \times \mathbf{B}) + \nabla^2 \mathbf{B} \quad (8.4)$$

$$0 = \nabla \cdot \mathbf{B} \quad (8.5)$$

$$u_z = \frac{\kappa}{\eta} \nabla^2 T' . \quad (8.6)$$

We now assume that the horizontal scale of the confinement-layer flow is much larger than the vertical lengthscale δ_η , by a factor $F \gg 1$, say. We call F the “flatness number”, since it measures the characteristic aspect ratio of the confinement-layer flow. From (8.3) and (8.5) we deduce that the horizontal components of the velocity and magnetic fields must be larger than the respective vertical components by a factor of F . We therefore split all vector fields and operators into their vertical and horizontal components:

$$\mathbf{u} = u_z \mathbf{e}_z + \mathbf{u}_H , \quad (8.7)$$

$$\mathbf{B} = B_z \mathbf{e}_z + \mathbf{B}_H , \quad (8.8)$$

$$\nabla = \frac{\partial}{\partial z} \mathbf{e}_z + \nabla_H , \quad (8.9)$$

$$\nabla^2 = \frac{\partial^2}{\partial z^2} + \nabla_H^2 , \quad (8.10)$$

and assume that

$$u_z \sim 1, \quad |\mathbf{u}_H| \sim F, \quad (8.11)$$

$$B_z \sim 1, \quad |\mathbf{B}_H| \sim F, \quad (8.12)$$

$$\frac{\partial}{\partial z} \sim 1, \quad |\nabla_H| \sim 1/F. \quad (8.13)$$

By substituting definitions (8.7)–(8.10) into (8.2)–(8.6), and neglecting contribu-

tions $O(F^{-2})$, we obtain a set of boundary-layer equations for the confinement-layer flow. These boundary-layer equations have $\partial^2/\partial z^2$ in place of ∇^2 in (8.4) and (8.6), and the boundary-layer equivalent of (8.2) is

$$-\frac{\partial \mathbf{u}}{\partial z} = -\alpha_T \mathbf{e}_z \times \nabla T' + \mathbf{B} \cdot \nabla (\nabla \times \mathbf{B}_H) - (\nabla \times \mathbf{B}_H) \cdot \nabla \mathbf{B} . \quad (8.14)$$

We now define a set of “horizontally stretched” coordinates, with respect to which both the horizontal and vertical lengthscales of the confinement-layer flow are order unity. This is equivalent to rescaling all horizontal lengthscales and horizontal vector-field components by a factor of F . In the stretched coordinates, the vorticity equation (8.14) becomes

$$-\frac{\partial \mathbf{u}}{\partial z} = -\frac{\alpha_T}{F^2} \mathbf{e}_z \times \nabla T' + \mathbf{B} \cdot \nabla (\nabla \times \mathbf{B}_H) - (\nabla \times \mathbf{B}_H) \cdot \nabla \mathbf{B} , \quad (8.15)$$

but, crucially, the other equations are invariant. By comparing (8.14) and (8.15) we see that increasing the thermal stratification in the confinement layer, and thus increasing the parameter α_T , has the same effect as horizontally stretching the confinement-layer flow (boundary conditions permitting). Indeed, since each term in (8.15) is $O(1)$, we deduce that the characteristic flatness of the confinement layer is $F^2 \sim \alpha_T T'$. From (8.6) we have $T' \sim \eta/\kappa$, and so

$$F^2 \sim \alpha_T (\eta/\kappa) . \quad (8.16)$$

However, (8.11)–(8.13) implicitly assume that the two horizontal components of the vector fields \mathbf{u} and \mathbf{B} are of similar magnitude, and that B_z has a dimensionless magnitude of order unity. In Wood & McIntyre (2010) a more careful scale analysis was performed in a neighbourhood of the pole, assuming axisymmetry. In that case, the azimuthal and colatitudinal components of \mathbf{u} and \mathbf{B} are generally not of similar magnitude. If the dimensional magnitude of B_z at the bottom of the confinement layer is denoted as \mathbf{B} , then

$$B_z \sim \Lambda^{1/2} \quad (8.17)$$

$$\text{and} \quad \frac{u_r}{u_\phi} \sim \frac{B_r}{B_\phi} \sim \Lambda \quad (8.18)$$

where Λ is the Elsasser number based on the vertical component of the magnetic

field:

$$\Lambda = \frac{B^2}{2\Omega_i\eta}. \quad (8.19)$$

Because of axisymmetry, the thermal stratification surfaces are necessarily horizontal at the pole. Wood & McIntyre (2010) showed that tilting of the thermal stratification surfaces first becomes dynamically significant at a dimensionless distance $\sim r_T$ from the pole, where

$$r_T^2 = \alpha_T(\eta/\kappa) \min(\Lambda, \Lambda^{-1}). \quad (8.20)$$

Wood & McIntyre's r_T is therefore analogous to the flatness number F derived above. With $N_T \approx 0.8 \times 10^{-3} \text{s}^{-1}$, $U \sim 10^{-5} \text{cm s}^{-1}$, and $\Lambda \sim 1$, we have $r_T = F \sim 4 \times 10^3$. With these numbers, which imply $\delta_\eta \sim 0.4 \text{Mm}$, the dimensional colatitudinal distance at which the tilting of the thermal stratification surfaces first becomes significant is $r_T \delta_\eta \sim 1500 \text{Mm}$, roughly $2R_\odot$ away from the pole.¹

Of course our cylindrical model with its assumption of uniform downwelling will itself cease to apply, almost certainly, before we get as far as $r_T \delta_\eta$ from the pole. At some colatitude the downwelling must give way to upwelling. The confinement-layer regime cannot then apply even qualitatively. Instead, the interior magnetic field lines are free to advect and diffuse upward until they encounter the magnetic flux pumping associated with the convective overshoot layer, as assumed in figure 7.1.

With $\Lambda \sim 1$ and the other numbers just given, the interior field \mathbf{B}_i has dimensional orders of magnitude typified by $B_{ir} \sim 30 \text{cm s}^{-1}$, equivalently 50 gauss, at colatitude $\sim 30^\circ$, or a third of those values at colatitude $\sim 10^\circ$. Such $|\mathbf{B}_i|$ values are far above the threshold, more like 10^{-2} gauss, for the field strength required to enforce the Ferraro constraint in the interior (chapter 3). However, a separate question concerns the possible range of field strengths, and MHD turbulent intensities in the bulk of the tachocline, required to support the time-averaged picture suggested in figure 7.1. There, field strengths greater than 10^{-2} gauss might well be needed (e.g. appendix G).

¹Even when the tilting is significant, the slopes of the thermal stratification surfaces are far smaller than the geometrical aspect ratio r_T^{-1} , partly because of the parabolic shape of the stratification surfaces and partly because T' is only a small perturbation to the background stratification.

The range of interior field strengths accommodated by the confinement-layer regime is determined by (8.20). The condition for the regime to apply at least qualitatively within, say, 10° colatitude of the poles is $r_T \delta_\eta \gtrsim 90 \text{ Mm}$. We can use (8.20) together with realistic N_T and diffusivity values to write this condition as

$$\max(\Lambda, \Lambda^{-1}) \lesssim 3 \times 10^2 \left(\frac{U}{10^{-5} \text{ cm s}^{-1}} \right)^{-4}. \quad (8.21)$$

So for $U \sim 10^{-5} \text{ cm s}^{-1}$ the regime applies over a range of about five decimal orders of magnitude in Λ . If the downwelling is weaker then a much wider range of Λ values may become possible.

Chapter 9

The Helium Sublayer

9.1 Sublayer scalings

The helium sublayer marks the transition between the compositionally well-ventilated confinement layer and the nearly impermeable, compositionally stratified helium settling layer. The simplest description of the sublayer arises from neglecting both viscosity and helium diffusivity, as in [McIntyre \(2007\)](#). The sublayer is then infinitely thin, frictionless and impermeable, and the downwelling flow in the confinement layer feeds into a “slip-flow” immediately above the sublayer. The magnetic field lines crossing the sublayer are kinked by this slip-flow, to an extent that is limited by magnetic diffusion. In fact, the sublayer in this description is an example of the “magnetic Margules front” described in [appendix D](#), except that the slope of the sublayer is controlled by compositional rather than thermal stratification. Hence there is a discontinuity in the mean molecular weight μ across the sublayer.

To estimate the magnitude of the discontinuity in μ , and hence the slope of the sublayer, we must go beyond this simple description and allow for finite helium diffusivity χ . In order to simplify the analysis, we continue to neglect viscosity, and assume that

$$\chi \ll \eta . \tag{9.1}$$

We also assume for the moment that the magnetic field \mathbf{B}_i below the sublayer is

uniform and vertical. We may then equate the dimensional value of the vertical field strength to \mathbf{B} in the definition (8.19) of the Elsasser number Λ . We then have

$$\mathbf{B}_i = \Lambda^{\frac{1}{2}} \mathbf{e}_z. \quad (9.2)$$

We also make the boundary-layer approximation, $\nabla^2 \approx \partial^2 / \partial z^2$.

Allowing for finite χ values does not significantly alter the dynamics within the confinement layer, provided that the sublayer remains nearly flat and that $\chi \ll \eta$. Therefore the timescale of the flow within the sublayer is inherited from the confinement layer. In particular, the flow in the sublayer has the same strain rate as the confinement layer, U/δ_η . The thickness of the sublayer, δ_χ say, is determined by a balance between advection and diffusion of helium in (7.12). The strain rate U/δ_η must therefore match the helium diffusion rate χ/δ_χ^2 . Since $U/\delta_\eta = \eta/\delta_\eta^2$, it follows that

$$\delta_\chi/\delta_\eta \sim (\chi/\eta)^{1/2} \ll 1. \quad (9.3)$$

With realistic solar values for the tachocline diffusivities, we have $\chi/\eta \approx 0.02$ (see appendix A). The numerical solutions in chapter 10 confirm that this provides sufficient scale separation for the sublayer to be regarded as distinct from the confinement layer (see figure 7.2).

The magnetic diffusion rate η/δ_χ^2 in the sublayer greatly exceeds the helium diffusion rate χ/δ_χ^2 . The flow within the sublayer can therefore induce only a small departure $\mathbf{B} - \mathbf{B}_i = \mathbf{B}'$, say, from the interior field \mathbf{B}_i . In figures 7.2 and 7.4 the field lines are hardly deflected as they cross the sublayer. We therefore analyse the sublayer as a perturbation to the state with $\mathbf{u} = 0$ and $\mathbf{B} = \mathbf{B}_i$, and assume that the perturbation to \mathbf{B}_i is linear. Under these assumptions, equations (7.7)–(7.12)

become

$$\text{Ro} \frac{D\mathbf{u}}{Dt} + \mathbf{e}_z \times \mathbf{u} = -\nabla p + \alpha_T T \mathbf{e}_z - \alpha_\mu \mu \mathbf{e}_z + (\nabla \times \mathbf{B}') \times \mathbf{B}_i \quad (9.4)$$

$$0 = \nabla \cdot \mathbf{u} \quad (9.5)$$

$$\frac{\partial \mathbf{B}'}{\partial t} = \nabla \times (\mathbf{u} \times \mathbf{B}_i) + \frac{\partial^2 \mathbf{B}'}{\partial z^2} \quad (9.6)$$

$$0 = \nabla \cdot \mathbf{B}' \quad (9.7)$$

$$\frac{DT}{Dt} = \frac{\kappa}{\eta} \frac{\partial^2 T}{\partial z^2} \quad (9.8)$$

$$\frac{D\mu}{Dt} = \frac{\chi}{\eta} \frac{\partial^2 \mu}{\partial z^2} . \quad (9.9)$$

Since $\kappa \gg \chi$, the sublayer flow produces a negligible perturbation to the helium settling layer's uniform thermal stratification N_T . We may therefore assume that the thermal buoyancy force $\alpha_T T \mathbf{e}_z$ within the sublayer arises entirely from the uniform background thermal stratification. Since this force is curl-free, it can be incorporated into the pressure field, and will therefore be neglected for the remainder of this section.

On the timescale δ_η/U of the strain flow we may approximate magnetic diffusion across the sublayer as instantaneous, and therefore neglect the left-hand side of the induction equation (9.6). Substituting $\mathbf{B}_i = \Lambda^{\frac{1}{2}} \mathbf{e}_z$ into (9.6), we then find that

$$0 = \Lambda^{\frac{1}{2}} \frac{\partial \mathbf{u}}{\partial z} + \frac{\partial^2 \mathbf{B}'}{\partial z^2} . \quad (9.10)$$

Since both \mathbf{B}' and \mathbf{u} vanish beneath the sublayer, we can integrate (9.10) to give

$$0 = \Lambda^{\frac{1}{2}} \mathbf{u} + \frac{\partial \mathbf{B}'}{\partial z} . \quad (9.11)$$

Using (9.11), we can now write the Lorentz force in the momentum equation (9.4) as

$$(\nabla \times \mathbf{B}') \times \mathbf{B}_i = (\nabla \times \mathbf{B}') \times (\Lambda^{\frac{1}{2}} \mathbf{e}_z) \quad (9.12)$$

$$= -\Lambda^{\frac{1}{2}} \nabla B'_z + \Lambda^{\frac{1}{2}} \frac{\partial \mathbf{B}'}{\partial z} \quad (9.13)$$

$$= -\Lambda^{\frac{1}{2}} \nabla B'_z - \Lambda \mathbf{u} . \quad (9.14)$$

The term $-\Lambda^{\frac{1}{2}} \nabla B'_z$ is curl-free, and can therefore be incorporated into the pres-

sure force. The term $-\Lambda \mathbf{u}$ has the form of a Darcy or Rayleigh drag, showing that the sublayer behaves like a porous medium on the timescale set by the strain flow. The μ -choke together with the sublayer's flatness and thinness act to keep the flow nearly horizontal, compelling it to push past, and slightly deflect, the magnetic field lines spanning the sublayer. Similar behaviour occurs in Hartmann layers (e.g. [Debnath, 1973](#)), although in that case viscosity also contributes to the balance of forces.

Neglecting terms of order Ro , we obtain the following set of magnetostrophic equations for the sublayer flow:

$$\mathbf{e}_z \times \mathbf{u} = -\nabla p - \alpha_\mu \mu \mathbf{e}_z - \Lambda \mathbf{u} \quad (9.15)$$

$$0 = \nabla \cdot \mathbf{u} \quad (9.16)$$

$$\frac{D\mu}{Dt} = \frac{\chi}{\eta} \frac{\partial^2 \mu}{\partial z^2}. \quad (9.17)$$

A careful scaling analysis, presented in [Wood & McIntyre \(2010\)](#), confirms that equations (9.15)–(9.17) accurately describe the dynamics of the sublayer in a neighbourhood of the pole, even if the interior magnetic field is an axisymmetric dipole, rather than the uniform vertical field assumed here. The same method used to determine the “flatness” of the confinement layer in chapter 8 can now be applied to the sublayer. [Wood & McIntyre \(2010\)](#) showed that the tilting of the compositional stratification surfaces becomes dynamically significant at a dimensionless distance from the pole $\sim r_\mu$, where

$$r_\mu^2 = \alpha_\mu (\chi/\eta) \min(\Lambda, \Lambda^{-1}). \quad (9.18)$$

Comparing this with (8.20) we find

$$\begin{aligned} \frac{r_\mu}{r_T} &\sim \frac{N_\mu (\kappa \chi)^{1/2}}{N_T \eta} \\ &\approx 20, \end{aligned} \quad (9.19)$$

and so the sublayer is “even flatter” than the confinement layer, as was asserted in §7.5.

9.2 The subtail

Within the lower extremity of the sublayer, or “subtail”, the MMCs decay exponentially with depth as the μ -choke takes hold. Within this subtail, the helium settling layer suffers only small perturbations to its otherwise uniform compositional stratification, $\partial\mu/\partial z = -1$, and we may therefore perform a linear analysis similar to those in §4.2.1 and §4.2.2. We denote the perturbation to μ by μ' . In the steady state, equation (9.17) may then be approximated as

$$-u_z = \frac{\chi}{\eta} \frac{\partial^2 \mu'}{\partial z^2}. \quad (9.20)$$

We now take the curl and double-curl of (9.15), and apply (9.16), in order to obtain

$$-\frac{\partial \mathbf{u}}{\partial z} = \alpha_\mu \mathbf{e}_z \times \nabla \mu' - \Lambda \boldsymbol{\omega}, \quad (9.21)$$

$$-\frac{\partial \boldsymbol{\omega}}{\partial z} = \alpha_\mu \nabla^2 \mu' \mathbf{e}_z - \alpha_\mu \nabla \frac{\partial \mu'}{\partial z} + \Lambda \nabla^2 \mathbf{u}, \quad (9.22)$$

where $\boldsymbol{\omega} = \nabla \times \mathbf{u}$ is the vorticity. Taking the vertical components of (9.21) and (9.22), and making the boundary-layer approximation $\nabla^2 \approx \partial^2/\partial z^2$, we obtain

$$-\frac{\partial u_z}{\partial z} = -\Lambda \omega_z \quad (9.23)$$

$$-\frac{\partial \omega_z}{\partial z} = \alpha_\mu \nabla_H^2 \mu' + \Lambda \frac{\partial^2 u_z}{\partial z^2} \quad (9.24)$$

where $\nabla_H^2 = \nabla^2 - \partial^2/\partial z^2$ is the horizontal Laplacian. We can combine (9.23) and (9.24) with (9.20) to yield a single equation for the perturbation μ' ,

$$\alpha_\mu (\eta/\chi) \nabla_H^2 \mu' = (\Lambda + \Lambda^{-1}) \frac{\partial^4 \mu'}{\partial z^4}. \quad (9.25)$$

In dimensional variables, this equation is

$$\frac{N_\mu^2}{2\Omega_i \chi} \nabla_H^2 \mu' = (\Lambda + \Lambda^{-1}) \frac{\partial^4 \mu'}{\partial z^4}, \quad (9.26)$$

which is closely analogous to equation (4.9) in §4.2.2, once we identify $\nabla_H^2 = -1/L^2$. In §4.2.2, the horizontal scale L was determined by the global geometry

of the tachocline. Here, we expect the subtail to inherit the horizontal scale of the sublayer. Since (9.19) implies that the sublayer is even flatter than the confinement layer, the sublayer in turn inherits the horizontal scale of the confinement layer, $r_T \delta_\eta$. If we replace $\nabla_H^2 \rightarrow -1/(r_T \delta_\eta)^2$ in the dimensional subtail equation (9.26), and apply definitions (9.3) and (9.18), we obtain

$$\delta_x^4 \frac{\partial^4 \mu'}{\partial z^4} \approx -\frac{r_\mu^2}{r_T^2} \mu'. \quad (9.27)$$

Therefore the vertical scale of the subtail, δ_ℓ say, is smaller than the vertical scale of the bulk of the sublayer δ_χ , by a factor

$$\begin{aligned} \frac{\delta_\ell}{\delta_\chi} &= \left(\frac{r_T}{r_\mu} \right)^{1/2} \\ &\approx 0.2. \end{aligned} \quad (9.28)$$

In the sublayer analysis of §9.1 it was assumed that viscous forces are negligible. However, this approximation may break down within the subtail, if the length-scale δ_ℓ is sufficiently small. If we allow for finite viscosity, then equation (9.26) becomes

$$\frac{N_\mu^2}{2\Omega_i \chi} \left(\Lambda - \delta_{\text{Ek}}^2 \frac{\partial^2}{\partial z^2} \right) \nabla_H^2 \mu' = \left[1 + \left(\Lambda - \delta_{\text{Ek}}^2 \frac{\partial^2}{\partial z^2} \right)^2 \right] \frac{\partial^4 \mu'}{\partial z^4} \quad (9.29)$$

where $\delta_{\text{Ek}} = (\nu/2\Omega_i)^{1/2}$ is the Ekman lengthscale. So viscous effects are negligible within the subtail only if the Darcy friction from the magnetic field dominates the fluid viscosity, i.e. if

$$\Lambda \gg \delta_{\text{Ek}}^2 / \delta_\ell^2 \quad (9.30)$$

$$= \text{Ek} (r_\mu / r_T) (\eta / \chi) \quad (9.31)$$

$$\sim 10^{-6}. \quad (9.32)$$

This implies a lower bound on the vertical field strength B of approximately 10^{-4} gauss.

Chapter 10

The Numerical Model

10.1 Numerical complexity

Unfortunately it is not possible to solve the complete set of equations (7.7)–(7.12) analytically. To go beyond the perfectly flat analytical solutions described in §7.5 we must compute solutions numerically. One way to gauge the complexity of this task is to count the number of spatial and temporal derivatives in these equations. The order of the complete system can be determined by considering small-scale perturbations to an idealised background. In the absence of compositional stratification, such perturbations are governed by equations (C.20) and (C.21) of appendix C. In (C.21), the term with the highest number of derivatives is

$$\left(\frac{\partial}{\partial t} - \kappa \nabla^2\right) \left(\frac{\partial}{\partial t} - \nu \nabla^2\right)^2 \left(\frac{\partial}{\partial t} - \eta \nabla^2\right)^2 \nabla^2 \quad (10.1)$$

from which we deduce that the system is 12th order in space and 5th order in time. Allowing for compositional stratification introduces an additional factor of

$$\left(\frac{\partial}{\partial t} - \chi \nabla^2\right) \quad (10.2)$$

and so the system becomes 14th order in space and 6th order in time.

The large number of spatial derivatives relative to temporal derivatives arises from the presence of diffusion in each of the prognostic equations, which render

the equations “almost parabolic” on small spatial scales. However, the system remains partially elliptic because of the incompressibility constraint (7.8), which leads to the ∇^2 factor in (10.1). The system also supports hyperbolic behaviour, for example through Alfvén wave propagation.

From the discussions in chapters 8 and 9 it is clear that the confinement-layer flow incorporates a wide range of spatial and temporal scales. Resolving all of these scales in a numerical model is computationally demanding. Since we are primarily interested in steady states, it would be desirable to solve the steady-state equations directly, as in the model of Garaud & Garaud (2008). However, the numerical scheme employed by Garaud & Garaud is not guaranteed to converge to a solution when applied to a nonlinear system such as (7.7)–(7.12), and does not provide any information regarding the dynamical convergence towards the steady state (see §4.2.4).

An alternative approach is to neglect any terms in equations (7.7)–(7.12) that we expect to be small. In particular, we might choose to neglect the $O(\text{Ro})$ and $O(\text{Ek})$ terms in (7.7), thereby imposing magnetostrophic balance directly. However, this approach leads to pathological behaviour at small scales, for reasons discussed in appendix H.

Instead, we have chosen to solve the full set of time-dependent equations numerically. Although this is computationally demanding, we can be confident that the system will eventually converge to a steady state, provided that the confinement layer is dynamically stable. Timestepping the equations in a physically meaningful way also provides some insight into the dynamics of the confinement layer (§I.1).

Because of the computational complexity of the task, we have not attempted to solve the global tachocline problem. We consider only the high-latitude confinement layer illustrated in figure 7.2. Fitting the high-latitude confinement layer into a global tachocline model remains a challenge for the future, and will require the quantification of turbulent processes in the tachocline and convection zone. In particular, a global model would need to include realistic descriptions of magnetic flux pumping and turbulent magnetic diffusion in the bulk of the tachocline. Also crucial to the global picture is the turbulent gyroscopic pumping of polar

downwelling, and compensating upwelling in lower latitudes, together with the resulting global-scale pattern of heat flow and the feedback on N_T within the tachocline.

The numerical scheme employed is described briefly in the next section, with further technical details in appendix H. Several consistency tests have been performed on the numerical solutions, the results of which are set out in appendix I.

10.2 The numerical scheme

We have written a numerical code to solve the axisymmetric version of (7.7)–(7.12) in a cylinder of radius r_d , say. The computational domain is taken to be a rectangular grid in r and z , with regular grid intervals Δr and Δz , as illustrated in figure 10.1.

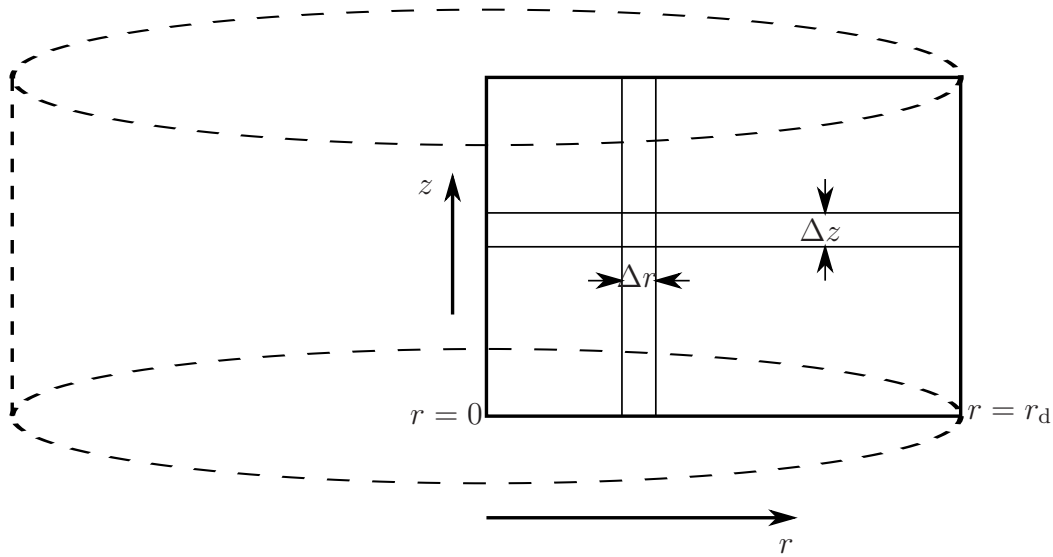


Figure 10.1: The computational domain used for numerical solution.

Since we are solving a local problem, we are required to specify boundary conditions (listed in §10.3). This inevitably involves artificial choices. In order to minimise the number of boundary conditions required by the numerical scheme, we have chosen to evaluate all spatial derivatives using low order finite differences. In particular, all first-order spatial derivatives are evaluated using two-point, one-

sided (first-order) finite differences, and all second-order spatial derivatives are evaluated using three-point, centred (first-order) finite differences. The directions of the one-sided finite differences are chosen to ensure numerical stability at the grid scale (further detail in appendix H). The prognostic equations are timestepped explicitly using a (first-order) Euler scheme. Since our primary interest is in the steady state, there would be no benefit from using a more accurate, higher-order timestepping scheme.

As explained in appendix H, the vertical grid interval Δz must be small enough to resolve the helium sublayer accurately, and the timestep Δt must be small enough to resolve thermal diffusion at this scale. In terms of the dimensionless units¹ defined in chapter 7, this imposes the following upper bound on the dimensionless timestep Δt :

$$\Delta t < \chi/\kappa. \quad (10.3)$$

We anticipate that the system will converge to a steady state on the timescale of magnetic diffusion across the confinement layer, which is order unity in the nondimensionalised system. The disparity between the diffusion rates of helium and temperature is therefore the principal factor determining the number of timesteps required for convergence to the steady state.

10.3 Boundary conditions

We impose a dipolar magnetic field structure underneath the confinement layer, with $B_r \propto r$, and a uniform downwelling of dimensional magnitude U from the field-free region aloft. In the example shown in figure 7.2 the numerical domain was defined by $0 \leq r \leq 5$, i.e. $r_d = 5$, and $-1 \leq z \leq 6$, one dimensionless unit taller than shown in the figure. We imposed $u_z = -1$ at $z = 6$ and $B_r/r = 1$ at $z = -1$. The imposed value of B_r/r determines the characteristic magnitude of the poloidal magnetic field components in the confinement layer, as can be seen from the analytical solutions of §7.5 (e.g. dashed curve in figure 7.3). This in turn determines the magnitude of the Elsasser number Λ defined by (8.19). In

¹We use dimensionless units for the remainder of this chapter, except where explicitly stated otherwise.

fact,

$$\Lambda \sim B_z^2 \tag{10.4}$$

$$\sim (B_r/r)^2. \tag{10.5}$$

From the analytical solutions of §7.5, we anticipate that the poloidal components of the magnetic field will decay with altitude like $\exp(-z)$ above the confinement layer. We therefore impose that $\partial B_z/\partial z = -B_z$ at $z = 6$, to simulate the presence of such an exponential tail in the region above the numerical domain. Since B_z is exponentially small at the top of the domain, we do not expect the precise choice of boundary condition there to significantly influence the steady state. This expectation is confirmed in appendix I. We also impose that $B_\phi = 0$ at $z = 6$, to ensure that the Maxwell stress over the top of the domain vanishes.

As shown in §7.5, the bulk of the confinement layer is relatively insensitive to conditions within the field-free region aloft, and in particular to the vertical shear $\partial u_\phi/\partial z$ aloft. In the numerical solutions, the vertical shear aloft is tied to the temperature distribution via the thermal-wind equation (7.18), and is therefore sensitive to the upper boundary condition for the temperature. This behaviour is not seen in the perfectly flat solutions derived in §7.5, because equation (7.18) becomes degenerate in the perfectly flat limit where $\alpha_T \rightarrow \infty$ and $\partial T/\partial r \rightarrow 0$.

The “true” upper boundary condition for temperature can only be determined by solving the global-scale heat flow problem, which is beyond the scope of the present study. For simplicity, we impose $T = \text{const.}$ and $\partial u_\phi/\partial z = 0$ at $z = 6$, which is consistent with equation (7.18) and the imposed uniform downwelling, and also ensures that no viscous torque is exerted on the top of the domain. Matching the confinement layer on to the observed negative vertical shear in the bulk of the tachocline is beyond the scope of this study, for reasons mentioned in §7.5 (but see discussions in Part IV).

At the periphery of the domain, the artificial cylindrical surface $r = r_d = 5$, the numerical algorithm requires us to specify the thermal and compositional stratification profiles $T(z)$ and $\mu(z)$, in a manner consistent with scalings in the confinement layer and helium sublayer (chapters 8 and 9). In this way we artificially fix the altitude of the helium sublayer, which in a global model would

be determined rather by the competition between the burrowing of MMCs and the diffusion of the interior field (see Part IV). The z -origin in our local, Boussinesq model is arbitrary, and has been chosen to coincide approximately with the altitude of the helium sublayer.

The peripheral $T(z)$ and $\mu(z)$ profiles strongly influence the velocity field, which is tightly linked to the two stratifications by equations (7.11) and (7.12). In the limit of infinitely strong stratification described in §7.5, equations (7.11) and (7.12) reduce to (7.21), and so $T(z)$ and $\mu(z)$ can no longer be specified independently. In §7.5, $T(z)$ and $\mu(z)$ were both determined by (7.21), up to boundary conditions, as soon as $u_z(z)$ was specified. The $T(z)$ and $\mu(z)$ profiles obtained in this manner can be used as peripheral boundary conditions for the numerical solutions.

In addition to $T(z)$ and $\mu(z)$, the numerical solutions require a third vertical profile to be specified at the periphery. An obvious choice is the vertical profile of Maxwell stress, $B_r B_\phi$, which represents the field lines' connection to lower latitudes and the Alfvénic torque exerted therefrom. As discussed in §7.3, we expect the Maxwell stress over the periphery to be prograde within the confinement layer, and to vanish both above and below the confinement layer. However, in practice, we found it more convenient to specify $B_\phi(z)$ at the periphery, since B_ϕ decays less rapidly with height above the confinement layer than does the Maxwell stress, and is therefore less susceptible to numerical truncation errors.

The freedom to specify $B_\phi(z)$ is also present in the analytical framework of §7.5, but was given up in order to ensure the vanishing of the Alfvénic torque as $z \rightarrow -\infty$. This condition uniquely determined $B_\phi(z)$ via the expression (7.29). Also allowed by the analytical framework is the freedom to specify $u_\phi(z)$, which we similarly gave up in order to ensure solid rotation as $z \rightarrow -\infty$, thus determining $u_\phi(z)$ via (7.31).

Within the analytical framework both u_ϕ and B_ϕ can be determined from their values at any single location on each magnetic field line. This is because of the Alfvénic coupling along the field lines, expressed by the $\mathbf{B} \cdot \nabla$ operator in equations (7.22) and (7.24). There is slightly less freedom within the numerical framework. The time-dependence, in the equations solved numerically, replaces

static Alfvénic coupling by Alfvénic wave propagation, requiring a single boundary condition at either end of each field line. This is analogous to the need for a single boundary condition at either end of an elastic string in motion. Having already chosen to specify $B_\phi(z)$ at the periphery $r = 5$ we must therefore specify $u_\phi(r)$ at the bottom of the domain, i.e. at $z = -1$. Alternatively, we could choose to specify $B_\phi(r)$ at $z = -1$ and $u_\phi(z)$ at $r = 5$. Although both choices are mathematically valid, we found it more convenient to specify $B_\phi(z)$ at the periphery, for reasons discussed in §10.4.

At $z = -1$ we impose $u_\phi = 0$, i.e. that the interior is in solid rotation, as expected from the global picture. However, care must be taken to ensure that an Ekman layer does not form at the bottom of the domain. Uniform rotation must therefore be imposed indirectly, via the azimuthal component of the induction equation (7.9), rather than via the azimuthal component of the momentum equation (7.7). As shown in appendix D, any discontinuity in $\partial B_\phi/\partial z$ over a horizontal surface must be balanced by a discontinuity in u_ϕ . More precisely,

$$-\left[\frac{\partial B_\phi}{\partial z}\right] = B_z [u_\phi] \quad (10.6)$$

in dimensionless units (cf. equation (D.8)) where square brackets indicate a discontinuity. By imposing a discontinuity in $\partial B_\phi/\partial z$ across the lower boundary of the numerical domain, with amplitude equal to the value of $B_z u_\phi$ immediately *below* the lower boundary, we thereby ensure that u_ϕ vanishes immediately *above* the lower boundary. Using $+/-$ to denote conditions above/below the boundary $z = -1$, this boundary condition can be expressed as

$$\left[\frac{\partial B_\phi}{\partial z}\right]_-^+ = B_z u_\phi|_- . \quad (10.7)$$

As the system converges to a steady state, we expect u_ϕ to converge to zero below $z = -1$, so that the discontinuity in $\partial B_\phi/\partial z$ vanishes. Indeed, in appendix D we show that such a discontinuity can be maintained only by a discontinuity in T (or μ), which is ruled out by the presence of temperature and helium diffusion.

At $z = -1$, we further impose the conditions (7.3) and (7.4), equivalently $\partial T/\partial z = 1$ and $\partial \mu/\partial z = -1$. We also impose $u_z = 0$, i.e. that there is no meridional flow

pendix H, in which artificial horizontal diffusivities ν_H , χ_H are introduced in order to maintain numerical stability. However, from the scale analyses outlined in chapters 8 and 9 we may identify the conditions most essential for achieving a qualitatively similar parameter regime — that is, qualitatively similar to a regime with a perfect parameter match to the real Sun. These essential conditions are:

1. The Rossby number Ro should be small in comparison with unity, so that the steady state is close to magnetostrophic.
2. The thermal diffusivity κ should be large in comparison with the magnetic diffusivity η , so that the confinement-layer flow only weakly perturbs the background thermal stratification.
3. The confinement layer and helium sublayer should both be reasonably flat, at least within the numerical domain $r \leq r_d$. With (9.19) in mind, we also take $r_\mu > r_T$, where $r_T > r_d > 1$.
4. The helium diffusivity χ should be small in comparison with the magnetic diffusivity η , so that the helium sublayer is thinner than, and therefore distinct from, the magnetic confinement layer.
5. The viscosity ν should be small enough that viscous effects are negligible throughout the confinement layer and sublayer. This condition implies a lower bound on Λ , given by (9.31), or equivalently an upper bound on Ek .

Leaving ν_H and χ_H aside for the moment (see Appendix H) we can characterise the system by seven dimensionless parameters, including the Elsasser number Λ , which enters through the boundary condition for B_r at $z = -1$, as described in §10.3. Table 10.1 presents the other six dimensionless parameters, with nominal solar values alongside the values used in the numerical solution presented in figure 7.2 (and also in figures 10.3, 10.4 and 10.5).² The last column echoes aspects of the qualitative parameter conditions just stated. The nominal solar values are based on the parameter values quoted in appendix A, and also assume $U = 10^{-5} \text{ cm s}^{-1}$.

²In figures 7.2 and 10.3 the uppermost part of the numerical domain, $5 \leq z \leq 6$, is not shown.

Table 10.1: Parameter values and conditions; see text.

Dim'less parameter	Nominal solar value	Value for num. sol'n	Condition
Ro	5×10^{-8}	10^{-2}	$\ll 1$
κ/η	3×10^4	10^2	$\gg 1$
$\alpha_T(\eta/\kappa)$	2×10^7	50	$> \max(\Lambda, \Lambda^{-1})^a$
$(r_\mu/r_T)^2$	3×10^2	2	> 1
χ/η	2×10^{-2}	2×10^{-2}	$\ll 1$
Ek	3×10^{-9}	2×10^{-4}	$\ll \Lambda(r_T/r_\mu)(\chi/\eta)$

^a This condition follows from $r_T > 1$, with r_T defined by (8.20).

Figure 10.3 shows plots of the steady-state streamlines and magnetic field lines from the numerical solution whose parameter values are listed in table 10.1, and whose meridional cross-section was presented in figure 7.2. Figure 10.4 shows the vertical profiles of u_z , u_r/r , u_ϕ/r , B_z , B_r/r and B_ϕ/r on the rotation axis, from the same numerical solution.

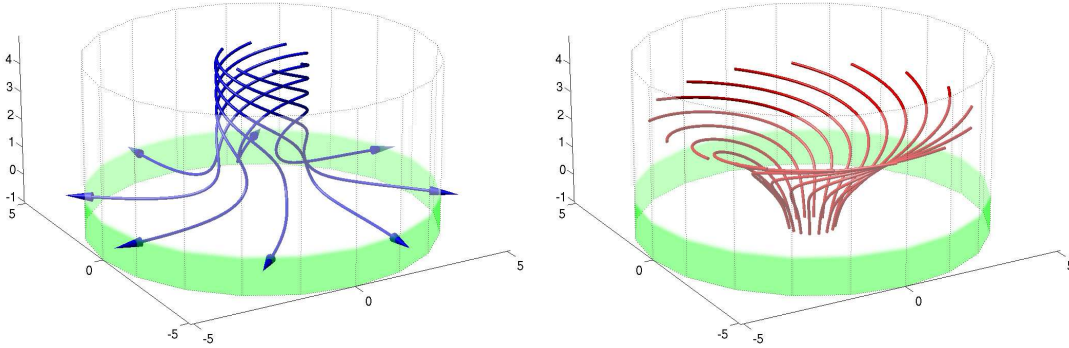


Figure 10.3: A numerical solution of the confinement-layer equations with $r_T^2 \approx 14$ and Elsasser number $\Lambda \approx 3.5$. Other parameter values are given in the second-last column of Table 10.1. From the same solution as shown in figure 7.2.

From figure 10.4 we see that $\Lambda = B_{iz}^2|_{z=0} \approx 3.5$. The nominal range of Λ for which solutions are nearly flat within dimensionless radius r is determined by (8.20) with $r_T > r$. With the parameter values in the second-last column of Table 10.1, $r_T > r$ is equivalent to

$$\max(\Lambda, \Lambda^{-1}) < 50/r^2. \quad (10.8)$$

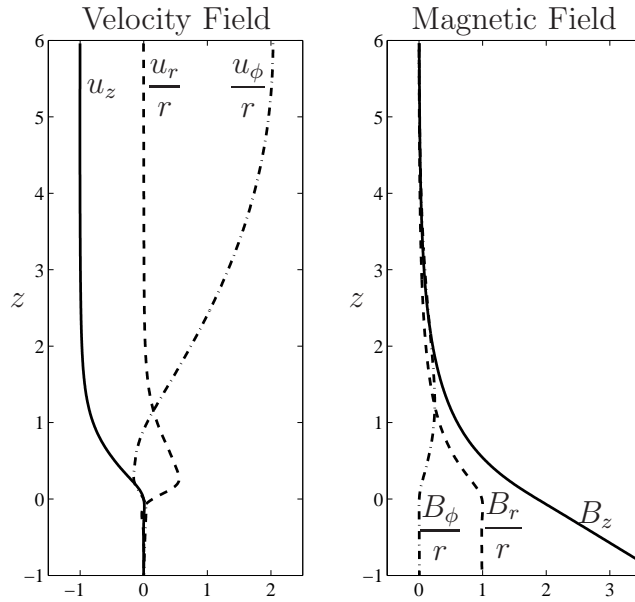


Figure 10.4: Vertical profiles from a numerical solution of the confinement-layer equations with $r_T^2 \approx 14$ and Elsasser number $\Lambda \approx 3.5$. Other parameter values are given in the second-last column of Table 10.1. From the same solution as shown in figure 7.2.

Since $\Lambda \approx 3.5$, (10.8) is violated near the edge of the domain, $r = r_d = 5$. Nevertheless, as seen for instance in figure 7.2, the solution remains fairly close to being flat. This shows that the confinement-layer structure is robust even at colatitudes for which the analysis of §7.5 breaks down.

The numerical solutions confirm that the confinement layer and helium sublayer are magnetostrophically balanced (see plots in §1.2). However, magnetostrophic balance holds less robustly in the upper part of the domain. In this upper region the Coriolis and Lorentz forces are exponentially small, and the effects of small but finite Ro and Ek are therefore relatively more significant. This leads to difficulties when comparing the numerical solutions directly with the analytical solutions of §7.5, as will be described in §10.5.

For the numerical solution shown in figures 7.2, 10.3 and 10.4, the vertical profiles of T , μ and B_ϕ at $r = 5$ were initially taken from an analytical solution of the kind described in §7.5. The resulting steady-state meridional flow, and the Coriolis torque it exerts on each field line, cannot be precisely known in advance. So the steady state found, with this choice of B_ϕ , will generally include a non-zero profile of Alfvénic torque exerted at the bottom of the computational domain,

$z = -1$. This is inconsistent with the picture presented in figure 7.1, in which \mathbf{B}_i is dipolar and no Alfvénic torque is exerted on the top of the helium settling layer. We therefore make iterative adjustments to the $B_\phi(z)$ profile at $r = 5$, aiming to make the Alfvénic torque at $z = -1$ vanish in the steady state.

It was found that making small changes in the peripheral $B_\phi(z)$ profile typically leads to a new steady state in which the meridional velocity within the confinement layer is essentially unchanged. Therefore the steady-state poloidal magnetic field is also essentially unchanged. Since the numerical solutions are very nearly magnetostrophic, this observation suggests a simple algorithm for determining the required adjustment to $B_\phi(z)$. Equation (7.16) implies that any change in rB_ϕ at $r = 5$ is transmitted to the bottom of the domain along the poloidal field lines. This is the same “static Alfvénic coupling” described in §10.3. So the required adjustment to $B_\phi(z)$ at $r = 5$ can be determined directly from the steady-state $B_\phi(r)$ profile at $z = -1$.

In practice, slight departures from magnetostrophic balance mean that this adjustment procedure never works perfectly at the first attempt, but nonetheless the Alfvénic torque at the bottom of the domain generally decreases with each successive adjustment to $B_\phi(z)$, and after several such adjustments is close to zero. In figure 10.5 we display the steady-state profile of rB_ϕ in a vertical cross-section through the same solution shown in figure 7.2. Figure 10.5 also displays some of the poloidal field lines in the confinement layer. It is apparent that the Alfvénic torque on the bottom of the domain is close to zero, and that rB_ϕ is roughly constant along each magnetic field line in the region below the helium sublayer, where the left-hand side of (7.16) vanishes.

10.5 Upper-domain “slipperiness”

On the rotation axis, where the profiles in figure 10.4 were taken, the stratification surfaces are flat for any finite α_T and α_μ . If the solution were in perfect magnetostrophic balance then we could use its $u_z(z)$ profile to calculate the other field components on the axis by the procedure for constructing perfectly flat solutions described in §7.5. But, as described above, the numerical solutions are

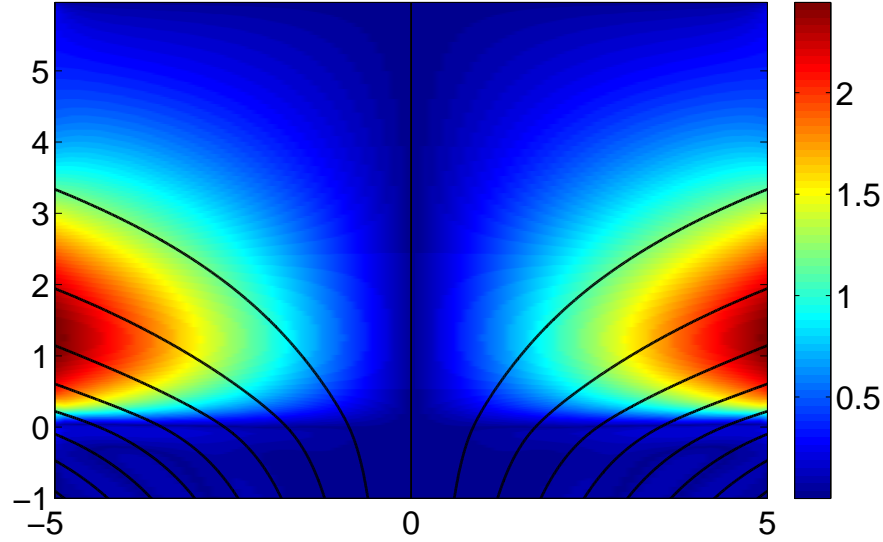


Figure 10.5: The steady-state profile of $\sqrt{|rB_\phi|}$ in a vertical cross-section through the same numerical solution shown in figure 7.2. Poloidal magnetic field lines are shown in black.

generally not in perfect balance, especially toward the upper part of the domain. In particular, the numerical $u_z(z)$ will generally not conform to the decay law (7.30) as z increases. So the perfectly flat solution obtained by this process cannot precisely match the numerical solution, even on the axis. Indeed, such a perfectly flat solution will often exhibit wild deviations from the numerical solution toward the upper part of the domain. There, the delicate balance of terms gives the dynamics a certain “slipperiness”, as already evidenced by the upper-domain sensitivity to values of the decay constant γ in (7.30).

To enable a meaningful comparison between the numerical and analytical solutions, we are therefore compelled to make small adjustments to $u_z(z)$ in the upper domain, to make it conform to (7.30), before using it to compute a perfectly flat solution. In the case shown here the required adjustment to $u_z(z)$ is very small indeed. The solid u_z curves on the left of figures 7.3 and 10.4 are practically indistinguishable.

Part IV

Conclusions

Chapter 11

Discussion

The confinement-layer solutions described in Part III represent the first self-consistent model of magnetic confinement and angular momentum balance in the high-latitude tachocline. However, in order to formulate a complete tachocline theory, we must describe how the high-latitude confinement layer fits into the global picture suggested by figure 7.1.

Figure 11.1 sketches the way in which the confinement layer might fit into its surroundings near the bottom of the polar tachocline (cf. figure 7.2). At the periphery of the polar downwelling region, the field lines (solid) emerge from the confinement layer on their way to lower latitudes. They will tend to splay out and slant upward as they exit the downwelling region. The extra-polar tachocline is therefore characterised by stronger magnetic fields with greater vertical lengthscales. The magnetic Reynolds number, which is of order unity in the confinement layer, increases with colatitude, and the equatorward MMC at the base of the tachocline begins to slant upward, flowing approximately along the field lines.

At even greater colatitudes, the field lines continue to rise through the tachocline until they encounter the convection zone's overshoot layer, where they are held horizontal by turbulent magnetic flux pumping. On the way we must expect turbulent eddy fluxes to become increasingly important, decoupling the MMC's upwelling streamlines from the time-averaged field lines, and also limiting the winding-up of the field lines by the tachocline's latitudinal shear (see figure 7.1).

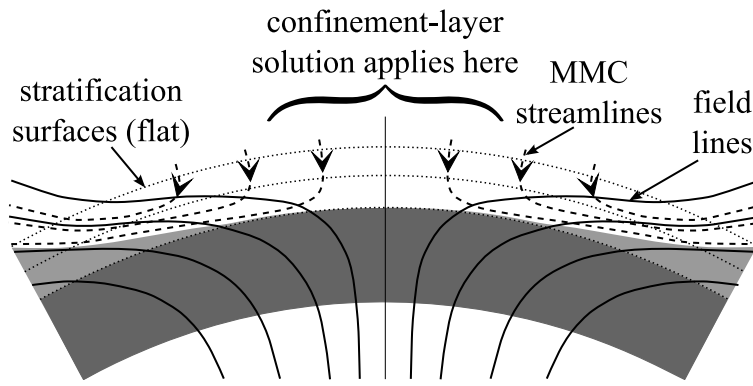


Figure 11.1: Sketch of the magnetic confinement layer and its immediate surroundings at the bottom of the high-latitude tachocline. Close to the pole the interior magnetic field (solid lines) is confined by the downwelling MMC (dashed streamlines). The vertical scale has been greatly exaggerated.

At all latitudes the stratification surfaces (shown dotted in figure 11.1) remain nearly flat. However, the region ventilated by the MMC (unshaded in figure 11.1) is deepest at the poles, in a manner reminiscent of the “polar pits” mentioned in chapter 4. In today’s Sun, the ventilated region extends down only as far as the top of the helium settling layer, indicated by dark shading. But in the early Sun, before the formation of the settling layer, the tachocline’s MMCs might well have burrowed much deeper into the radiative envelope (Wood & McIntyre, 2010). During the early main sequence, when the Sun rotated more rapidly, the burrowing tendency would have been stronger (§2.4),¹ and the polar pits might perhaps have been many tens of megametres deep. Ventilation to greater depths during the first gigayear or so of the Sun’s main-sequence evolution might prove to be the long-sought explanation for the Sun’s observed lithium and beryllium abundances (chapter 6).

The depth to which the MMCs burrow into the radiative envelope is determined by the structure of the internal field \mathbf{B}_i as well as by the strength of the gyroscopic pumping in the layers above. In our local model of the high-latitude confinement layer these factors are fixed by the boundary conditions, and so we cannot quantitatively predict the depth of ventilation below the convection zone. But if this ventilation is the dominant mechanism for solar lithium depletion, then the polar pits would need to extend approximately $0.1R_\odot$ into the radiative envelope

¹The interior field \mathbf{B}_i also would have been stronger, but probably by only a modest fraction, since the global-scale magnetic diffusion time is longer than the Sun’s present age.

(see chapter 6 and further discussion in chapter 12).

The global tachocline model that would be needed to test, and to begin to quantify, the foregoing speculations would have to describe

1. the precise way in which turbulent stresses in the convection zone and tachocline gyroscopically pump the polar downwelling responsible for confining \mathbf{B}_i ;
2. the global-scale distribution of temperature and heat flow that fits in with these MMCs;
3. the turbulent magnetic flux pumping by convective overshoot that we assume confines \mathbf{B}_i in extra-polar latitudes;
4. the extent to which the winding-up of the time-averaged toroidal field in extra-polar latitudes (figure 7.1) is limited by turbulent eddy fluxes;
5. the reaction of the overlying turbulent layers to all of the above, especially the deficit in the convection zone's differential rotation governing the torques exerted from above, whether via gyroscopically-pumped MMCs or via turbulent stresses in the bulk of the tachocline, or via both.

Progress on these formidable problems will of course depend on finding suitable ways to model the turbulent processes. In chapter 12 we suggest ways in which the high-latitude model presented in Part III could be extended to incorporate some of the processes described above.

Chapter 12

Future Work

12.1 Gyroscopic pumping

In the confinement-layer model presented in Part [III](#), the downwelling required to confine \mathbf{B}_i is imposed as an upper boundary condition. As described in [§4.2.3](#), downwelling in the high-latitude tachocline is driven by gyroscopic pumping in the layers above, and is therefore closely connected to the vertical shear in those layers. The case of gyroscopic pumping by a Tayler–Spruit dynamo ([Spruit, 2002](#)) was described by [McIntyre \(2007\)](#), whose arguments are summarised in [appendix G](#). If the angular momentum transport produced by the dynamo is parametrised as a turbulent viscosity ν_T , then the vertical component of the MMC driven in high-latitudes is

$$u_z = \nu_T \frac{d \ln \Omega}{dz} \quad (12.1)$$

where Ω is the absolute angular velocity and z is the vertical coordinate.

By introducing a turbulent viscosity into the upper layers of our confinement-layer model, it should be possible to incorporate gyroscopic pumping directly, rather than as a boundary condition. In order to drive downwelling, the angular velocity Ω must decrease with altitude in the upper part of the domain. In the numerical solution presented in [chapter 10](#), constant temperature was imposed at the top of the domain, and so the angular velocity has no vertical variation

aloft (see §10.3). With more general temperature boundary conditions it should be possible to obtain solutions with negative shear aloft, as is observed in the high-latitude tachocline. The analysis in §7.5 suggests that the structure of the confinement layer will not be strongly affected by the presence of vertical shear and turbulent viscosity in the layers above.

12.2 Lithium burning

To verify the picture suggested in figure 11.1 we need to extend our confinement-layer model horizontally, beyond the polar downwelling region. However, to determine whether the ventilated polar pits can extend deep enough to burn lithium, we will need to construct a global model of magnetic field confinement, perhaps similar to that of [Garaud & Garaud \(2008, see §4.2.4\)](#). The analysis performed in chapter 8 might allow us to develop their model to achieve field confinement in the polar regions.

If the polar pits can be shown to extend deep enough to burn lithium, we must then address how long they can persist, before being choked off by the formation of the helium settling layer. Incorporating compositional stratification into global tachocline models is problematic because of the tiny diffusivities involved, but some insight might be gained from our local high-latitude model. By varying the degree of compositional stratification in our numerical solutions, we hope to describe in detail the formation of the helium sublayer, and the onset of the μ -choke.

Part V

Appendices

Appendix A

Parameter Values

Table A.1: Tachocline parameters at $0.7R_{\odot}$, and global solar parameters. All values are taken from [Gough \(2007\)](#) except N_{μ} , which is taken from [McIntyre \(2007, see chapter 5\)](#).

density	ρ	0.21	g cm^{-3}
pressure	p	6.7×10^{13}	$\text{g cm}^{-1}\text{s}^{-2}$
temperature	T	2.3×10^6	K
sound speed	c	2.3×10^7	cm s^{-1}
gravitational acceleration	g	5.4×10^4	cm s^{-2}
density scale height	H_{ρ}	$0.12R_{\odot}$	
pressure scale height	H_p	$0.08R_{\odot}$	
pressure Soret factor	k_p	2.9	
temperature Soret factor	k_T	2.6	
adiabatic index	γ	1.665	
thermal buoyancy frequency	N_T	8×10^{-4}	s^{-1}
compositional buoyancy frequency	N_{μ}	5×10^{-4}	s^{-1}
total buoyancy frequency	N	9×10^{-4}	s^{-1}
magnetic diffusivity	η	4.1×10^2	cm^2s^{-1}
kinematic viscosity	ν	2.7×10^1	cm^2s^{-1}
thermal diffusivity	κ	1.4×10^7	cm^2s^{-1}
helium diffusivity	χ	8.7	cm^2s^{-1}
total solar mass	M_{\odot}	1.99×10^{33}	g
total solar radius	R_{\odot}	6.96×10^{10}	cm
interior angular velocity	Ω_i	2.7×10^{-6}	s^{-1}

Appendix B

Meridional Circulation

Mean meridional circulations (MMCs) arise naturally in rotating fluids that are driven away from uniform rotation. As a simple example, we consider here an incompressible fluid in approximately uniform rotation with angular velocity $\mathbf{\Omega}$. In the frame rotating with the fluid, the momentum equation is then

$$\frac{D\mathbf{u}}{Dt} + 2\mathbf{\Omega} \times \mathbf{u} = -\frac{1}{\rho}\mathbf{\nabla}p + \mathbf{g} + \nu\nabla^2\mathbf{u}, \quad (\text{B.1})$$

where D/Dt is the Lagrangian or material derivative. We define the operator $\langle.\rangle$ as an average over time and longitude, and use it to decompose the velocity and pressure fields \mathbf{u} and p into steady, axisymmetric and fluctuating, non-axisymmetric parts: $\mathbf{u} = \langle\mathbf{u}\rangle + \mathbf{u}'$ and $p = \langle p\rangle + p'$. By taking the average of the momentum equation (B.1) we obtain the following equation for $\langle\mathbf{u}\rangle$:

$$\langle\mathbf{u}\rangle \cdot \mathbf{\nabla} \langle\mathbf{u}\rangle + 2\mathbf{\Omega} \times \langle\mathbf{u}\rangle = -\frac{1}{\rho}\mathbf{\nabla} \langle p\rangle + \mathbf{g} + \nu \langle \nabla^2 \mathbf{u} \rangle - \langle \mathbf{u}' \cdot \mathbf{\nabla} \mathbf{u}' \rangle. \quad (\text{B.2})$$

The final two terms on the right-hand side incorporate all the angular momentum transport processes, including hydrodynamic turbulence and wave breaking, that can act to drive the system away from uniform rotation. To properly describe these processes would require solving the complete set of nonlinear, three-dimensional fluid equations. Here, we instead adopt a crude parametrisation, replacing these two terms with a “generalised Rayleigh friction” that forces the fluid towards a state of differential rotation. Using cylindrical polar coordinates

(r, z, ϕ) aligned with the rotation axis, we write this “anti-frictional” force¹ as $\alpha(\tilde{u}_\phi - \langle u_\phi \rangle) \mathbf{e}_\phi$, where $\langle u_\phi \rangle$ is the averaged azimuthal velocity in the rotating frame, and \tilde{u}_ϕ is the steady, axisymmetric differential rotation that the system is forced towards. The parameter α is a relaxation rate, which quantifies how strongly the system is driven away from uniform rotation, and might be interpreted physically in terms of the turnover rate of the local convective eddies. Provided that the forcing produces only small departures from uniform rotation (i.e. $\tilde{u}_\phi/r \ll |\boldsymbol{\Omega}|$) and is not too strong ($\alpha \lesssim |\boldsymbol{\Omega}|$) we may neglect the nonlinear term on the left-hand side of B.2. We then have

$$2\boldsymbol{\Omega} \times \langle \mathbf{u} \rangle = -\frac{1}{\rho} \boldsymbol{\nabla} \langle p \rangle + \mathbf{g} + \alpha(\tilde{u}_\phi - \langle u_\phi \rangle) \mathbf{e}_\phi. \quad (\text{B.3})$$

The azimuthal components of (B.3) and its curl are

$$2|\boldsymbol{\Omega}| \langle u_r \rangle = \alpha(\tilde{u}_\phi - \langle u_\phi \rangle), \quad (\text{B.4})$$

$$2|\boldsymbol{\Omega}| \frac{\partial}{\partial z} \langle u_\phi \rangle = 0. \quad (\text{B.5})$$

Equation (B.5) is an explicit demonstration of the Taylor–Proudman theorem, and equation (B.4), taken together with boundary conditions, describes the gyroscopic pumping of the meridional circulation. For example, if the domain is bounded by axisymmetric impermeable surfaces $z = z_1(r)$ and $z = z_2(r)$ then mass conservation implies that $\int_{z_1}^{z_2} dz \langle u_r \rangle = 0$ for all r . Hence, by integrating (B.4) between $z = z_1$ and $z = z_2$, we find that

$$\int_{z_1}^{z_2} dz (\tilde{u}_\phi - \langle u_\phi \rangle) = 0 \quad (\text{B.6})$$

$$\Rightarrow \langle u_\phi \rangle = \frac{\int_{z_1}^{z_2} dz \tilde{u}_\phi}{z_2 - z_1} \quad (\text{B.7})$$

i.e. $\langle u_\phi \rangle$ is the axial average of \tilde{u}_ϕ .

So the anti-frictional forcing produces only as much differential rotation as is permitted by the Taylor–Proudman theorem. The residual forcing serves to drive the meridional circulation. The only effect of increasing the strength of the forcing (i.e. increasing α) is to drive a faster circulation.

¹We adopt here a similar parametrisation to that of [Garaud & Acevedo Arreguin \(2009\)](#), except that here the forcing acts only in the azimuthal direction.

As an illustrative example, we now apply these results to the case of a spherical shell with the same aspect ratio as the Sun’s convection zone. We choose \tilde{u}_ϕ to mimic the observed pattern of differential rotation. Since the results do not depend sensitively on the precise form of \tilde{u}_ϕ we adopt a simple “hyperbolic” approximation for the solar angular velocity contours:

$$\tilde{u}_\phi/r = (ar)^2 - (bz)^2 \quad (\text{B.8})$$

where a and b are constants. In Figure B.1 we show \tilde{u}_ϕ/r for a particular choice of a and b , together with the resulting profile of $\langle u_\phi/r \rangle$. Streamlines of the meridional flow are shown in Figure B.2; the shape of the streamlines is independent of both a and b .

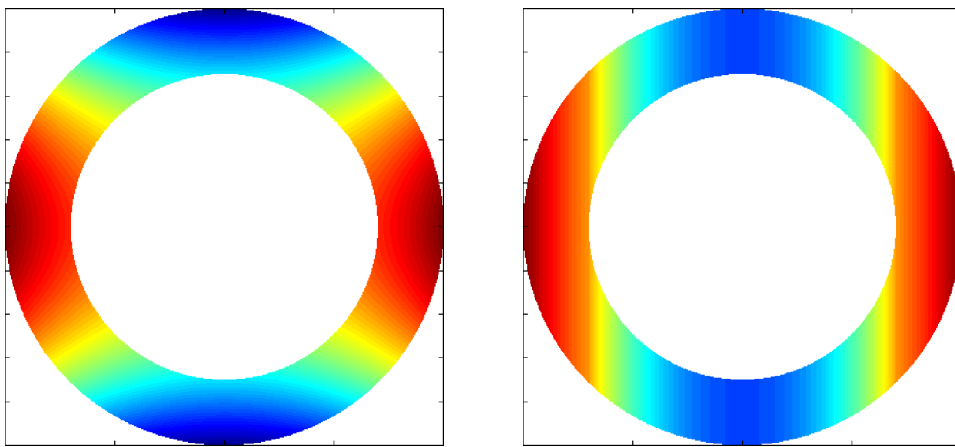


Figure B.1: Left panel: the differential rotation \tilde{u}_ϕ/r , chosen to approximate the rotation of the convection zone. Right panel: the differential rotation $\langle u_\phi/r \rangle$ in our model.

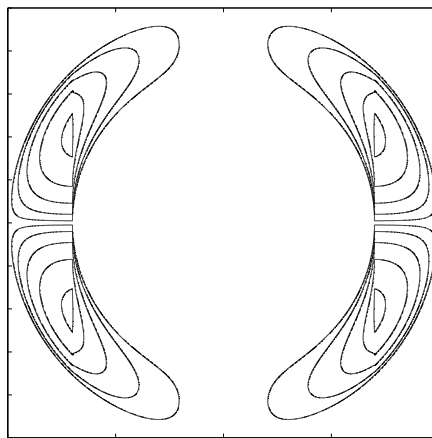


Figure B.2: Streamlines of the meridional flow in our model.

Appendix C

MAC Waves

We consider perturbations to a Boussinesq, magnetised fluid, with uniform gravitational acceleration \mathbf{g} . We suppose that the unperturbed flow is uniform rotation with angular velocity $\mathbf{\Omega}$, and adopt a frame of reference in which the fluid is at rest. We further assume uniform thermal stratification and an unperturbed background magnetic field of the form

$$\mathbf{B} = \mathbf{B}_0 + \frac{1}{2}\mathbf{J}_0 \times \mathbf{x}, \quad (\text{C.1})$$

where the vectors \mathbf{B}_0 and \mathbf{J}_0 are both uniform. Using primes to denote the perturbations, the governing equations can be written in the form

$$\begin{aligned} \left(\frac{D}{Dt} - \nu \nabla^2\right)\boldsymbol{\omega}' + \frac{1}{2}\mathbf{J}_0 \times \mathbf{J}' &= (2\mathbf{\Omega} + \boldsymbol{\omega}') \cdot \nabla \mathbf{u}' + (\mathbf{B} + \mathbf{B}') \cdot \nabla \mathbf{J}' \\ &\quad - (\mathbf{J}_0 + \mathbf{J}') \cdot \nabla \mathbf{B}' + \mathbf{g} \times \nabla T' \end{aligned} \quad (\text{C.2})$$

$$\nabla \cdot \mathbf{u}' = 0 \quad (\text{C.3})$$

$$\left(\frac{D}{Dt} - \eta \nabla^2\right)\mathbf{B}' + \frac{1}{2}\mathbf{J}_0 \times \mathbf{u}' = (\mathbf{B} + \mathbf{B}') \cdot \nabla \mathbf{u}' \quad (\text{C.4})$$

$$\nabla \cdot \mathbf{B}' = 0 \quad (\text{C.5})$$

$$\left(\frac{D}{Dt} - \kappa \nabla^2\right)T' = \frac{N^2}{|\mathbf{g}|^2} \mathbf{g} \cdot \mathbf{u}' \quad (\text{C.6})$$

where $\boldsymbol{\omega}' = \nabla \times \mathbf{u}'$ is the vorticity, $\mathbf{J}' = \nabla \times \mathbf{B}'$ is the electric current in suitable units and T' represents fractional perturbations to the background temperature

profile. The terms involving \mathbf{J}_0 on the left-hand sides of (C.2) and (C.4) arise from the curvature of the background magnetic field \mathbf{B} . The operator

$$\frac{D}{Dt} = \frac{\partial}{\partial t} + \mathbf{u}' \cdot \nabla \quad (\text{C.7})$$

is the material derivative.

If the perturbations are sufficiently small then they can be described by the linearised versions of (C.2), (C.4) and (C.6), which are

$$\begin{aligned} \left(\frac{\partial}{\partial t} - \nu \nabla^2\right) \boldsymbol{\omega}' + \frac{1}{2} \mathbf{J}_0 \times \mathbf{J}' &= (2\boldsymbol{\Omega} \cdot \nabla) \mathbf{u}' + (\mathbf{B} \cdot \nabla) \mathbf{J}' \\ &\quad - (\mathbf{J}_0 \cdot \nabla) \mathbf{B}' + \mathbf{g} \times \nabla T' \end{aligned} \quad (\text{C.8})$$

$$\left(\frac{\partial}{\partial t} - \eta \nabla^2\right) \mathbf{B}' + \frac{1}{2} \mathbf{J}_0 \times \mathbf{u}' = (\mathbf{B} \cdot \nabla) \mathbf{u}' \quad (\text{C.9})$$

$$\left(\frac{\partial}{\partial t} - \kappa \nabla^2\right) T' = \frac{N^2}{|\mathbf{g}|^2} \mathbf{g} \cdot \mathbf{u}'. \quad (\text{C.10})$$

It proves useful to also consider the curls of (C.8) and (C.9), which are

$$\begin{aligned} -\left(\frac{\partial}{\partial t} - \nu \nabla^2\right) \nabla^2 \mathbf{u}' - \frac{1}{2} \mathbf{J}_0 \times \nabla^2 \mathbf{B}' &= (2\boldsymbol{\Omega} \cdot \nabla) \boldsymbol{\omega}' - (\mathbf{B} \cdot \nabla) \nabla^2 \mathbf{B}' - (\mathbf{J}_0 \cdot \nabla) \mathbf{J}' \\ &\quad + \mathbf{g} \nabla^2 T' - \mathbf{g} \cdot \nabla \nabla T' \end{aligned} \quad (\text{C.11})$$

$$\left(\frac{\partial}{\partial t} - \eta \nabla^2\right) \mathbf{J}' + \frac{1}{2} \mathbf{J}_0 \times \boldsymbol{\omega}' = (\mathbf{B} \cdot \nabla) \boldsymbol{\omega}'. \quad (\text{C.12})$$

In the particular case where \mathbf{J}_0 and $\boldsymbol{\Omega}$ are both aligned with \mathbf{g} , the solutions of the linearised equations are remarkably simple. Defining u'_g , ω'_g , B'_g and J'_g as the “downward” components of \mathbf{u}' , $\boldsymbol{\omega}'$, \mathbf{B}' and \mathbf{J}' (i.e. the components in the direction of \mathbf{g}) we then need consider only the downward components of our linear

equations, which are

$$\left(\frac{\partial}{\partial t} - \nu \nabla^2\right) \omega'_g = (2\mathbf{\Omega} \cdot \nabla) u'_g + (\mathbf{B} \cdot \nabla) J'_g - (\mathbf{J}_0 \cdot \nabla) B'_g \quad (\text{C.13})$$

$$\left(\frac{\partial}{\partial t} - \eta \nabla^2\right) B'_g = (\mathbf{B} \cdot \nabla) u'_g \quad (\text{C.14})$$

$$\begin{aligned} -\nabla^2 \left(\frac{\partial}{\partial t} - \nu \nabla^2\right) u'_g &= (2\mathbf{\Omega} \cdot \nabla) \omega'_g - \nabla^2 (\mathbf{B} \cdot \nabla) B'_g \\ &\quad - (\mathbf{J}_0 \cdot \nabla) J'_g + |\mathbf{g}| \nabla_H^2 T' \end{aligned} \quad (\text{C.15})$$

$$\left(\frac{\partial}{\partial t} - \eta \nabla^2\right) J'_g = (\mathbf{B} \cdot \nabla) \omega'_g \quad (\text{C.16})$$

$$\left(\frac{\partial}{\partial t} - \kappa \nabla^2\right) T' = \frac{N^2}{|\mathbf{g}|} u'_g \quad (\text{C.17})$$

where $\nabla_H^2 = \nabla^2 - |\mathbf{g}|^{-2}(\mathbf{g} \cdot \nabla)^2$ is the horizontal Laplacian. These five equations form a closed set and, moreover, all the differential operators commute. For example,

$$[\mathbf{B} \cdot \nabla, 2\mathbf{\Omega} \cdot \nabla] = (\mathbf{\Omega} \times \mathbf{J}_0) \cdot \nabla \quad (\text{C.18})$$

$$= 0. \quad (\text{C.19})$$

We can therefore combine all five equations into a single equation

$$\mathcal{M}[u] = 0 \quad (\text{C.20})$$

where u represents any of the dependent variables $\{u'_g, \omega'_g, B'_g, J'_g, T'\}$, and \mathcal{M} is the differential operator

$$\begin{aligned} &\left(\frac{\partial}{\partial t} - \kappa \nabla^2\right) \left[\left(\frac{\partial}{\partial t} - \nu \nabla^2\right) \left(\frac{\partial}{\partial t} - \eta \nabla^2\right) - (\mathbf{B} \cdot \nabla)^2 \right]^2 \nabla^2 \\ &+ \left(\frac{\partial}{\partial t} - \kappa \nabla^2\right) \left[(2\mathbf{\Omega} \cdot \nabla) \left(\frac{\partial}{\partial t} - \eta \nabla^2\right) - (\mathbf{J}_0 \cdot \nabla) (\mathbf{B} \cdot \nabla) \right]^2 \\ &+ \left(\frac{\partial}{\partial t} - \eta \nabla^2\right) \left[\left(\frac{\partial}{\partial t} - \nu \nabla^2\right) \left(\frac{\partial}{\partial t} - \eta \nabla^2\right) - (\mathbf{B} \cdot \nabla)^2 \right] N^2 \nabla_H^2. \end{aligned} \quad (\text{C.21})$$

The unstratified case has been studied by several authors (e.g. [Malkus, 1967](#); [Craik, 1988](#); [Dritschel, 1991](#)). [Malkus \(1967\)](#) considered the case with $\mathbf{B}_0 = 0$ in a spherical geometry, and hence this particular field configuration is often called the ‘‘Malkus field’’. [Craik \(1988\)](#) and [Dritschel \(1991\)](#) considered more general

field configurations, and showed that certain solutions of (C.20) are also exact solutions of the full, nonlinear equations.

In the special case where $\mathbf{J}_0 = 0$ (i.e. the unperturbed magnetic field is uniform) equation C.20 applies even if $\boldsymbol{\Omega}$ is not aligned with \mathbf{g} . Furthermore, the system supports plane wave solutions, known as “magneto–Archimedes–Coriolis” (MAC) waves, with spatio–temporal dependence of the form $\exp(i\mathbf{k} \cdot \mathbf{x} - i\omega t)$, provided that the wave vector \mathbf{k} and frequency ω satisfy the dispersion relation

$$\begin{aligned} 0 = & -\omega^{(\kappa)} [\omega^{(\nu)}\omega^{(\eta)} - (\mathbf{B} \cdot \mathbf{k})^2]^2 |\mathbf{k}|^2 \\ & + \omega^{(\kappa)}\omega^{(\eta)}\omega^{(\eta)} (2\boldsymbol{\Omega} \cdot \mathbf{k})^2 \\ & + \omega^{(\eta)} [\omega^{(\nu)}\omega^{(\eta)} - (\mathbf{B} \cdot \mathbf{k})^2] N^2 |\mathbf{k}_H|^2 . \end{aligned} \quad (\text{C.22})$$

In (C.22) we have defined

$$\mathbf{k}_H = \mathbf{k} - |\mathbf{g}|^{-2}(\mathbf{g} \cdot \mathbf{k})^2, \quad (\text{C.23})$$

$$\omega^{(\kappa)} = \omega + i\kappa|\mathbf{k}|^2, \quad (\text{C.24})$$

$$\omega^{(\eta)} = \omega + i\eta|\mathbf{k}|^2, \quad (\text{C.25})$$

and $\omega^{(\nu)} = \omega + i\nu|\mathbf{k}|^2. \quad (\text{C.26})$

The special cases of Alfvén waves, internal gravity waves and Coriolis waves can all be deduced from (C.22).

Appendix D

The Magnetic Margules Front

We consider a rotating, magnetised fluid within which there is a temperature discontinuity across a surface of negligible curvature; we call this surface a “front”. We suppose that the baroclinicity associated with the temperature discontinuity is supported by discontinuities in the components of the velocity \mathbf{u} and electric current \mathbf{J} that lie within the front. We may describe this situation by considering linear perturbations to a uniformly rotating system containing a uniform magnetic field. Adopting the same notation as in appendix C, the relevant equations are (C.8) and (C.9), together with

$$\mathbf{J}' = \nabla \times \mathbf{B}' . \quad (\text{D.1})$$

Neglecting viscosity, and setting $\mathbf{J}_0 = 0$, the steady-state versions of (C.8) and (C.9) are

$$0 = (2\boldsymbol{\Omega} \cdot \nabla)\mathbf{u}' + (\mathbf{B} \cdot \nabla)\mathbf{J}' + \mathbf{g} \times \nabla T' \quad (\text{D.2})$$

and
$$-\eta \nabla^2 \mathbf{B}' = (\mathbf{B} \cdot \nabla)\mathbf{u}' . \quad (\text{D.3})$$

Defining the normal to the front as the unit vector \mathbf{n} , we decompose the vector fields \mathbf{u}' and \mathbf{J}' into their components parallel and perpendicular to \mathbf{n} :

$$\mathbf{u}' = u'_{\parallel} \mathbf{n} + \mathbf{u}'_{\perp} \quad (\text{D.4})$$

and
$$\mathbf{J}' = J'_{\parallel} \mathbf{n} + \mathbf{J}'_{\perp} . \quad (\text{D.5})$$

After making a similar decomposition for the components of \mathbf{g} , $\boldsymbol{\Omega}$ and \mathbf{B} , we can use (D.1)–(D.3) to derive the following “jump conditions”:

$$[\mathbf{J}'_{\perp}] = \mathbf{n} \times [(\mathbf{n} \cdot \boldsymbol{\nabla})\mathbf{B}'_{\perp}] \quad (\text{D.6})$$

$$0 = 2\Omega_{\parallel}[\mathbf{u}'_{\perp}] + B_{\parallel}[\mathbf{J}'_{\perp}] + \mathbf{g}_{\perp} \times \mathbf{n}[T'] \quad (\text{D.7})$$

$$-\eta [(\mathbf{n} \cdot \boldsymbol{\nabla})\mathbf{B}'_{\perp}] = B_{\parallel}[\mathbf{u}'_{\perp}]. \quad (\text{D.8})$$

where the notation $[\cdot]$ refers to the discontinuity in a quantity across the front. The jump conditions can be combined into a single equation relating the discontinuity in T' to the discontinuities in $[\mathbf{u}'_{\perp}]$:

$$0 = 2\Omega_{\parallel}[\mathbf{u}'_{\perp}] - 2\Omega_{\parallel}\Lambda_{\parallel}\mathbf{n} \times [\mathbf{u}'_{\perp}] + \mathbf{g}_{\perp} \times \mathbf{n}[T'] \quad (\text{D.9})$$

where for notational convenience we have defined an Elsasser number

$$\Lambda_{\parallel} = \frac{B_{\parallel}^2}{2\Omega_{\parallel}\eta}. \quad (\text{D.10})$$

The vector product of (D.9) with \mathbf{n} is

$$0 = 2\Omega_{\parallel}\mathbf{n} \times [\mathbf{u}'_{\perp}] + 2\Omega_{\parallel}\Lambda_{\parallel}[\mathbf{u}'_{\perp}] + \mathbf{g}_{\perp}[T']. \quad (\text{D.11})$$

Eliminating $\mathbf{n} \times [\mathbf{u}'_{\perp}]$ between (D.9) and (D.11) we find

$$0 = 2\Omega_{\parallel}(1 + \Lambda_{\parallel}^2)[\mathbf{u}'_{\perp}] + \mathbf{g}_{\perp} \times \mathbf{n}[T'] + \Lambda_{\parallel}\mathbf{g}_{\perp}[T']. \quad (\text{D.12})$$

In an axisymmetric system, the front must be a surface of revolution about the rotation axis. Then \mathbf{g} and \mathbf{n} both lie within the meridional plane, and the azimuthal component of (D.12) is

$$0 = 2\Omega_{\parallel}(1 + \Lambda_{\parallel}^2)[u'_{\phi}] + (\mathbf{g}_{\perp} \times \mathbf{n}) \cdot \mathbf{e}_{\phi}[T']. \quad (\text{D.13})$$

If $\boldsymbol{\Omega}$ is anti-parallel with \mathbf{g} , we deduce that the front has an angle of inclination, ε say, given by the formula¹

$$\tan \varepsilon = -(1 + \Lambda_{\parallel}^2) \frac{2\Omega_{\parallel}}{g} \frac{[u'_{\phi}]}{[T']}. \quad (\text{D.14})$$

¹This is an implicit formula, since in general Λ_{\parallel} depends on the angle ε .

This situation is illustrated in figure D.1. For a purely hydrodynamic system ($\Lambda_{\parallel} = 0$), equation (D.14) reduces to the well-known Witte–Margules equation for the slope of a Margules front.

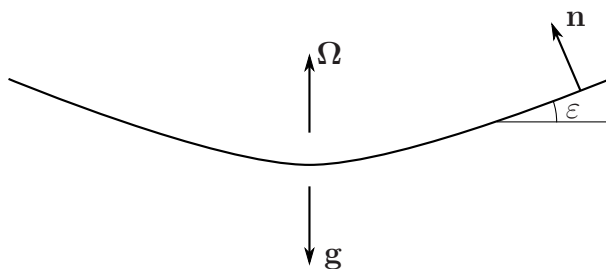


Figure D.1: Meridional cross-section through an axisymmetric front with inclination angle ε and unit normal \mathbf{n} .

Appendix E

Magnetic Pumping

In the presence of weakly non-linear, non-rotating, unstratified, “quasi-isotropic” small-scale turbulence, and in the limit of large turbulent viscosity and magnetic diffusivity, a weak, large-scale magnetic field experiences diamagnetic pumping with a characteristic pumping velocity γ , say. If the turbulence is three-dimensional, then

$$\gamma = -\frac{1}{2}\nabla\eta_e \quad (\text{E.1})$$

(e.g. [Kitchatinov & Rüdiger, 1992](#)), where $\eta_e(\mathbf{x})$ is the effective magnetic diffusivity, the sum of microscopic and turbulent contributions. If the turbulence is two-dimensional, then

$$\gamma = -\nabla\eta_e \quad (\text{E.2})$$

([Zel’dovich, 1957](#)). The evolution of the large-scale field \mathbf{B} , in the absence of large-scale fluid motions, is then described by the mean-field induction equation

$$\frac{\partial\mathbf{B}}{\partial t} = \nabla \times (\gamma \times \mathbf{B} - \eta_e \nabla \times \mathbf{B}). \quad (\text{E.3})$$

For a pumping velocity of the form

$$\gamma = -c\nabla\eta_e, \quad (\text{E.4})$$

where c is constant, [\(E.3\)](#) can be written more compactly as

$$\frac{\partial\mathbf{B}}{\partial t} = -\nabla \times (\eta_e^{1-c} \nabla \times (\eta_e^c \mathbf{B})). \quad (\text{E.5})$$

The strength of the pumping can be measured in terms of the coefficient c , with $c = 0$ corresponding to no pumping.

Following [Kitchatinov & Rüdiger \(2008\)](#), we consider a three-layer solar model. We assume that the effective magnetic diffusivity η_e takes a small value, η_0 say, within the radiative interior, but a much larger value, η_1 say, within the convection zone. Both η_0 and η_1 are assumed to be constant, implying a discontinuity in η_e at the radiative–convective interface. The region outside the Sun is approximated as a vacuum, wherein $\nabla \times \mathbf{B} = 0$. We assume that \mathbf{B} is poloidal and axisymmetric, so that it can be defined in terms of a scalar potential A :

$$\mathbf{B} = \nabla \times (A \mathbf{e}_\phi) \quad (\text{E.6})$$

where \mathbf{e}_ϕ is the unit vector directed azimuthally. The induction equation can then be “uncurled” and written in the form

$$\frac{\partial A}{\partial t} = r \eta_e^{1-c} \nabla \cdot \left(\frac{\eta_e^c}{r^2} \nabla (rA) \right) \quad (\text{E.7})$$

where r is the perpendicular distance from the axis of symmetry. The discontinuity in η_e at the base of the convection zone implies a delta function in the pumping velocity γ , and leads to the following matching conditions at the interface with the radiative envelope:

$$[A] = 0, \quad (\text{E.8})$$

$$[\eta_e^c \mathbf{n} \cdot \nabla (rA)] = 0, \quad (\text{E.9})$$

where \mathbf{n} is the normal to the interface. These matching conditions imply that the vertical field $\mathbf{n} \cdot \mathbf{B}$ is continuous at the interface, but that the horizontal field $\mathbf{n} \times \mathbf{B}$ is discontinuous, and is smaller on the convection-zone side of the interface by a factor $(\eta_0/\eta_1)^c$.

We are interested in the long-time behaviour of the system, i.e. the behaviour on timescales comparable to the global magnetic diffusion time in the radiative interior. On such timescales we may assume that magnetic diffusion within the

convection zone is instantaneous, since $\eta_1 \gg \eta_0$. Hence (E.7) becomes

$$\nabla \cdot \left(\frac{1}{r^2} \nabla (rA) \right) = 0 \quad (\text{E.10})$$

within the convection zone, which is equivalent to $\nabla \times \mathbf{B} = 0$. The location of the solar surface is now immaterial, since we have a vacuum field everywhere outside the radiative interior.

After a sufficiently long time, the magnetic field in the radiative interior will become dipolar, since the dipolar component has the longest decay time. If the radiative–convective interface is approximated as spherical, then the vacuum field outside the radiative interior must be

$$A = r/|\mathbf{x}|^3 \quad (\text{E.11})$$

after this time. Hence $\mathbf{n} \times \mathbf{B}$ and $\mathbf{n} \cdot \mathbf{B}$ are of similar magnitude at the base of the convection zone, regardless of the pumping strength c . At the top of the radiative envelope the matching conditions (E.8) and (E.9) then imply that the horizontal field $\mathbf{n} \times \mathbf{B}$ is typically larger than the vertical field $\mathbf{n} \cdot \mathbf{B}$ by a factor of $(\eta_1/\eta_0)^c$. Hence if $(\eta_1/\eta_0)^c \gg 1$ then the magnetic field is confined, i.e. predominantly horizontal, below the base of the convection zone.

However, we note that solutions of equation (E.3) are generally not force-free. Indeed, the Lorentz force will be particularly large at the base of the convection zone, where the vertical discontinuity in the horizontal field implies the existence of a current sheet. A complete and self-consistent model of magnetic confinement by turbulent pumping would need to take into account the dynamical effects of this force, including its effect on the turbulence and hence the pumping velocity γ .

Appendix F

The Tayler Instability

In this section, we re-derive a simple case of Tayler instability described by [Spruit \(1999\)](#). ([Spruit](#) considered more general toroidal field configurations than we do here.) We consider perturbations to a uniformly rotating, stably stratified fluid containing a magnetic field of the form

$$\mathbf{B} = \frac{1}{2}\mathbf{J}_0 \times \mathbf{x}, \quad (\text{F.1})$$

where \mathbf{J}_0 is uniform. We suppose that gravity \mathbf{g} and the fluid's angular velocity $\boldsymbol{\Omega}$ are both uniform and parallel to \mathbf{J}_0 . As shown in [appendix C](#), linear perturbations in such a fluid can be described by the equation

$$\mathcal{M}[u] = 0 \quad (\text{F.2})$$

where \mathcal{M} is the operator

$$\begin{aligned} & \left(\frac{\partial}{\partial t} - \kappa \nabla^2 \right) \left[\left(\frac{\partial}{\partial t} - \nu \nabla^2 \right) \left(\frac{\partial}{\partial t} - \eta \nabla^2 \right) - (\mathbf{B} \cdot \nabla)^2 \right]^2 \nabla^2 \\ & + \left(\frac{\partial}{\partial t} - \kappa \nabla^2 \right) \left[(2\boldsymbol{\Omega} \cdot \nabla) \left(\frac{\partial}{\partial t} - \eta \nabla^2 \right) - (\mathbf{J}_0 \cdot \nabla)(\mathbf{B} \cdot \nabla) \right]^2 \\ & + \left(\frac{\partial}{\partial t} - \eta \nabla^2 \right) \left[\left(\frac{\partial}{\partial t} - \nu \nabla^2 \right) \left(\frac{\partial}{\partial t} - \eta \nabla^2 \right) - (\mathbf{B} \cdot \nabla)^2 \right] N^2 \nabla_H^2. \end{aligned} \quad (\text{F.3})$$

We suppose that the magnetic field is weak, in the sense that $|\mathbf{J}_0| \ll |\boldsymbol{\Omega}|$, and that the system is “heavily stratified”, i.e. $|\boldsymbol{\Omega}| \ll N$. In the absence of thermal

and magnetic diffusion, the system would be stable. In the presence of thermal or magnetic diffusion, there are unstable modes that grow on a timescale $\tau \sim |\Omega|/|\mathbf{J}_0|^2$ (Pitts & Tayler, 1985). In order for diffusion to destabilise the motions, they must have a small vertical scale, say δ . On the other hand, the motions must have a large horizontal scale, in order to avoid significantly perturbing the stratification surfaces. For such motions we may approximate $\nabla^2 \approx \partial^2/\partial z^2$, where z is the vertical coordinate.

In the radiative envelope, where $\kappa \gg \eta \gg \nu$, Tayler instability is possible only if δ lies in the range

$$\kappa/\delta^2 \gg \tau^{-1} \gtrsim \eta/\delta^2 \gg \nu/\delta^2 \quad (\text{F.4})$$

(Spruit, 1999). In that case we may neglect viscosity, and assume that thermal diffusion is instantaneous, so that $(\frac{\partial}{\partial t} - \kappa \nabla^2) \rightarrow (-\kappa \nabla^2)$ in (F.3). Since the timescale for the instability τ is much longer than the rotation period, we also make the magnetostrophic approximation, and therefore neglect all terms in (F.3) containing the factor $(\frac{\partial}{\partial t} - \nu \nabla^2)$.

Defining cylindrical coordinates (r, ϕ, z) centred on the rotation axis, we seek solutions to (F.2) of the form

$$u = \hat{u}(r) \exp(inz + im\phi - i\omega t) , \quad (\text{F.5})$$

where n is real and m is integer. Applying the approximations listed above, (F.2) then becomes

$$(\nabla_H^2 + L^{-2})u = 0 , \quad (\text{F.6})$$

with

$$L^{-2} = \frac{i\kappa n^4 |\mathbf{J}_0|^2}{N^2(\omega + i\eta n^2)} \left[\left(1 + \frac{4\Omega(\omega + i\eta n^2)}{|\mathbf{J}_0|^2 m} \right)^2 - \frac{m^2}{4} \right] . \quad (\text{F.7})$$

Necessary conditions for instability are that $L^2 > 0$ and $\text{Im } \omega > 0$. After writing ω as the sum of (dimensionless) real and imaginary parts

$$\omega = \frac{|\mathbf{J}_0|^2}{4\Omega} (\tilde{\omega}_R + i\tilde{\omega}_I) \quad (\text{F.8})$$

we take the real and imaginary parts of (F.7), treating L^2 as real, which leads to

the following equations for $\tilde{\omega}_I$ and L :

$$\left(\tilde{\omega}_I + \frac{4\Omega\eta n^2}{|\mathbf{J}_0|^2}\right)^2 = m^2 \left[\frac{\frac{1}{4}m^2 - (1 + \tilde{\omega}_R/m)^2}{1 + 2m/\tilde{\omega}_R} \right] \quad (\text{F.9})$$

$$\frac{N^2 L^{-2}}{8\Omega\kappa n^4} = -\left(\frac{1}{m} + \frac{1}{\tilde{\omega}_R}\right) \left[\frac{\frac{1}{4}m^2 - (1 + \tilde{\omega}_R/m)^2}{1 + 2m/\tilde{\omega}_R} \right]^{1/2}. \quad (\text{F.10})$$

For a mode of the form (F.5) to be unstable, the right-hand sides of (F.9) and (F.10) must be positive, which requires that $m = 1$ and $-\frac{1}{2} < \tilde{\omega}_R < 0$.

If there are no further constraints on n and L then there are always unstable modes. If, however, the domain is of finite horizontal extent, then there will be an upper bound on L , say L_0 . This in turn implies a lower bound on the vertical wavenumber n , which can be deduced from (F.10). But n cannot be too large, or else the instability will be damped by magnetic diffusion, as can be seen from (F.9). In fact, for a given value of $\tilde{\omega}_R$, instability is possible if and only if

$$\left(\frac{4\Omega\eta n^2}{|\mathbf{J}_0|^2}\right)^2 < \frac{\frac{1}{4} - (1 + \tilde{\omega}_R)^2}{1 + 2/\tilde{\omega}_R}, \quad (\text{F.11})$$

with n given by

$$\frac{N^2 L_0^{-2}}{8\Omega\kappa n^4} = -(1 + 1/\tilde{\omega}_R) \left[\frac{\frac{1}{4} - (1 + \tilde{\omega}_R)^2}{1 + 2/\tilde{\omega}_R} \right]^{1/2}. \quad (\text{F.12})$$

By considering all $\tilde{\omega}_R$ in the range $(-\frac{1}{2}, 0)$, we deduce that the necessary and sufficient condition for instability is

$$\frac{2\Omega\eta^2 N^2 L_0^{-2}}{\kappa |\mathbf{J}_0|^4} < \max_{\tilde{\omega} \in (-\frac{1}{2}, 0)} \left\{ -(1 + 1/\tilde{\omega}) \left[\frac{\frac{1}{4} - (1 + \tilde{\omega})^2}{1 + 2/\tilde{\omega}} \right]^{3/2} \right\} \quad (\text{F.13})$$

$$\approx 0.05 \quad (\text{F.14})$$

$$\Rightarrow |\mathbf{J}_0|^4 \gtrsim \frac{40\Omega\eta^2 N^2}{\kappa L_0^2}. \quad (\text{F.15})$$

Appendix G

The Tayler–Spruit Dynamo

We consider a horizontal layer of stably stratified rotating fluid, threaded by a weak, approximately homogeneous magnetic field. If we impose vertical differential rotation within this layer, then the weak field will be wound up into a roughly axisymmetric toroidal field, in accordance with the principle of rotational smoothing described in §3.2. Assuming that the vertical shear is not too large, the toroidal field will continue to grow in strength, but remain stable, until the Tayler-instability criterion (F.15) is exceeded. The instability generates a vertical field component. If the imposed shear winds up this vertical field component into new toroidal field sufficiently quickly, the instability can operate continually, resulting in a dynamo (Spruit, 2002). Spruit argued that the dynamo would oppose the imposed shear through its Maxwell stress, yielding an effective turbulent viscosity ν_T . By assuming that the vertical and azimuthal field components in the saturated dynamo are correlated in the manner of the most unstable Tayler mode, Spruit estimated this viscosity to be

$$\nu_T \sim \Omega \delta^2 \tag{G.1}$$

in a neighbourhood of the rotation axis, where δ is the vertical scale of the instability. He also estimated the minimum vertical shear required to sustain dynamo action as

$$\left| \frac{d\Omega}{dz} \right| \sim \eta / \delta^3 \tag{G.2}$$

where z is the vertical coordinate. In the idealised scenario described in appendix F, the vertical scale of the Tayler instability can be deduced from (F.12):

$$\delta^{-4} \sim n^4 \sim \frac{N^2}{\Omega \kappa L_0^2} . \quad (\text{G.3})$$

McIntyre (2007) suggested that a Tayler–Spruit dynamo operating within the high-latitude tachocline might gyroscopically pump the downwelling required to confine the Sun’s interior magnetic field. The downwelling that can be pumped by this mechanism can be estimated using Spruit’s estimate (G.1) for the turbulent viscosity. We define cylindrical polar coordinates (r, ϕ, z) centred on the rotation axis. Within a neighbourhood of the north pole, the angular velocity Ω and density ρ within the tachocline may be assumed to depend only on height z . We assume that the effective viscosity ν_e is also a function of z . Within the bulk of the tachocline, we have $\nu_e = \nu_T$, with ν_T given by (G.1). Within the laminar magnetic confinement layer at the base of the tachocline, the effective viscosity drops to its microscopic value, which we shall take to be zero here. The latitudinal flow pumped by the tachocline’s Tayler–Spruit dynamo can be estimated by balancing the azimuthal Coriolis force against the divergence of the turbulent stress:

$$2\Omega \rho u_r = \frac{d}{dz} \left(\rho r \nu_e \frac{d\Omega}{dz} \right) . \quad (\text{G.4})$$

Since $\nu_e(z)$ increases steeply with height within the tachocline, against a background of negative shear $d\Omega/dz$, we anticipate that the gyroscopically pumped flow will be poleward, with $u_r \propto -r$. Now applying mass conservation, $\nabla \cdot (\rho \mathbf{u}) = 0$, we deduce that

$$\frac{d(\rho u_z)}{dz} = -2\rho u_r / r \quad (\text{G.5})$$

$$= -\frac{d}{dz} \left(\rho \nu_e \frac{d \ln \Omega}{dz} \right) . \quad (\text{G.6})$$

From the principle of downward control (Haynes *et al.*, 1991) we expect the converging poleward flow to turn downward. Assuming that there is no gyroscopic pumping in the layers above the tachocline, the vertical flow u_z within the bulk of the tachocline must vanish. We can then integrate (G.6) vertically to calculate the downwelling pumped into the top of the confinement layer. Neglecting the

small changes in density within the tachocline, we find

$$u_z = \nu_T \frac{d \ln \Omega}{dz} . \quad (\text{G.7})$$

Following McIntyre (2007) we suppose that the turbulent stresses within the tachocline prevent the vertical shear from growing significantly beyond the threshold value given by (G.2). We can then apply the estimates (G.1) and (G.2) to the downwelling formula (G.7) to obtain

$$u_z = \eta / \delta . \quad (\text{G.8})$$

The estimate (G.1) for the turbulent viscosity assumes that the magnetic field generated by the Tayler–Spruit dynamo has the large-scale horizontal structure associated with Tayler instability. However, Denissenkov & Pinsonneault (2007) have argued that such a large-scale field would not be sustained in the nonlinear regime, and that (G.1) therefore overestimates the angular momentum transport that can be produced by a Tayler–Spruit dynamo. In that case, we should regard (G.8) as an upper bound for the downwelling that can be pumped by a Tayler–Spruit dynamo operating at threshold within the tachocline.

Appendix H

The Numerical Scheme

H.1 Equations

We wish to solve a suitable version of equations (7.7)–(7.12) in axisymmetric cylindrical polar coordinates. We introduce streamfunctions Ψ and A , i.e. azimuthal vector-potential components, for the poloidal velocity and magnetic fields, such that

$$u_z = \frac{1}{r} \frac{\partial(r\Psi)}{\partial r} \quad \text{and} \quad u_r = -\frac{\partial\Psi}{\partial z}, \quad (\text{H.1})$$

$$B_z = \frac{1}{r} \frac{\partial(rA)}{\partial r} \quad \text{and} \quad B_r = -\frac{\partial A}{\partial z}, \quad (\text{H.2})$$

guaranteeing that the fields are divergence-free. In the fluid-dynamical literature $r\Psi$ is sometimes called the Stokes streamfunction. The azimuthal vorticity ω_ϕ and electric current J_ϕ are related to Ψ and A by

$$\omega_\phi = -(\nabla^2 - r^{-2}) \Psi \quad (\text{H.3})$$

$$\text{and} \quad J_\phi = -(\nabla^2 - r^{-2}) A. \quad (\text{H.4})$$

For numerical reasons described below, we introduce anisotropic viscosity and helium diffusivity with dimensionless horizontal components ν_H and χ_H . So

equations (7.7)–(7.12) are replaced by

$$\begin{aligned} \text{Ro} \frac{1}{r} \frac{D(ru_\phi)}{Dt} &= \frac{\partial \Psi}{\partial z} + \frac{1}{r} \mathbf{B} \cdot \nabla (rB_\phi) \\ &\quad + \text{Ek} \left[\frac{\partial^2}{\partial z^2} + \nu_H (\nabla_H^2 - r^{-2}) \right] u_\phi \end{aligned} \quad (\text{H.5})$$

$$\begin{aligned} \text{Ro} \left[r \frac{D(\omega_\phi/r)}{Dt} + \frac{\partial(ru_\phi, u_\phi/r)}{\partial(z, r)} \right] &= \frac{\partial u_\phi}{\partial z} - \alpha_T \frac{\partial T}{\partial r} + \alpha_\mu \frac{\partial \mu}{\partial r} \\ &\quad + r \mathbf{B} \cdot \nabla (J_\phi/r) + \frac{\partial(rB_\phi, B_\phi/r)}{\partial(z, r)} \\ &\quad + \text{Ek} \left[\frac{\partial^2}{\partial z^2} + \nu_H (\nabla_H^2 - r^{-2}) \right] \omega_\phi \end{aligned} \quad (\text{H.6})$$

$$r \frac{D(B_\phi/r)}{Dt} = r \mathbf{B} \cdot \nabla (u_\phi/r) + (\nabla^2 - r^{-2}) B_\phi \quad (\text{H.7})$$

$$\frac{1}{r} \frac{D(rA)}{Dt} = (\nabla^2 - r^{-2}) A \quad (\text{H.8})$$

$$\frac{DT}{Dt} = \frac{\kappa}{\eta} \nabla^2 T \quad (\text{H.9})$$

$$\frac{D\mu}{Dt} = \frac{\chi}{\eta} \left[\frac{\partial^2}{\partial z^2} + \chi_H \nabla_H^2 \right] \mu. \quad (\text{H.10})$$

Because of the axisymmetric cylindrical geometry, the lack of spatial periodicity, and the wide range of spatial scales inherent in the polar confinement-layer problem, a spectral or pseudospectral code would be unsuited to the task of solving these equations. Instead, a simple finite-difference code has been written in cylindrical polar coordinates, with an Eulerian grid regularly spaced in r and z at intervals Δr and Δz . The outer boundary of the computational domain is at $r = r_d$. The inner boundary is at $r = 2\Delta r$, i.e. two grid intervals from the coordinate singularity at the rotation axis. For reasons of symmetry and good behaviour near the coordinate singularity, the finite differencing is done by locally approximating the fields Ψ/r , u_ϕ/r , ω_ϕ/r , A/r , B_ϕ/r , T , and μ as functions that are linear in z and in r^2 over a single grid interval. This ensures that the error is $O(\Delta r)$ even for small r . Field values for $r < 2\Delta r$ are obtained by extrapolation from $r = 3\Delta r$ and $r = 2\Delta r$, again assuming linear functional dependence on r^2 .

With the parameter values given in table 10.1, the dimensionless helium-sublayer and Ekman-layer thicknesses are $\delta_\chi/\delta_\eta = (\chi/\eta)^{1/2} \approx 0.14$ and $\delta_{\text{Ek}}/\delta_\eta = \text{Ek}^{1/2} \approx 0.01$ respectively. We have chosen a vertical grid interval $\Delta z = 0.01$, dimen-

sionally $0.01\delta_\eta$, which is small enough to resolve the helium sublayer accurately. This Δz is too large to resolve any Ekman layers. However, Ekman layers are prevented from becoming significant by careful choice of the code representing the boundary conditions (see §10.3).

An explicit Eulerian timestepping scheme is used to evolve the system. The timestep Δt must be small enough to resolve thermal diffusion at the grid scale, which is the fastest process at this scale and therefore determines the Courant–Friedrichs–Lewy condition. With the parameter values given in table 10.1, this constraint becomes $\Delta t \lesssim (\eta/\kappa)(\Delta z)^2 = 10^{-2} \times (0.01)^2 = 10^{-6}$, dimensionally $10^{-6}\delta_\eta/U$ or $10^{-4}(2\Omega_i)^{-1}$. The system typically takes several domain-scale magnetic diffusion times to reach a steady state, and multiple iterations of the peripheral $B_\phi(z)$ profile are required to achieve a steady state with vanishing $B_\phi(r)$ at the bottom. To make the computation feasible, in a domain wide enough to accommodate noticeable tilting effects, we have used $r_d = 5$, dimensionally $5\delta_\eta$, and a horizontal grid interval $\Delta r = 0.1$, dimensionally $0.1\delta_\eta$, larger than the vertical grid interval Δz by a factor of 10. To ensure that the diffusive terms in (H.5), (H.6) and (H.10) are dominant at the grid scale, we increased the horizontal viscosity and helium diffusivity each by a factor of 10, i.e. $\nu_H = \chi_H = 10$. We have verified, in smaller computational domains, that the coarser horizontal resolution and the anisotropic diffusion do not qualitatively affect the steady state of the system (see §§I.4 and I.5). The increased horizontal viscosity introduces stronger angular momentum coupling between neighbouring Ferraro surfaces, and typically brings the system’s steady state closer to uniform rotation below the confinement layer. In this sense the artificial viscosity acts rather like the hypothesized shear-induced turbulence mentioned in §3.2.

At each timestep, the azimuthal vorticity ω_ϕ is updated and the streamfunction Ψ then computed from (H.3) by inverting the operator $\nabla^2 - r^{-2}$, approximated using centred differences. The inversion is performed iteratively, using a successive-overrelaxation method described in Press *et al.* (1986). During the early evolution, when the dynamics is dominated by timescales not much longer than the timestep Δt (see §I.1), many such iterations are required, at each timestep, to achieve convergence. At later times the same degree of convergence can be achieved with far fewer iterations. Since we are interested only in the ultimate

steady state, we can tolerate a larger error in the inversion during the early evolution. Further details of the numerical code are given in §H.2.

As anticipated from scaling arguments, the steady state is found to be close to magnetostrophic balance (see §I.2). It might be thought that imposing magnetostrophic balance throughout the evolution, as first suggested by Taylor (1963), would filter out all the fast oscillations, including inertial or epicyclic oscillations, and thereby allow larger timesteps to be used. However, the imposition of magnetostrophic balance leads to pathological behaviour at small scales (Walker *et al.*, 1998). Far from eliminating or slowing the fast oscillations, the imposition of balance exacerbates the problem, for reasons explained in §H.3.

H.2 Finite-differences

We consider grid-scale perturbations in a region of the numerical domain away from the axis, so that curvature terms may be neglected. We linearise equations (H.5)–(H.9) about a background state with a uniform magnetic field \mathbf{B} and a uniform vertical temperature gradient $dT/dz = 1$. For simplicity we ignore gradients in μ . (The terms in our equations involving μ will be computed in the same fashion as the terms involving T .) We may also assume that the background state is at rest, provided that the grid intervals Δr and Δz are small enough that diffusion dominates advection at the grid scale.

Using primes to denote the perturbations, the linearised equations are

$$\text{Ro} \frac{\partial}{\partial t} u'_\phi - \frac{\partial}{\partial z} {}^{(1)}\Psi' = \mathbf{B} \cdot \nabla^{(1)} B'_\phi + \text{Ek} \left[\frac{\partial^2}{\partial z^2} + \nu_H \nabla_H^2 \right] u'_\phi \quad (\text{H.11})$$

$$\text{Ro} \frac{\partial}{\partial t} \omega'_\phi - \frac{\partial}{\partial z} {}^{(2)}u'_\phi = -\alpha_T \frac{\partial}{\partial r} {}^{(1)}T' + \mathbf{B} \cdot \nabla^{(2)} J'_\phi + \text{Ek} \left[\frac{\partial^2}{\partial z^2} + \nu_H \nabla_H^2 \right] \omega'_\phi \quad (\text{H.12})$$

$$\frac{\partial}{\partial t} B'_\phi = \mathbf{B} \cdot \nabla^{(3)} u'_\phi + \nabla^2 B'_\phi \quad (\text{H.13})$$

$$\frac{\partial}{\partial t} A' = \mathbf{B} \cdot \nabla^{(4)} \Psi' + \nabla^2 A' \quad (\text{H.14})$$

$$\frac{\partial}{\partial t} T' + \frac{\partial}{\partial r} {}^{(2)}\Psi' = \frac{\kappa}{\eta} \nabla^2 T' \quad (\text{H.15})$$

$$\omega'_\phi = -\nabla^2 \Psi' \quad (\text{H.16})$$

$$J'_\phi = -\nabla^2 A' \quad (\text{H.17})$$

where the operators $\partial/\partial z$, $\mathbf{B} \cdot \nabla$, etc. represent finite difference operators. The Laplacian-type operators are all evaluated using three-point, centred (first-order) finite differences. Operators with superscripts in brackets are evaluated using two-point, one-sided (first-order) finite differences. We would like to choose the directions of these one-sided differences such that small scales in the system behave as MAC waves (see appendix C).

To simplify the notation, we define new operators

$$\text{Ro} \frac{\partial^{(\nu)}}{\partial t} = \text{Ro} \frac{\partial}{\partial t} - \text{Ek} \left[\frac{\partial^2}{\partial z^2} + \nu_H \nabla_H^2 \right], \quad (\text{H.18})$$

$$\frac{\partial^{(\eta)}}{\partial t} = \frac{\partial}{\partial t} - \nabla^2, \quad (\text{H.19})$$

$$\text{and} \quad \frac{\partial^{(\kappa)}}{\partial t} = \frac{\partial}{\partial t} - \frac{\kappa}{\eta} \nabla^2. \quad (\text{H.20})$$

The linear equations (H.11)–(H.17) can be combined into a single equation

$$\mathcal{M}[u] = 0, \quad (\text{H.21})$$

where u represents any of the fields $\{\Psi', u'_\phi, A', B'_\phi, T'\}$, and \mathcal{M} is the operator

$$\begin{aligned} & \frac{\partial^{(\kappa)}}{\partial t} \left[\text{Ro} \frac{\partial^{(\nu)}}{\partial t} \frac{\partial^{(\eta)}}{\partial t} - \mathbf{B} \cdot \nabla^{(1)} \mathbf{B} \cdot \nabla^{(3)} \right] \left[\text{Ro} \frac{\partial^{(\nu)}}{\partial t} \frac{\partial^{(\eta)}}{\partial t} - \mathbf{B} \cdot \nabla^{(2)} \mathbf{B} \cdot \nabla^{(4)} \right] \nabla^2 \\ & + \frac{\partial^{(\kappa)}}{\partial t} \frac{\partial^{(1)}}{\partial z} \frac{\partial^{(2)}}{\partial z} \frac{\partial^{(\eta)}}{\partial t} \frac{\partial^{(\eta)}}{\partial t} \\ & + \frac{\partial^{(\eta)}}{\partial t} \left[\text{Ro} \frac{\partial^{(\nu)}}{\partial t} \frac{\partial^{(\eta)}}{\partial t} - \mathbf{B} \cdot \nabla^{(1)} \mathbf{B} \cdot \nabla^{(3)} \right] \alpha_T \frac{\partial^{(1)}}{\partial r} \frac{\partial^{(2)}}{\partial r} \end{aligned} \quad (\text{H.22})$$

(cf. equation (C.21)). In the numerical scheme, the one-sided difference operators $\frac{\partial^{(1)}}{\partial z}$ and $\frac{\partial^{(2)}}{\partial z}$ are evaluated in opposite directions (i.e. one is “up” and one is “down”) so that

$$\frac{\partial^{(1)}}{\partial z} \frac{\partial^{(2)}}{\partial z} = \frac{\partial^2}{\partial z^2} \quad (\text{H.23})$$

where $\frac{\partial^2}{\partial z^2}$ is a first-order-accurate centred difference. Similarly, $\frac{\partial^{(1)}}{\partial r}$ is evaluated in the opposite direction to $\frac{\partial^{(2)}}{\partial r}$, $\mathbf{B} \cdot \nabla^{(1)}$ is evaluated in the opposite direction to $\mathbf{B} \cdot \nabla^{(3)}$, and $\mathbf{B} \cdot \nabla^{(2)}$ is evaluated in the opposite direction to $\mathbf{B} \cdot \nabla^{(4)}$. These choices ensure that the system’s small-scale behaviour mimics that of true MAC waves as closely as possible. The remaining degrees of freedom in choosing the

Table H.1: The directions chosen for the one-sided finite differences. “Upward”, for example, means that the derivative at each grid point is evaluated using the difference between the value at that grid point and the value at the grid point immediately above.

Finite difference	Direction chosen	Finite difference	Direction chosen
$\frac{\partial}{\partial z}^{(1)}$	upward	$\frac{\partial}{\partial z}^{(2)}$	downward
$\frac{\partial}{\partial r}^{(1)}$	outward	$\frac{\partial}{\partial r}^{(2)}$	inward
$\mathbf{B} \cdot \nabla^{(1)}$	upward and inward	$\mathbf{B} \cdot \nabla^{(3)}$	downward and outward
$\mathbf{B} \cdot \nabla^{(2)}$	downward and outward	$\mathbf{B} \cdot \nabla^{(4)}$	upward and inward

directions for the differences have been used to allow the most straightforward implementation of the boundary conditions (§10.3). For example, since we specify a peripheral boundary condition for T , it is convenient to define the difference operator $\frac{\partial}{\partial r}^{(1)}$ in (H.12) as an “outward” directed difference. The directionalities chosen for all one-sided finite differences are listed in table H.1.

The code is written in C and currently runs on a single processor only. The source code is available online¹ or by request.²

H.3 Magnetostrophic balance

Because the confinement-layer problem involves only steady or nearly-steady flow, it is natural to try to save computational resources by filtering out the fast oscillations (e.g. Taylor, 1963). These include Alfvén waves, gravity waves, inertia/Coriolis/epicyclic waves and the various hybrid types (see appendix C). Such filtering is familiar, and often effective, in many other problems involving stiff differential equations. A well known example is that of fluid flow in non-MHD fluid systems with strong rotation and stable stratification. The standard “quasi-geostrophic equations” result from small-Ro approximations that filter out inertia and gravity waves, as well as sound waves, allowing relatively large time steps.

¹www.damtp.cam.ac.uk/user/tsw25/cl-code/

²t.wood.02 "at" cantab.net

Such filtering turns out, however, to be ineffective in the confinement-layer problem. Indeed — at first sight paradoxically — the imposition of magnetostrophic balance leads to pathological behaviour in the following sense. Far from eliminating fast oscillations, it introduces spurious modes of oscillation that are even faster, as shown by [Walker *et al.* \(1998\)](#) in the context of the terrestrial dynamo problem. Following [Walker *et al.*](#), we show how the pathology can be understood through an idealised analysis of the fast oscillations, first in the unfiltered and then in the filtered equations.

The reason for the pathology is the interplay between the Coriolis and Lorentz forces. Stratification N^2 is relatively unimportant, as will be shown shortly. We therefore start with the linear theory of MC (magneto–Coriolis) waves, i.e. small plane-wave disturbances to an unstratified, incompressible fluid with uniform rotation $\mathbf{\Omega}$ and a uniform magnetic field \mathbf{B} . Neglecting viscosity and magnetic diffusivity, we find the well-known dispersion relation

$$\omega^2 - (\mathbf{B} \cdot \mathbf{k})^2 = \pm 2\mathbf{\Omega} \cdot \mathbf{k} \omega / |\mathbf{k}|, \quad (\text{H.24})$$

where ω is the frequency and \mathbf{k} is the wavevector, both dimensional here. If we take the limit of rapid rotation, $|\mathbf{\Omega}| \rightarrow \infty$, then for most choices of \mathbf{k} the four roots of this dispersion relation are asymptotically

$$\omega \sim \pm \frac{2\mathbf{\Omega} \cdot \mathbf{k}}{|\mathbf{k}|}, \quad (\text{H.25})$$

and

$$\omega \sim \pm \frac{(\mathbf{B} \cdot \mathbf{k})^2}{2\mathbf{\Omega} \cdot \mathbf{k}} |\mathbf{k}|. \quad (\text{H.26})$$

The modes corresponding to (H.25) are inertial waves — in this context sometimes called “fast MC waves” — and those corresponding to (H.26) are “slow MC waves”. By imposing magnetostrophic balance we neglect relative fluid accelerations, which corresponds to dropping the ω^2 term from the left-hand side of (H.24). The dispersion relation then becomes

$$\omega = \pm \frac{(\mathbf{B} \cdot \mathbf{k})^2}{2\mathbf{\Omega} \cdot \mathbf{k}} |\mathbf{k}|, \quad (\text{H.27})$$

so imposing magnetostrophic balance eliminates the two “fast” branches (H.25) of the full dispersion relation (H.24).

However, not all modes of the full dispersion relation (H.24) have the asymptotic behaviour described by (H.25) and (H.26). Even in the presence of rapid rotation, there are always some modes whose \mathbf{k} values satisfy

$$|\mathbf{B} \cdot \mathbf{k}| \gg |2\boldsymbol{\Omega} \cdot \mathbf{k}|/|\mathbf{k}| \quad \text{as} \quad |\boldsymbol{\Omega}| \rightarrow \infty, \quad (\text{H.28})$$

and such modes behave like Alfvén waves, i.e. $\omega \sim \pm \mathbf{B} \cdot \mathbf{k}$. Imposing magnetostrophic balance removes the mechanism for Alfvén wave propagation, and must therefore alter the behaviour of these modes. From (H.27) we find that these modes now have a very high frequency. In fact if we fix $2\boldsymbol{\Omega} \cdot \mathbf{k}$ and allow $|\mathbf{k}| \rightarrow \infty$ then ω grows as $|\mathbf{k}|^3$. The conclusion is that even in a rapidly rotating system *some modes of the full dispersion relation always feel the Lorentz force more strongly than the Coriolis force*, and these modes become ill-behaved under the assumption of magnetostrophic balance. A numerical scheme that imposes magnetostrophic balance will therefore be ill-conditioned.

If we introduce stratification N^2 then (H.27) becomes

$$\omega = \pm \frac{\mathbf{B} \cdot \mathbf{k}}{2\boldsymbol{\Omega} \cdot \mathbf{k}} [(\mathbf{B} \cdot \mathbf{k})^2 |\mathbf{k}|^2 + N^2(|\mathbf{k}|^2 - k_V^2)]^{1/2}, \quad (\text{H.29})$$

where k_V is the vertical component of \mathbf{k} . Therefore the presence of stratification serves only to increase the frequency of the ill-behaved modes, and thereby to exacerbate the problem.

Appendix I

Numerical Test Cases

I.1 Transient adjustment

The numerical scheme timesteps equations (H.5)–(H.10) forwards in time from a given initial condition. We typically take the initial condition to be a previously computed numerical or analytical confinement-layer solution. The behaviour at early times is characterised by “sloshing” of the flow through the confinement layer, leading to undulations of the helium sublayer on timescales of the order of the inverse buoyancy frequency. Figure I.1 shows the meridional streamlines in a vertical cross-section through the computational domain during this transient adjustment phase. An animated version of this figure is available online at www.damtp.cam.ac.uk/user/tsw25/adjust.avi. The animation shows the evolution of the poloidal streamlines over a dimensionless time interval of 5×10^{-2} , dimensionally $50/N$, where N is the total buoyancy frequency at the bottom of the domain. The meridional flow typically settles into a quasi-steady state after a dimensionless time much less than unity. The magnetic field, on the other hand, typically takes a dimensionless time of order unity to achieve a steady state.

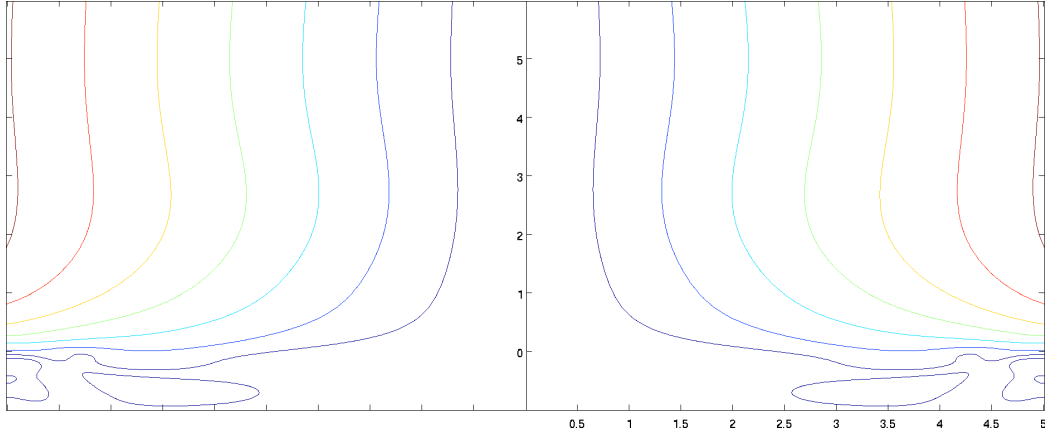


Figure I.1: Meridional streamlines in a vertical cross-section through the confinement layer during its transient adjustment towards a steady state.

I.2 Magnetostrophic balance

The evolution of angular momentum in the numerical scheme is described by equation (H.5). Since both Ro and Ek are much smaller than unity, we anticipate that the solutions will be close to magnetostrophic balance, with

$$0 \approx \frac{1}{r} \frac{\partial \Psi}{\partial z} + \frac{1}{r^2} \mathbf{B} \cdot \nabla (r B_\phi). \quad (\text{I.1})$$

In figure I.2 we plot the first and second terms on the right-hand side of (I.1) in a vertical cross-section through the same numerical solution¹ presented in figure 7.2. In figure I.3 we plot the sum of these two terms, which would vanish if the solution were in perfect magnetostrophic balance. We see that both terms in (I.1) are largest within the confinement layer, and both are close to zero above and below the confinement layer. As expected, their sum is close to zero throughout the domain, indicating that the solution is very nearly magnetostrophically balanced. The largest absolute departures from magnetostrophic balance are localised next to the vertical outer boundary, where we impose profiles of T and μ taken from a perfectly flat, analytical confinement-layer solution (§7.5). The largest *relative* departures from magnetostrophic balance occur above and below the confinement layer, where both terms in (I.1) are small. Below the confinement layer, the most significant departures from magnetostrophic balance are associated with viscous

¹Figure I.2 shows the entire numerical domain, whereas the cross-section in figure 7.2 was truncated at $z = 5$.

angular-momentum exchange between the poloidal magnetic flux surfaces.

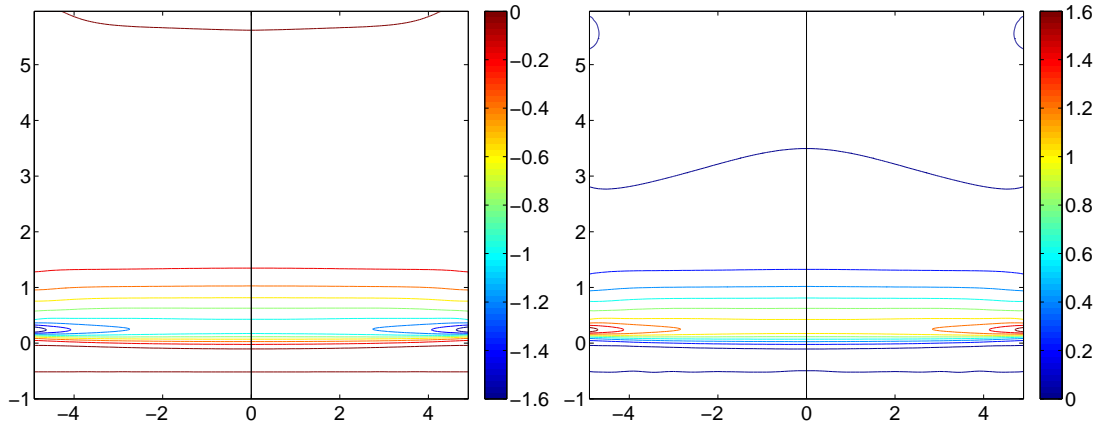


Figure I.2: Contours of the first and second terms in (I.1), in a vertical cross-section through a numerical solution. Both terms are largest in magnitude within the confinement layer.

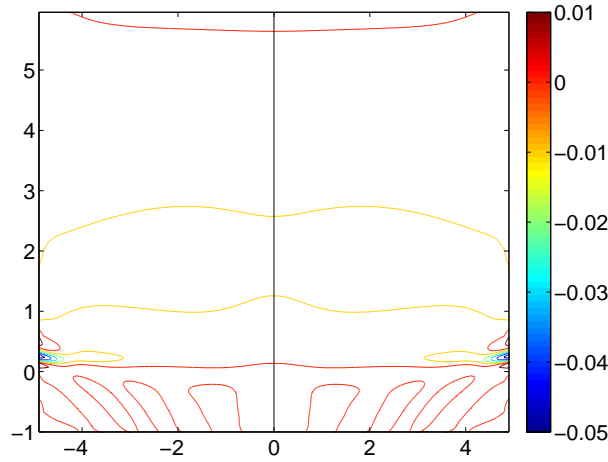


Figure I.3: Contours of the total right-hand side of (I.1), representing departures from magnetostrophic balance.

I.3 Numerical boundaries

I.3.1 The upper boundary

In the numerical solution presented in figure 7.2, the boundary condition

$$\partial B_z / \partial z = -B_z \quad (\text{I.2})$$

was imposed at the top of the domain (see §10.3) in order to mimic the presence of an exponential tail in the layers above. Contours of B_z in a vertical cross-section through that solution are presented in figure I.4. To verify that the solution is not sensitive to this particular choice of boundary condition, we have also computed a solution with the condition $B_z = 0$, instead of (I.2), imposed at the top of the domain, but with all other boundary conditions unchanged. Figure I.4 presents contours of the difference in B_z between the two solutions. As expected, the effect of the change in the upper boundary condition is localised to the region close to the upper boundary, and is small in magnitude.

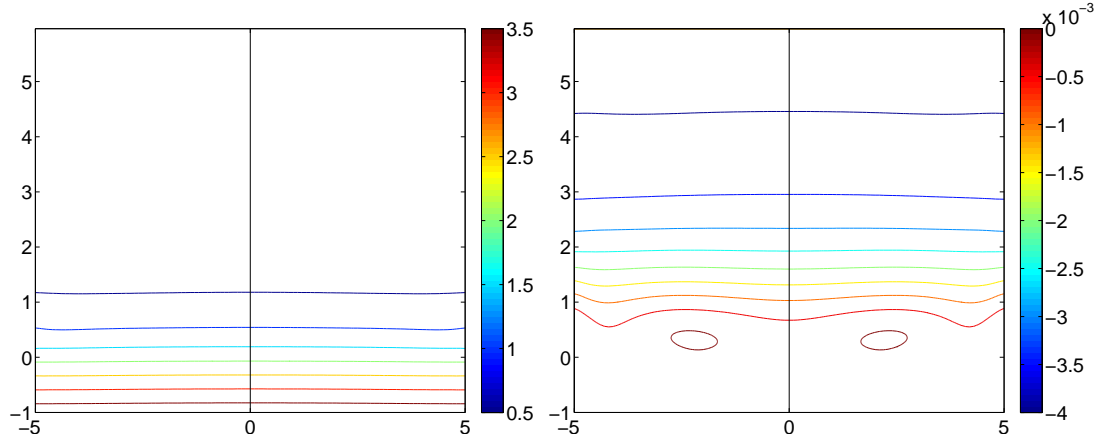


Figure I.4: The effect of changing the upper boundary condition on B_z . The left panel shows contours of B_z obtained when matching on to an exponentially decaying profile above (see §10.3). The right panel shows the change in B_z when, instead, a vanishing field is imposed above.

I.3.2 Boundary locations

Since the boundaries of the numerical domain are artificial, we should check that their exact locations do not significantly affect the solutions. In figure I.5 we show the result of shifting the domain vertically. The left-hand plot shows the streamlines, magnetic field lines and compositional stratification in a vertical cross-section through the same solution presented in figure 7.2. The right-hand plot shows an equivalent cross-section through a solution in which the numerical domain was shifted downward by a dimensionless distance of 0.5, i.e. $0.5\delta_\eta$, via a suitable translation of the peripheral boundary conditions. The solution is found to be entirely robust to the vertical shift of the numerical domain.

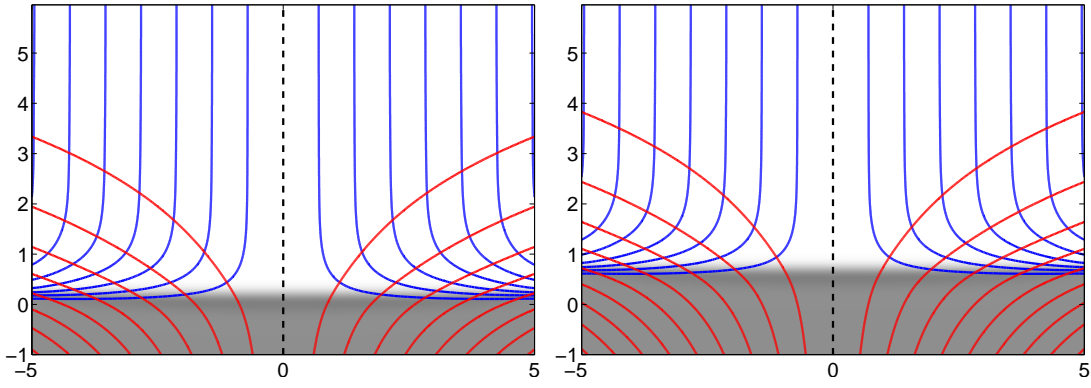


Figure I.5: Shifting the numerical domain downward does not significantly affect the solution. The velocity streamlines and magnetic field lines are shown in blue and red respectively. The shading indicates compositional stratification, $\partial\mu/\partial z$.

I.4 Horizontal resolution

As mentioned in appendix H, the constraints on the vertical grid interval Δz are stronger than the constraints on the horizontal grid interval Δr , due to the thinness of the helium sublayer. The numerical solution presented in figure 7.2 has $\Delta z = 0.01$ and $\Delta r = 0.1$. To check that the relatively coarse horizontal resolution does not qualitatively affect the numerical results, we have also computed a solution with $\Delta r = 0.05$, in a domain with cylindrical radius $r_d = 2.5$. The peripheral boundary profiles $T(z)$, $\mu(z)$ and $B_\phi(z)$ in this solution were taken from the original, wider solution at $r = 2.5$. In figure I.6 we plot contours of B_ϕ/r from both solutions. Although the two solutions are not identical, the differences between the two are small.

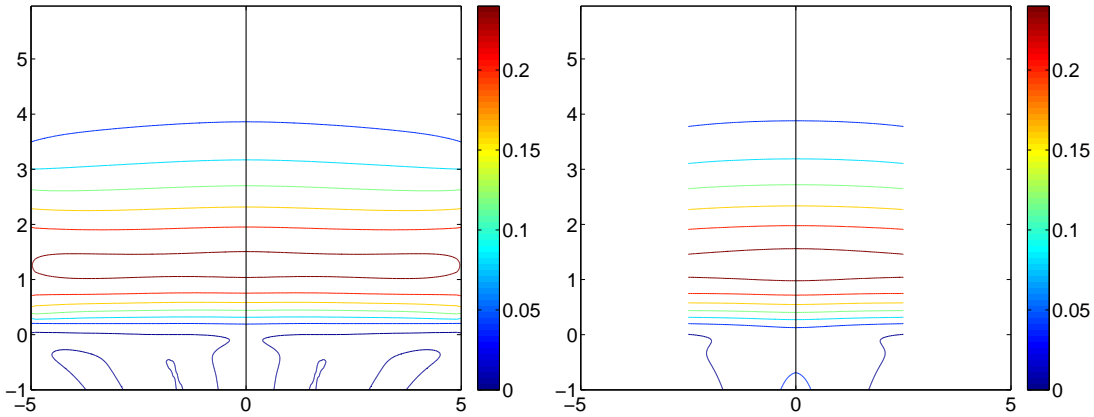


Figure I.6: The influence of horizontal resolution on the numerical solutions. The left panel shows contours of B_ϕ/r in a solution with $\Delta r = 0.1$ and $r_d = 5$. The right panel shows contours of B_ϕ/r in a solution with $\Delta r = 0.05$ and $r_d = 2.5$.

I.5 Horizontal diffusion

The increased horizontal diffusivities ν_H and χ_H , introduced for numerical stability, undoubtedly have an effect on the numerical solutions. We would like to quantify this effect, in order to ensure that the solutions do not depend significantly on the values of ν_H and χ_H chosen. In figure I.7 we present the rotation profile u_ϕ/r in a vertical cross-section through the numerical solution described in §I.4, which has $\Delta r = 0.05$, $r_d = 2.5$ and $\nu_H = \chi_H = 10$. We also present the rotation profile in a solution that has $\nu_H = \chi_H = 5$ but is otherwise identical. The most noticeable differences between the two solutions are in the upper part of the domain, where magnetostrophic balance becomes delicate (§I.2) and diffusion of angular momentum therefore becomes increasingly significant. Nonetheless, changing the horizontal diffusivities does not qualitatively affect the structure of the confinement layer.

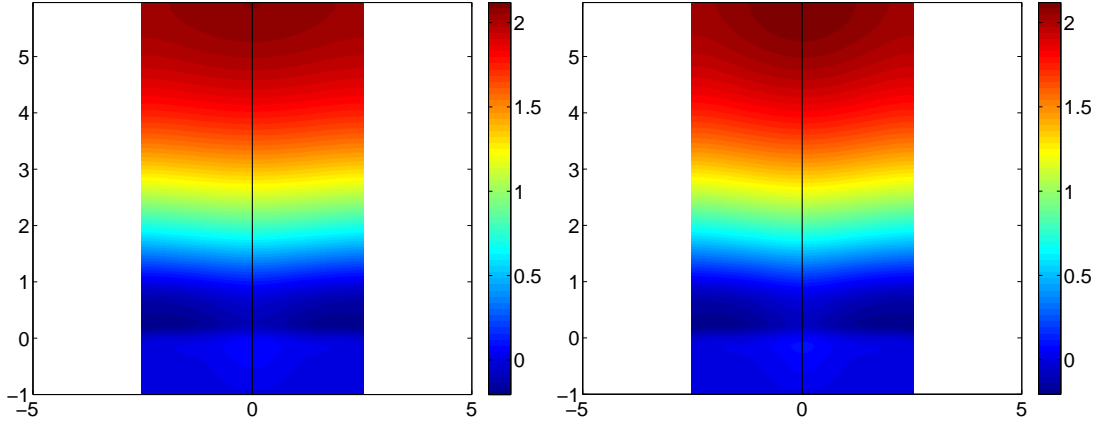


Figure I.7: The rotation profile u_ϕ/r in two numerical solutions. The left panel has $\nu_H = \chi_H = 10$; the right panel has $\nu_H = \chi_H = 5$. The two solutions have identical boundary conditions.

Bibliography

- ALFVÉN, H. 1942 Existence of electromagnetic-hydrodynamic waves. *Nature* **150**, 405–406.
- ANDREWS, D. G., HOLTON, J. R. & LEOVY, C. B. 1987 *Middle atmosphere dynamics*. New York: Academic Press.
- ANTIA, H. M. & BASU, S. 2000 Temporal variations of the rotation rate in the solar interior. *Astrophys. J.* **541**, 442–448.
- APPOURCHAUX, T., BELKACEM, K., BROOMHALL, A.-M., CHAPLIN, W. J., GOUGH, D. O., HOUDEK, G., PROVOST, J., BAUDIN, F., BOUMIER, P., ELSWORTH, Y., GARCÍA, R. A., ANDERSEN, B. N., FINSTERLE, W., FRÖHLICH, C., GABRIEL, A., GREC, G., JIMÉNEZ, A., KOSOVICHEV, A., SEKII, T., TOUTAIN, T. & TURCK-CHIÈZE, S. 2010 The quest for the solar g modes. *A&A Rev.* **18**, 197–277.
- ASPLUND, M. 2005 New light on stellar abundance analyses: departures from LTE and homogeneity. *Annu. Rev. Astron. Astrophys.* **43**, 481–530.
- ASPLUND, M., GREVESSE, N. & SAUVAL, A. J. 2006 The new solar abundances — Part I: the observations. *Communications in Asteroseismology* **147**, 76–79.
- ASPLUND, M., GREVESSE, N., SAUVAL, A. J. & SCOTT, P. 2009 The chemical composition of the Sun. *Annu. Rev. Astron. Astrophys.* **47**, 481–522.
- AURNOU, J., HEIMPEL, M. & WICHT, J. 2007 The effects of vigorous mixing in a convective model of zonal flow on the ice giants. *Icarus* **190**, 110–126.
- BABCOCK, H. W. 1961 The topology of the Sun’s magnetic field and the 22-year cycle. *Astrophys. J.* **133**, 572–587.

- BADNELL, N. R., BAUTISTA, M. A., BUTLER, K., DELAHAYE, F., MENDOZA, C., PALMERI, P., ZEIPPEN, C. J. & SEATON, M. J. 2005 Updated opacities from the Opacity Project. *MNRAS* **360**, 458–464.
- BAHCALL, J. N., BASU, S. & SERENELLI, A. M. 2005 What is the neon abundance of the Sun? *Astrophys. J.* **631**, 1281–1285.
- BAHCALL, J. N. & PINSONNEAULT, M. H. 2004 What do we (not) know theoretically about solar neutrino fluxes? *Phys. Rev. Lett.* **92** (12), 121301.
- BAHCALL, J. N. & SERENELLI, A. M. 2005 How do uncertainties in the surface chemical composition of the Sun affect the predicted solar neutrino fluxes? *Astrophys. J.* **626**, 530–542.
- BARCILON, V. & PEDLOSKY, J. 1967 A unified linear theory of homogeneous and stratified rotating fluids. *J. Fluid Mech.* **29**, 609–621.
- BASU, S. & ANTIA, H. M. 1995 Helium abundance in the solar envelope. *MNRAS* **276**, 1402–1408.
- BASU, S. & ANTIA, H. M. 2003 Changes in solar dynamics from 1995 to 2002. *Astrophys. J.* **585**, 553–565.
- BASU, S. & ANTIA, H. M. 2004 Constraining solar abundances using helioseismology. *Astrophys. J.* **606**, L85–L88.
- BOESGAARD, A. M. & TRIPICCO, M. J. 1986 Lithium in the Hyades Cluster. *Astrophys. J.* **302**, L49–L53.
- BÖHM-VITENSE, E. 1958 Über die Wasserstoffkonvektionszone in Sternen verschiedener Effektivtemperaturen und Leuchtkräfte. Mit 5 Textabbildungen. *Zeitschrift für Astrophysik* **46**, 108–143.
- BOUVIER, J., ALENCAR, S. H. P., HARRIES, T. J., JOHNS-KRULL, C. M. & ROMANOVA, M. M. 2007 Magnetospheric accretion in classical T Tauri stars. In *Protostars and Planets V* (ed. B. Reipurth, D. Jewitt, & K. Keil), pp. 479–494. Tuscon: Univ. Arizona Press.
- BRAITHWAITE, J. & NORDLUND, Å. 2006 Stable magnetic fields in stellar interiors. *A&A* **450**, 1077–1095.

- BRAITHWAITE, J. & SPRUIT, H. C. 2004 A fossil origin for the magnetic field in A stars and white dwarfs. *Nature* **431**, 819–821.
- BRETHERTON, F. P. & SPIEGEL, A. E. 1968 The effect of the convection zone on solar spin-down. *Astrophys. J.* **153**, L77–L80.
- BRUMMELL, N. H., CLUNE, T. L. & TOOMRE, J. 2002 Penetration and overshooting in turbulent compressible convection. *Astrophys. J.* **570**, 825–854.
- BRUN, A. S. & ZAHN, J.-P. 2006 Magnetic confinement of the solar tachocline. *A&A* **457**, 665–674.
- BUSSE, F. H. & HOOD, L. L. 1982 Differential rotation driven by convection in a rapidly rotating annulus. *Geophys. Astrophys. Fluid Dyn.* **21**, 59–74.
- CATTANEO, F., BRUMMELL, N. H., TOOMRE, J., MALAGOLI, A. & HURLBURT, N. E. 1991 Turbulent compressible convection. *Astrophys. J.* **370**, 282–294.
- CATTANEO, F. & HUGHES, D. W. 1996 Nonlinear saturation of the turbulent α effect. *Phys. Rev. E* **54**, 4532–4535.
- CHANDRASEKHAR, S. & PRENDERGAST, K. H. 1956 The equilibrium of magnetic stars. *Proceedings of the National Academy of Science* **42**, 5–9.
- CHARBONNEAU, P., BEAUBIEN, G. & ST-JEAN, C. 2007 Fluctuations in Babcock–Leighton dynamos. II. Revisiting the Gnevyshev–Ohl rule. *Astrophys. J.* **658**, 657–662.
- CHARBONNEAU, P. & MACGREGOR, K. B. 1993 Angular momentum transport in magnetized stellar radiative zones. II. The solar spin-down. *Astrophys. J.* **417**, 762.
- CHARBONNEAU, P. & MACGREGOR, K. B. 1997 Solar interface dynamos. II. Linear, kinematic models in spherical geometry. *Astrophys. J.* **486**, 502–520.
- CHARBONNEL, C. & TALON, S. 2005 Influence of gravity waves on the internal rotation and Li abundance of solar-type stars. *Science* **309**, 2189–2191.

- CHARBONNEL, C. & TALON, S. 2007 On internal gravity waves in low-mass stars. In *Unsolved Problems in Stellar Physics: A Conference in Honor of Douglas Gough* (ed. R. J. Stancliffe, J. Dewi, G. Houdek, R. G. Martin, & C. A. Tout), *American Institute of Physics Conference Series*, vol. 948, pp. 15–26.
- CHARBONNEL, C., VAUCLAIR, S. & ZAHN, J.-P. 1992 Rotation-induced mixing and lithium depletion in galactic clusters. *A&A* **255**, 191–199.
- CHEN, Y. Q., NISSEN, P. E., BENONI, T. & ZHAO, G. 2001 Lithium abundances for 185 main-sequence stars: Galactic evolution and stellar depletion of lithium. *A&A* **371**, 943–951.
- CHRISTENSEN-DALSGAARD, J. 2002 Helioseismology. *Reviews of Modern Physics* **74**, 1073–1129.
- CHRISTENSEN-DALSGAARD, J. & DI MAURO, M. P. 2007 Diffusion and helioseismology. In *Stellar Evolution and Seismic Tools for Asteroseismology — Diffusive Processes in Stars and Seismic Analysis* (ed. C. W. Straka, Y. Lebreton, & M. J. P. F. G. Monteiro), *EAS Publications Series*, vol. 26, pp. 3–16.
- CHRISTENSEN-DALSGAARD, J., DI MAURO, M. P., HOUDEK, G. & PIJPERS, F. 2009 On the opacity change required to compensate for the revised solar composition. *A&A* **494**, 205–208.
- CHRISTENSEN-DALSGAARD, J., GOUGH, D. O. & THOMPSON, M. J. 1991 The depth of the solar convection zone. *Astrophys. J.* **378**, 413–437.
- CHRISTENSEN-DALSGAARD, J., GOUGH, D. O. & THOMPSON, M. J. 1992 On the rate of destruction of lithium in late-type main-sequence stars. *A&A* **264**, 518–528.
- CHRISTENSEN-DALSGAARD, J., PROFFITT, C. R. & THOMPSON, M. J. 1993 Effects of diffusion on solar models and their oscillation frequencies. *Astrophys. J.* **403**, L75–L78.

- CHRISTENSEN-DALSGAARD, J. & THOMPSON, M. J. 2007 Observational results and issues concerning the tachocline. In *The Solar Tachocline* (ed. D. W. Hughes, R. Rosner, & N. O. Weiss), p. 53.
- CHRISTIAN, D. J. & MATHIOUDAKIS, M. 2000 Is Lithium produced in active stellar atmospheres? In *NOAO Proposal ID #2000B-0165*, p. 165.
- CIACIO, F., DEGL'INNOCENTI, S. & RICCI, B. 1997 Updating standard solar models. *A&AS* **123**, 449–454.
- CLARK, A. 1973 The linear spin-up of a strongly stratified fluid of small Prandtl number. *J. Fluid Mech.* **60**, 561–580.
- CLARK, A. 1975 Time scales in stellar spin-down. *Mémoires Société Royale des Sciences de Liège* **8**, 43–46.
- CLAVERIE, A., ISAAK, G. R., MCLEOD, C. P., VAN DER RAAY, H. B. & ROCA CORTES, T. 1981 Rapid rotation of the solar interior. *Nature* **293**, 443–445.
- COWLING, T. G. 1933 The magnetic field of sunspots. *MNRAS* **94**, 39–48.
- CRAIK, A. D. D. 1988 A class of exact solutions in viscous incompressible magnetohydrodynamics. *Proc. R. Soc. Lond. A* **417**, 235–244.
- DE JAGER, C. 1972 Micro- and macroturbulent motions and the velocity spectrum of the solar photosphere. *Sol. Phys.* **25**, 71–80.
- DEBNATH, L. 1973 On Ekman and Hartmann boundary layers in a rotating fluid. *Acta Mechanica* **18**, 333–341.
- DENISENKOV, P. A. & PINSONNEAULT, M. 2007 A revised prescription for the Tayler–Spruit dynamo: magnetic angular momentum transport in stars. *Astrophys. J.* **655**, 1157–1165.
- DIKPATI, M. & CHARBONNEAU, P. 1999 A Babcock–Leighton flux transport dynamo with solar-like differential rotation. *Astrophys. J.* **518**, 508–520.
- DINTRANS, B., BRANDENBURG, A., NORDLUND, Å. & STEIN, R. F. 2005 Spectrum and amplitudes of internal gravity waves excited by penetrative convection in solar-type stars. *A&A* **438**, 365–376.

- DORCH, S. B. F. & NORDLUND, Å. 2001 On the transport of magnetic fields by solar-like stratified convection. *A&A* **365**, 562–570.
- DRITSCHEL, D. G. 1991 Generalized helical Beltrami flows in hydrodynamics and magnetohydrodynamics. *J. Fluid Mech.* **222**, 525–541.
- DROBYSHEVSKI, E. M. & YUFEREV, V. S. 1974 Topological pumping of magnetic flux by three-dimensional convection. *J. Fluid Mech.* **65**, 33–44.
- ELLIOTT, J. R. 1997 Aspects of the solar tachocline. *A&A* **327**, 1222–1229.
- ELLIOTT, J. R. & GOUGH, D. O. 1999 Calibration of the thickness of the solar tachocline. *Astrophys. J.* **516**, 475–481.
- FEAST, M. W. 1966 Lithium in β Hydri and other stars. *MNRAS* **134**, 321–326.
- FERRARO, V. C. A. 1937 The non-uniform rotation of the Sun and its magnetic field. *MNRAS* **97**, 458–472.
- FRITTS, D. C., VADAS, S. L. & ANDREASSEN, O. 1998 Gravity wave excitation and momentum transport in the solar interior: implications for a residual circulation and lithium depletion. *A&A* **333**, 343–361.
- GAIDOS, E. J. 1998 Nearby young solar analogs. I. Catalog and stellar characteristics. *PASP* **110**, 1259–1276.
- GARAUD, P. 2001 Latitudinal shear instability in the solar tachocline. *MNRAS* **324**, 68–76.
- GARAUD, P. 2002 Dynamics of the solar tachocline — I. An incompressible study. *MNRAS* **329**, 1–17.
- GARAUD, P. & ACEVEDO ARREGUIN, L. 2009 On the penetration of meridional circulation below the solar convection zone. II. Models with convection zone, the Taylor–Proudman constraint, and applications to other stars. *Astrophys. J.* **704**, 1–16.
- GARAUD, P. & BRUMMELL, N. H. 2008 On the penetration of meridional circulation below the solar convection zone. *Astrophys. J.* **674**, 498–510.

- GARAUD, P. & GARAUD, J.-D. 2008 Dynamics of the solar tachocline — II. The stratified case. *MNRAS* **391**, 1239–1258.
- GARAUD, P. & ROGERS, T. 2007 Solar rotation. In *Unsolved Problems in Stellar Physics: A Conference in Honor of Douglas Gough* (ed. R. J. Stancliffe, J. Dewi, G. Houdek, R. G. Martin, & C. A. Tout), *American Institute of Physics Conference Series*, vol. 948, pp. 237–248.
- GARCÍA LÓPEZ, R. J. & SPRUIT, H. C. 1991 Li depletion in F stars by internal gravity waves. *Astrophys. J.* **377**, 268–277.
- GILMAN, P. A. 1977 Nonlinear dynamics of Boussinesq convection in a deep rotating spherical shell. I. *Geophys. Astrophys. Fluid Dyn.* **8**, 93–135.
- GILMAN, P. A. & CALLY, P. S. 2007 Global MHD instabilities of the tachocline. In *The Solar Tachocline* (ed. D. W. Hughes, R. Rosner, & N. O. Weiss), p. 243.
- GILMAN, P. A. & MIESCH, M. S. 2004 Limits to penetration of meridional circulation below the solar convection zone. *Astrophys. J.* **611**, 568–574.
- GILMAN, P. A. & MILLER, J. 1981 Dynamically consistent nonlinear dynamos driven by convection in a rotating spherical shell. *ApJS* **46**, 211–238.
- GLATZMAIER, G., EVONU, M. & ROGERS, T. 2009 Differential rotation in giant planets maintained by density-stratified turbulent convection. *Geophys. Astrophys. Fluid Dyn.* **103**, 31–51.
- GOUGH, D. 2007 An introduction to the solar tachocline. In *The Solar Tachocline* (ed. D. W. Hughes, R. Rosner, & N. O. Weiss), p. 3.
- GOUGH, D. O. 1969 The anelastic approximation for thermal convection. *J. Atmos. Sci.* **26**, 448–456.
- GOUGH, D. O. & MCINTYRE, M. E. 1998 Inevitability of a magnetic field in the Sun’s radiative interior. *Nature* **394**, 755–757.
- GREENSPAN, H. P. 1968 *The theory of rotating fluids*. Cambridge: University Press.

- GREVESSE, N., ASPLUND, M. & SAUVAL, A. J. 2007 The solar chemical composition. *Space Sci. Rev.* **130**, 105–114.
- GREVESSE, N. & SAUVAL, A. J. 1998 Standard solar composition. *Space Sci. Rev.* **85**, 161–174.
- GUZIK, J. A., WILLSON, L. A. & BRUNISH, W. M. 1987 A comparison between mass-losing and standard solar models. *Astrophys. J.* **319**, 957–965.
- HALE, G. E. 1908 On the probable existence of a magnetic field in sun-spots. *Astrophys. J.* **28**, 315–343.
- HALE, G. E., ELLERMAN, F., NICHOLSON, S. B. & JOY, A. H. 1919 The magnetic polarity of sun-spots. *Astrophys. J.* **49**, 153–178.
- HAYNES, P. H., MCINTYRE, M. E., SHEPHERD, T. G., MARKS, C. J. & SHINE, K. P. 1991 On the ‘downward control’ of extratropical diabatic circulations by eddy-induced mean zonal forces. *J. Atmos. Sci.* **48**, 651–680.
- HOLTON, J. R. 1965 The influence of viscous boundary layers on transient motions in a stratified rotating fluid. Part I. *J. Atmos. Sci.* **22**, 402–411.
- HOLWEGGER, H. & MÜLLER, E. A. 1974 The photospheric barium spectrum — Solar abundance and collision broadening of BA II lines by hydrogen. *Sol. Phys.* **39**, 19–30.
- HOWARD, R. & LABONTE, B. J. 1980 The Sun is observed to be a torsional oscillator with a period of 11 years. *Astrophys. J.* **239**, L33–L36.
- HOWE, R. 2009 Solar interior rotation and its variation. *Living Reviews in Solar Physics* **6**, 1.
- HOWE, R., CHRISTENSEN-DALSGAARD, J., HILL, F., KOMM, R., SCHOU, J., THOMPSON, M. J. & TOOMRE, J. 2007 Temporal variations in solar rotation at the bottom of the convection zone: The current status. *Advances in Space Research* **40**, 915–918.
- HOWE, R., CHRISTENSEN-DALSGAARD, J., HILL, F., KOMM, R. W., LARSEN, R. M., SCHOU, J., THOMPSON, M. J. & TOOMRE, J. 2000 Dy-

- dynamic variations at the base of the solar convection zone. *Science* **287**, 2456–2460.
- HURLBURT, N. E., TOOMRE, J. & MASSAGUER, J. M. 1986 Nonlinear compressible convection penetrating into stable layers and producing internal gravity waves. *Astrophys. J.* **311**, 563–577.
- IBEN, JR., I. 1965 Stellar evolution. I. The approach to the main sequence. *Astrophys. J.* **141**, 993–1018.
- ISRAELIAN, G., DELGADO MENA, E., SANTOS, N. C., SOUSA, S. G., MAYOR, M., UDRY, S., DOMÍNGUEZ CERDEÑA, C., REBOLO, R. & RANDICH, S. 2009 Enhanced lithium depletion in Sun-like stars with orbiting planets. *Nature* **462**, 189–191.
- KÄHLER, H. 1978 The Vogt-Russell theorem, and new results on an old problem. In *The HR Diagram — The 100th Anniversary of Henry Norris Russell* (ed. A. G. D. Philip & D. S. Hayes), *IAU Symposium*, vol. 80, pp. 303–311.
- KING, E. M., STELLMACH, S., NOIR, J., HANSEN, U. & AURNou, J. M. 2009 Boundary layer control of rotating convection systems. *Nature* **457**, 301–304.
- KITCHATINOV, L. L. & RÜDIGER, G. 1992 Magnetic-field advection in inhomogeneous turbulence. *A&A* **260**, 494–498.
- KITCHATINOV, L. L. & RÜDIGER, G. 1995 Differential rotation in solar-type stars: revisiting the Taylor-number puzzle. *A&A* **299**, 446–452.
- KITCHATINOV, L. L. & RÜDIGER, G. 2006 Magnetic field confinement by meridional flow and the solar tachocline. *A&A* **453**, 329–333.
- KITCHATINOV, L. L. & RÜDIGER, G. 2008 Diamagnetic pumping near the base of a stellar convection zone. *Astron. Nachr.* **329**, 372–375.
- KRAUSE, F. & RÄDLER, K.-H. 1980 *Mean-field magnetohydrodynamics and dynamo theory*. Oxford: Pergamon Press.
- LARMOR, J. 1919 How could a rotating body such as the Sun become a magnet? *Rep. Brit. Assoc. Adv. Sci.* p. 159.

- LEIGHTON, R. B. 1969 A magneto-kinematic model of the solar cycle. *Astrophys. J.* **156**, 1–26.
- LEVY, E. H. & BOYER, D. 1982 Oscillating dynamo in the presence of a fossil magnetic field — The solar cycle. *Astrophys. J.* **254**, L19–L22.
- LINEYKIN, P. C. 1955 On the determination of the thickness of the baroclinic layer in the ocean. *Dokl. Akad. Nauk. SSSR* **101**, 461–464.
- MACGREGOR, K. B. & CHARBONNEAU, P. 1999 Angular momentum transport in magnetized stellar radiative zones. IV. Ferraro’s theorem and the solar tachocline. *Astrophys. J.* **519**, 911–917.
- MALKUS, W. V. R. 1967 Hydromagnetic planetary waves. *J. Fluid Mech.* **28**, 793–802.
- MATHIS, S. 2009 Transport by gravito-inertial waves in differentially rotating stellar radiation zones. I — Theoretical formulation. *A&A* **506**, 811–828.
- MCINTYRE, M. 1994 The quasi-biennial oscillation (QBO) : some points about the terrestrial QBO and the possibility of related phenomena in the solar interior. In *The Solar Engine and its Influence on Terrestrial Atmosphere and Climate* (ed. E. Nesme-Ribes), p. 293.
- MCINTYRE, M. E. 2003 Solar tachocline dynamics: eddy viscosity, anti-friction, or something in between? In *Stellar astrophysical fluid dynamics* (ed. Thompson, M. J. & Christensen-Dalsgaard, J.), pp. 111–130. Cambridge: University Press.
- MCINTYRE, M. E. 2007 Magnetic confinement and the sharp tachopause. In *The Solar Tachocline* (ed. D. W. Hughes, R. Rosner, & N. O. Weiss), p. 183.
- MESTEL, L. 1953 Rotation and stellar evolution. *MNRAS* **113**, 716–745.
- MESTEL, L. & MOSS, D. L. 1986 On mixing by the Eddington–Sweet circulation. *MNRAS* **221**, 25–51.
- MESTEL, L. & WEISS, N. O. 1987 Magnetic fields and non-uniform rotation in stellar radiative zones. *MNRAS* **226**, 123–135.

- MICHAUD, G. 1986 The lithium abundance gap in the Hyades F stars — The signature of diffusion. *Astrophys. J.* **302**, 650–655.
- MICHAUD, G. & CHARBONNEAU, P. 1991 The lithium abundance in stars. *Space Sci. Rev.* **57**, 1–58.
- MICHAUD, G. & PROFFITT, C. R. 1993 Particle transport processes. In *IAU Colloq. 137: Inside the Stars* (ed. W. W. Weiss & A. Baglin), *Astronomical Society of the Pacific Conference Series*, vol. 40, pp. 246–259.
- MIESCH, M. S. 2005 Large-scale dynamics of the convection zone and tachocline. *Living Reviews in Solar Physics* **2**, 1.
- MIESCH, M. S., BRUN, A. S. & TOOMRE, J. 2006 Solar differential rotation influenced by latitudinal entropy variations in the tachocline. *Astrophys. J.* **641**, 618–625.
- MIESCH, M. S., ELLIOTT, J. R., TOOMRE, J., CLUNE, T. L., GLATZMAIER, G. A. & GILMAN, P. A. 2000 Three-dimensional spherical simulations of solar convection. I. Differential rotation and pattern evolution achieved with laminar and turbulent states. *Astrophys. J.* **532**, 593–615.
- MOFFATT, H. K. 1978 *Magnetic field generation in electrically conducting fluids*. Cambridge: University Press.
- MONTALBÁN, J., MIGLIO, A., NOELS, A., GREVESSE, N. & DI MAURO, M. P. 2004 Solar model with CNO revised abundances. In *SOHO 14 Helio- and Asteroseismology: Towards a Golden Future* (ed. D. Danesy), *ESA Special Publication*, vol. 559, pp. 574–576.
- MONTALBÁN, J., MIGLIO, A., THEADO, S., NOELS, A. & GREVESSE, N. 2006 The new solar abundances — Part II: the crisis and possible solutions. *Communications in Asteroseismology* **147**, 80–84.
- MURSULA, K., USOSKIN, I. G. & KOVALTSOV, G. A. 2001 Persistent 22-year cycle in sunspot activity: Evidence for a relic solar magnetic field. *Sol. Phys.* **198**, 51–56.

- OGILVIE, G. I. 2007 Instabilities, angular momentum transport and magnetohydrodynamic turbulence. In *The Solar Tachocline* (ed. D. W. Hughes, R. Rosner, & N. O. Weiss), p. 299.
- PARFREY, K. P. & MENOU, K. 2007 The origin of solar activity in the tachocline. *Astrophys. J.* **667**, L207–L210.
- PARKER, E. N. 1955*a* Hydromagnetic dynamo models. *Astrophys. J.* **122**, 293–314.
- PARKER, E. N. 1955*b* The formation of sunspots from the solar toroidal field. *Astrophys. J.* **121**, 491–507.
- PARKER, E. N. 1975 The generation of magnetic fields in astrophysical bodies. X — Magnetic buoyancy and the solar dynamo. *Astrophys. J.* **198**, 205–209.
- PARKER, E. N. 1981 Residual fields from extinct dynamos. *Geophys. Astrophys. Fluid Dyn.* **18**, 175–196.
- PARKER, E. N. 1993 A solar dynamo surface wave at the interface between convection and nonuniform rotation. *Astrophys. J.* **408**, 707–719.
- PEDLOSKY, J. 1979 *Geophysical fluid dynamics*. New York: Springer-Verlag.
- PINSONNEAULT, M. H. & DELAHAYE, F. 2009 The solar heavy element abundances. II. Constraints from stellar atmospheres. *Astrophys. J.* **704**, 1174–1188.
- PINSONNEAULT, M. H., DEPOY, D. L. & COFFEE, M. 2001 The mass of the convective zone in FGK main-sequence stars and the effect of accreted planetary material on apparent metallicity determinations. *Astrophys. J.* **556**, L59–L62.
- PITTS, E. & TAYLER, R. J. 1985 The adiabatic stability of stars containing magnetic fields. IV — The influence of rotation. *MNRAS* **216**, 139–154.
- PLUMPTON, C. & FERRARO, V. C. A. 1955 On toroidal magnetic fields in the Sun and stars. *Astrophys. J.* **121**, 168–174.
- PRENDERGAST, K. H. 1956 The equilibrium of a self-gravitating incompressible fluid sphere with a magnetic field. I. *Astrophys. J.* **123**, 498–507.

- PRESS, W. H., FLANNERY, B. P., TEUKOLSKY, S. A. & VETTERLING, W. T. 1986 *Numerical recipes. The art of scientific computing*. Cambridge: University Press.
- PROFFITT, C. R. & MICHAUD, G. 1991 Diffusion and mixing of lithium and helium in population II dwarfs. *Astrophys. J.* **371**, 584–601.
- RÄDLER, K. H. 1968 On the electrodynamics of conducting fluids in turbulent motion. II. Turbulent conductivity and turbulent permeability. *Zeitschrift Naturforschung Teil A* **23**, 1851–1860.
- REMPEL, M. 2005 Solar differential rotation and meridional flow: The role of a subadiabatic tachocline for the Taylor–Proudman balance. *Astrophys. J.* **622**, 1320–1332.
- ROBERTS, P. H. & SOWARD, A. M. 1975 A unified approach to mean field electrodynamics. *Astron. Nachr.* **296**, 49–64.
- ROGERS, T. M. & GLATZMAIER, G. A. 2006 Angular momentum transport by gravity waves in the solar interior. *Astrophys. J.* **653**, 756–764.
- ROGERS, T. M., MACGREGOR, K. B. & GLATZMAIER, G. A. 2008 Non-linear dynamics of gravity wave driven flows in the solar radiative interior. *MNRAS* **387**, 616–630.
- ROSSBY, C. G. 1938 On the mutual adjustment of pressure and velocity distributions in certain simple current systems, II. *J. Mar. Res.* **1**, 239–263.
- RÜDIGER, G. & KITCHATINOV, L. L. 1997 The slender solar tachocline: a magnetic model. *Astron. Nachr.* **318**, 273–279.
- RÜDIGER, G., KITCHATINOV, L. L. & ARLT, R. 2005 The penetration of meridional flow into the tachocline and its meaning for the solar dynamo. *A&A* **444**, L53–L56.
- SCHATZMAN, E. 1962 A theory of the role of magnetic activity during star formation. *Annales d’Astrophysique* **25**, 18–29.
- SCHATZMAN, E. 1993 Transport of angular momentum and diffusion by the action of internal waves. *A&A* **279**, 431–446.

- SCHMITT, D. 1993 The solar dynamo. In *The Cosmic Dynamo* (ed. F. Krause, K. H. Rädler, & G. Rüdiger), *IAU Symposium*, vol. 157, pp. 1–12.
- SCHOU, J., ANTIA, H. M., BASU, S., BOGART, R. S., BUSH, R. I., CHITRE, S. M., CHRISTENSEN-DALSGAARD, J., DI MAURO, M. P., DZIEMBOWSKI, W. A., EFF-DARWICH, A., GOUGH, D. O., HABER, D. A., HOEKSEMA, J. T., HOWE, R., KORZENNIK, S. G., KOSOVICHEV, A. G., LARSEN, R. M., PIJPERS, F. P., SCHERRER, P. H., SEKII, T., TARBELL, T. D., TITTE, A. M., THOMPSON, M. J. & TOOMRE, J. 1998 Helioseismic studies of differential rotation in the solar envelope by the Solar Oscillations Investigation using the Michelson Doppler Imager. *Astrophys. J.* **505**, 390–417.
- SODERBLOM, D. R., OEY, M. S., JOHNSON, D. R. H. & STONE, R. P. S. 1990 The evolution of the lithium abundances of solar-type stars. I — The Hyades and Coma Berenices clusters. *AJ* **99**, 595–607.
- SPIEGEL, E. A. 1972 A history of solar rotation. *NASA Special Publication* **300**, 61.
- SPIEGEL, E. A. & WEISS, N. O. 1980 Magnetic activity and variations in solar luminosity. *Nature* **287**, 616–617.
- SPIEGEL, E. A. & ZAHN, J.-P. 1992 The solar tachocline. *A&A* **265**, 106–114.
- SPRUIT, H. C. 1999 Differential rotation and magnetic fields in stellar interiors. *A&A* **349**, 189–202.
- SPRUIT, H. C. 2002 Dynamo action by differential rotation in a stably stratified stellar interior. *A&A* **381**, 923–932.
- STEENBECK, M. & KRAUSE, F. 1969 Zur Dynamotheorie stellarer und planetarer Magnetfelder I. Berechnung sonnenähnlicher Wechselfeldgeneratoren. *Astron. Nachr.* **291**, 49–84.
- STEENBECK, M., KRAUSE, F. & RÄDLER, K.-H. 1966 A calculation of the mean electromotive force in an electrically conducting fluid in turbulent motion, under the influence of Coriolis forces. *Zeitschrift Naturforschung Teil A* **21**, 369.
- STEIN, R. F. & NORDLUND, Å. 1998 Simulations of solar granulation. I. General properties. *Astrophys. J.* **499**, 914–933.

- STRÖMGREN, B. 1938 On the helium and hydrogen content of the interior of the stars. *Astrophys. J.* **87**, 520–534.
- SWENSON, F. J. & FAULKNER, J. 1992 Lithium dilution through main-sequence mass loss. *Astrophys. J.* **395**, 654–674.
- TALON, S., KUMAR, P. & ZAHN, J.-P. 2002 Angular momentum extraction by gravity waves in the Sun. *Astrophys. J.* **574**, L175–L178.
- TAO, L., PROCTOR, M. R. E. & WEISS, N. O. 1998 Flux expulsion by inhomogeneous turbulence. *MNRAS* **300**, 907–914.
- TASSOUL, J.-L. & TASSOUL, M. 1986 On the nature of the core-envelope boundary layer in a slowly rotating star. *Geophys. Astrophys. Fluid Dyn.* **36**, 303–315.
- TAYLOR, J. B. 1963 The magneto-hydrodynamics of a rotating fluid and the Earth's dynamo problem. *Proc. R. Soc. Lond. A* **274**, 274–283.
- TOBIAS, S. M., BRUMMELL, N. H., CLUNE, T. L. & TOOMRE, J. 1998 Pumping of magnetic fields by turbulent penetrative convection. *Astrophys. J.* **502**, L177–L180.
- TOBIAS, S. M., BRUMMELL, N. H., CLUNE, T. L. & TOOMRE, J. 2001 Transport and storage of magnetic field by overshooting turbulent compressible convection. *Astrophys. J.* **549**, 1183–1203.
- TOBIAS, S. M., DIAMOND, P. H. & HUGHES, D. W. 2007 β -Plane magnetohydrodynamic turbulence in the solar tachocline. *Astrophys. J.* **667**, L113–L116.
- VAUCLAIR, S., VAUCLAIR, G., SCHATZMAN, E. & MICHAUD, G. 1978 Hydrodynamical instabilities in the envelopes of main-sequence stars — Constraints implied by the lithium, beryllium, and boron observations. *Astrophys. J.* **223**, 567–582.
- VORONTSOV, S. V., CHRISTENSEN-DALSGAARD, J., SCHOU, J., STRAKHOV, V. N. & THOMPSON, M. J. 2002 Helioseismic measurement of solar torsional oscillations. *Science* **296**, 101–103.
- WALÉN, C. 1946 *Ark. Mat. Astr. Fys.* **30A**, no. 15.

- WALKER, M. R., BARENGHI, C. F. & JONES, C. A. 1998 A note on dynamo action at asymptotically small Ekman number. *Geophys. Astrophys. Fluid Dyn.* **88**, 261–275.
- WANG, Y.-M. & SHEELEY, JR., N. R. 1991 Magnetic flux transport and the Sun's dipole moment — New twists to the Babcock–Leighton model. *Astrophys. J.* **375**, 761–770.
- WEISS, N. O. 1966 The expulsion of magnetic flux by eddies. *Proc. R. Soc. Lond. A* **293**, 310–328.
- WEYMANN, R. & SEARS, R. L. 1965 The depth of the convective envelope on the lower main sequence and the depletion of lithium. *Astrophys. J.* **142**, 174.
- WOOD, T. S. & MCINTYRE, M. E. 2007 Confinement of the Sun's interior magnetic field: Some exact boundary-layer solutions. In *Unsolved Problems in Stellar Physics: A Conference in Honor of Douglas Gough* (ed. R. J. Stancliffe, J. Dewi, G. Houdek, R. G. Martin, & C. A. Tout), *American Institute of Physics Conference Series*, vol. 948, pp. 303–308. Corrigendum at www.atm.damtp.cam.ac.uk/people/mem/papers/SQB0/solarfigure.html#chirality.
- WOOD, T. S. & MCINTYRE, M. E. 2010 Confinement of the Sun's interior magnetic field by laminar magnetostrophic flow. *Submitted to the Journal of Fluid Mechanics*.
- ZAHN, J.-P. 1992 Circulation and turbulence in rotating stars. *A&A* **265**, 115–132.
- ZAHN, J.-P., TALON, S. & MATIAS, J. 1997 Angular momentum transport by internal waves in the solar interior. *A&A* **322**, 320–328.
- ZEL'DOVICH, YA. B. 1957 The magnetic field in the two-dimensional motion of a conducting turbulent fluid. *Soviet Journal of Experimental and Theoretical Physics* **4**, 460.